Università degli Studi di Torino

PhD Programme in Chemical and Materials Sciences XXXII Cycle

Optimization and development of thermoelectric intermetallic compounds for waste heat harvesting

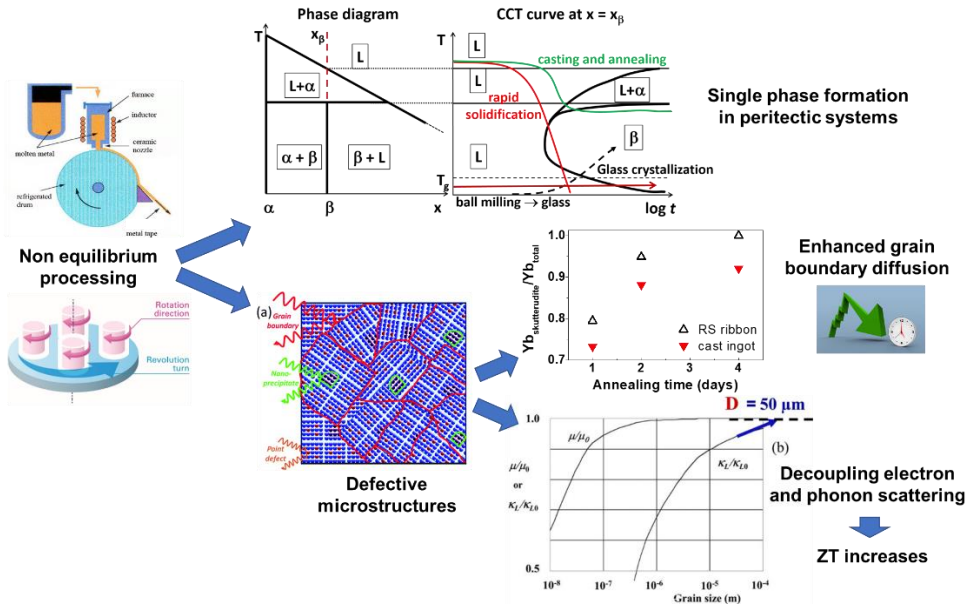

Francesco Aversano

Supervisor:
Prof. Alberto Castellero

Università degli Studi di Torino

PhD Programme in Chemical and Materials Sciences XXXII cycle

Optimization and development of thermoelectric intermetallic compounds for waste heat harvesting

Candidate: **Francesco Aversano**

Supervisor: Prof. **Alberto Castellero**

Jury Members:

Prof. **Marcello Baricco**
Università di Torino
Dipartimento di Chimica

Dr. **Monica Fabrizio**
Consiglio Nazionale delle Ricerche
Istituto di Chimica della Materia Condensata e di Tecnologie per l'Energia

Prof. **Minoru Nohara**
University of Okayama
Research Institute for Interdisciplinary Science

Head of the Doctoral School: Prof. Alberto Rizzuti
PhD Programme Coordinator: Prof. Mario Chiesa

Torino, 2020

PREFACE

The increasing demand of a sustainable approach towards energy policies leads not only to the development of renewable energy technologies, but also to a more careful management of waste energy sources. In this context, thermoelectricity allows to convert directly waste heat into useful electrical energy on the basis of the Seebeck effect. Thermoelectric power generators consist of two semiconductors, one p-type, where the charge carriers are the holes, and one n-type, where charge carriers are the electrons, connected electrically in series and thermally in parallel. When a temperature difference is applied the charge carriers moves from the hot side to cold side generating a net current flow. Nowadays, the thermoelectric application is limited by their efficiency factor around 10 % for power generation, mainly due to limits of the material's properties used in a device. One of the key challenges is to find thermoelectric materials with high thermoelectric performance in the medium-high temperature range.

The main objective of my PhD thesis was to investigate different classes of thermoelectric materials for applications in the medium-high temperature range, adopting two strategies. On the one hand, I studied the effect of the non-equilibrium techniques, such as rapid solidification, on the structural, microstructural and thermoelectric properties of established compounds (i.e. $CoSb_3$ skutterudite and

TiNiSn half Heusler alloy) with the aim to optimize the processing of these materials. On the other hand, starting from ab-initio prediction of phase stability and band structure, I studied, from the experimental point of view, compounds, such as TaCoSn half Heusler alloy and ullmannites, that have not been considered for thermoelectric applications so far.

The present manuscript is divided into six chapters.

The first chapter consists of an extensive literature review. The concepts related to thermoelectricity are summarized and the main strategies used to enhance the thermoelectric performance are described.

The second chapter is devoted to the description of the processing techniques of the materials studied in this thesis. Furthermore, a description of the instrumental techniques for structural, microstructural and thermoelectric characterization is reported.

The third chapter focuses on the Yb-filled $CoSb_3$ skutterudite. The effect of different processing routes on the structural, microstructural and thermoelectric properties is discussed.

The fourth chapter deals with TiNiSn half Heusler compound. The complex interplay between structural, microstructural and thermoelectric properties is analysed, considering the role of the processing routes, residual secondary phases and thermal cycling.

The fifth chapter focuses on the experimental investigation of the thermodynamic stability and thermoelectric properties of the “novel” TaCoSn half-Heusler compound.

Finally, the sixth chapter is devoted to the experimental work performed during my stay at Okayama University (Japan) on ullmannites that represent a new class of promising thermoelectric metallic materials.

ACKNOWLEDGEMENT

Firstly, I would like to express my sincere gratitude to my advisor Prof. Alberto Castellero for his continuous support of my PhD study and related research, for his patience, motivation and knowledge. His guidance helped me in the research activity and while writing this thesis. I could not have imagined having a better advisor and mentor for my Ph.D study.

I would also like to thank the members of the committee for the evaluation of my PhD thesis (Prof. Marcello Baricco, Dr. Monica Fabrizio and Prof. Minoru Nohara) for reading and assessing the manuscript.

I would like to thank Prof. Minoru Nohara and Prof. Michael Reece who hosted me in their institutions for a period abroad. They supported both my scientific activity and my daily life in their country.

I would also like to thank Gianluca Fiore, Maurizio Leo and Maria Carmen Valsania for their availability and valuable help.

I thank my fellow labmates in for the stimulating discussions, and for all the fun we have had in the last three years.

I would like to thank my girlfriend for emotional support and accompanying me all the time.

Last but not the least, I would like to thank my family, my parents and my brother, for supporting me spiritually throughout writing this thesis and my life in general.

PhD activities

Papers

F. Aversano, A. Ferrario, S. Boldrini, C. Fanciulli, M. Baricco, A. Castellero "Thermoelectric Properties of TiNiSn Half Heusler Alloy Obtained by Rapid Solidification and Sintering" Journal of Materials Engineering and Performance (2018), 27, p. 6306–6313.

Zhen Zhang, Shuai Fu, Francesco Aversano, Mauro Bortolotti, Haiwen Zhang, Chunfeng Hu, Salvatore Grasso "Arc melting: a novel method to prepare homogeneous solid solutions of transition metal carbides (Zr, Ta, Hf)" Ceramics International (2019), 45, p. 9316-9319.

F. Aversano, S. Branz, E. Bassani, C. Fanciulli, A. Ferrario, S. Boldrini, M. Baricco, A. Castellero "Effect of rapid solidification on the synthesis and thermoelectric properties of Yb-filled Co_4Sb_{12} skutterudite" Journal of Alloys and Compounds (2019), 796, p. 33-41.

Presentations

Talks

Oral presentation National: "EFFECT OF DIFFERENT PROCESSING ROUTES ON THE PROPERTIES OF SKUTTERUDITE $Yb_{0.25}Co_4Sb_{12}$" F. Aversano, S. Branz, M. Baricco, A. Castellero, E. Bassani, C. Fanciulli, A. Ferrario, S. Boldrini - Giornate sulla Termoelettricità: Torino, 22-23 February 2017.

Oral presentation National: "HALF HEUSLER ALLOY FOR THERMOELECTRIC APPLICATION" F. Aversano - Annual Metallurgy Group Lab. Meeting – Italy, Vaie (TO), 06/07/2017.

Oral presentation National: "EFFECT OF DIFFERENT PROCESSING ROUTES ON THE PROPERTIES OF THERMOELECTRIC MATERIALS"

Aversano F. – Metallurgy Lab. Seminar, Department of Chemistry, University of Turin – Italy, Turin (TO), 19/01/2018.

Oral presentation National: "AMORPHOUS AND CRYSTALLINE TaCoSn: STUDY OF A NEW THERMOELECTRIC MATERIAL" F. Aversano, A. Ferrario, S. Boldrini, C. Fanciulli, M. Baricco, A. Castellero – Giornate sulla Termoelettricità: Santa Margherita Ligure (GE), 21-22 February 2018.

Oral presentation International: "EFFECT OF NON-EQUILIBRIUM PROCESSING ON THE SYNTHESIS AND THERMOELECTRIC PROPERTIES OF SKUTTERUDITES AND HALF HEUSLER COMPOUNDS" F. Aversano, A. Ferrario, S. Boldrini, C. Fanciulli, M. Baricco, A. Castellero – ISMANAM: Italy, Rome (RM), 2-6 July 2018.

Oral presentation National: "SYNTHESIS AND CHARACTERIZATION OF ULLMANNITE COMPOUNDS" F. Aversano, K. Kudo, S. Ayukawa, M. Nohara, M. Baricco, A. Castellero – Giornate sulla Termoelettricità: BOLOGNA (BO), 20-21 February 2019.

Oral presentation International: "Amorphous and Crystalline TaCoSn: Study of a New Thermoelectric Material" F. Aversano, A. Ferrario, S. Boldrini, C. Fanciulli, M. Baricco, A. Castellero – European Conference on Thermoelectrics (ECT): Cyprus 23-25 September 2019

Posters

Poster presentation: "EFFECT OF DIFFERENT PROCESSING ROUTES ON THE PROPERTIES OF $Yb_{0.25}Co_4Sb_{12}$ THERMOELECTRIC COMPOUND" F. Aversano, S. Branz, E. Bassani, C. Fanciulli, A. Ferrario, S. Boldrini, M. Baricco, A. Castellero – European Conference on Thermoelectrics (ECT): Padova (PD), 25-27 September 2017.

Poster presentation: "EFFECT OF DIFFERENT PROCESSING ROUTES ON THE PROPERTIES OF (Nb,Ta,V)CoSn HALF HEUSLER ALLOYS" Francesco Aversano, Kan Chen, Alberto Castellero, Marcello Baricco, Mike J. Reece – International Conference on Thermoelectric (ICT): France, Caen 1-5 July 2018.

Period abroad

20/04/2018-20/07/2018 United Kingdom, Queen Mary University of London, Engineering and Materials Science Engineering, Supervisor: Prof. Mike J. Reece.

01/10/2018-31/12/2018 Japan, Okayama University, Research Institute for Interdisciplinary Science, Supervisor: Prof. Minoru Nohara.

PhD Courses Attended

Course title	**Instructor**	**University / Department**	**Hours**
Statistics advanced	Bollani, Lombardi, Lonati, Sacco, Corsi, Garbarino	University of Turin, Department of agrarian	40
Introduction to Crystallography	P. Benna	University of Turin, CRISDI	6
Electron Diffraction	R. Cossio	University of Turin, CRISDI	4
X-Ray Diffraction	A. Pavese	University of Turin, CRISDI	4
Instrumentation for X-Ray Diffraction	A. Agostino	University of Turin, CRISDI	4
X-Ray Diffraction Methods: Polycrystalline	M. Milanesio	University of Turin, CRISDI	10
Solid State Properties: Modelization	A. Ferrari	University of Turin, CRISDI	8
The Rietveld Method	A. Agostino	University of Turin, CRISDI	8
X-Ray Diffraction Applications on Materials Study	S. Bianco, G. Ubertalli, M. Pavese, S. Ronchetti	Polytechnic of Turin, CRISDI	8
Aerospace metallic materials and technologies	Maciaj Motyka	Rzeszow University of Technology, Poland	8

PhD schools attended

Varenna course on "Advances in thermoelectricity: fondamental issues, materials and nanotechnology"- Italy, Varenna (LC), 14-20 July 2019

Seminars, Workshops, Conferences Attended

2nd year PhD presentations. – Italy, University of Turin, Department of Chemistry, 29-30/09/2016

PhD Defense Wolczyk – Italy, University of Turin, Department of Chemistry, 15/02/2017

Giornate sulla Termoelettricità: Torino, 22-23th febbrary 2017.

PhD Defense Emanuele Marano – Italy, University of Turin, Department of Chemistry, 02/03/2017.

PhD Defense Eirini Maria Paschalidou – Italy, University of Turin, Department of Chemistry, 11/04/2017.

Metallurgy Lab Seminar Marco Poletti- Italy, University of Turin, Department of Chemistry, 28/04/2017.

Metallurgy Lab Seminar Erika Dematteis - Italy, University of Turin, Department of Chemistry, 09/06/2017.

Metallurgy Group Lab. Meeting, Italy, Vaie (TO), 06/07/2017.

PhD Defense Nadia Belmonte – Italy, University of Turin, Department of Chemistry, 24/07/2017.

2nd year PhD presentations. – Italy, University of Turin, Department of Chemistry, 25/09/2016.

Incontro di studio: Aspetti della Moderna Triade (Calore – Elettricità – Meccanica) – Italy, Milano 26/10/2017.

Metallurgy Lab Seminar Federico Scaglione - Italy, University of Turin, Department of Chemistry, 10/11/2017.

Workshop NIS Colloquium: Recent advances in biosensor technologies – Italy, University of Turin, Department of Chemistry, 22/11/2017.

Workshop: Gender equality: don't change women, change the system – Italy, University of Turin, Department of Chemistry, 24/11/2017.

Corso base di solidificazione – Italy, Milano (MI), 28th February and 1st March 2018.

Metallurgy Lab Seminar Matteo Cialone - Italy, University of Turin, Department of Chemistry, 09/03/2018.

European Conference on Thermoelectrics (ECT): Padova, 25-27 September 2017.

Giornate sulla Termoelettricità (GiTe): S. Margherita Ligure, 22-23 February 2018.

International Conference on Thermoelectrics (ICT): Caen, 1-5 July 2018.

Metallurgy Lab Seminar Dario Gianoglio - Italy, University of Turin, Department of Chemistry, 18/01/2019.

Metallurgy Lab Seminar Francesco Aversano - Italy, University of Turin, Department of Chemistry, 18/01/2019.

Workshop NIS Colloquium: Materials and microstructures in Additive Manufacturing - Italy, University of Turin, Department of Chemistry, 14/02/2019.

Giornate sulla Termoelettricità (GiTe): Bologna, 20-21 February 2019.

Giornate del Crisdi x-ray diffraction: a useful tool for chemistry and material science - Italy, University of Turin, Department of Chemistry, 28/02/2019.

Seminar: Selected metallic materials and technologies for aerospace industry - Italy, University of Turin, Department of Chemistry, 05/04/2019.

PhD Defense Matteo Cialone – Italy, University of Turin, Department of Chemistry, 12/04/2019.

Teaching lab. Assistance

Laboratory of metallic materials, Prof. Paola Rizzi

Contents

CHAPTER I: INTRODUCTION AND BACKGROUND

The world's demand for energy is causing a dramatic escalation of social and political unrest. Likewise, the environmental impact of global climate change due to the combustion of fossil fuels is becoming increasingly alarming. Thus, the biggest challenge for humankind is to find alternative sources of energy. For several years, effort has been concentrated in search for alternative sources of energy that are environmentally friendly. Thermoelectricity is one way to improve the sustainability of our electricity base through the scavenging of waste heat with thermoelectric generators. Thermoelectricity allows to recover useful electric energy from unused waste heat generated by home heating, automotive exhaust, and industrial processes. As thermoelectric generators are solid-state devices with no moving parts, they are silent, reliable and scalable, making them ideal for small, distributed power generation[1]. The quality of thermoelectric material is measured by a parameter called thermoelectric figure of merit (ZT). Despite the potential advantages of this technology, thermoelectricity currently has too low efficiency to be cost-effective in most applications[2]. However, a resurgence of interest in thermoelectricity began in the mid1990s when significant progress was made in increasing the efficiency of thermoelectric materials in various ways, for example, exploring the novel thermoelectric materials with high ZT or developing novel techniques such as nanostructuring to increase the ZT value of existing thermoelectric materials.

1.1 Thermoelectric Phenomena

1.1.1 Seebeck effect

The Seebeck effect is the direct conversion of heat to electricity when the junctions of two different materials are subjected to a temperature difference. This effect was discovered by the German physicist Thomas Seebeck in 1821 who noted a potential difference between two ends of a metal bar when the metal bar is placed in the temperature gradient along its length[3]. The same phenomena was discovered later for a closed loop of two dissimilar metals in the presence of a temperature difference between the junctions, as shown in Figure I- 1.

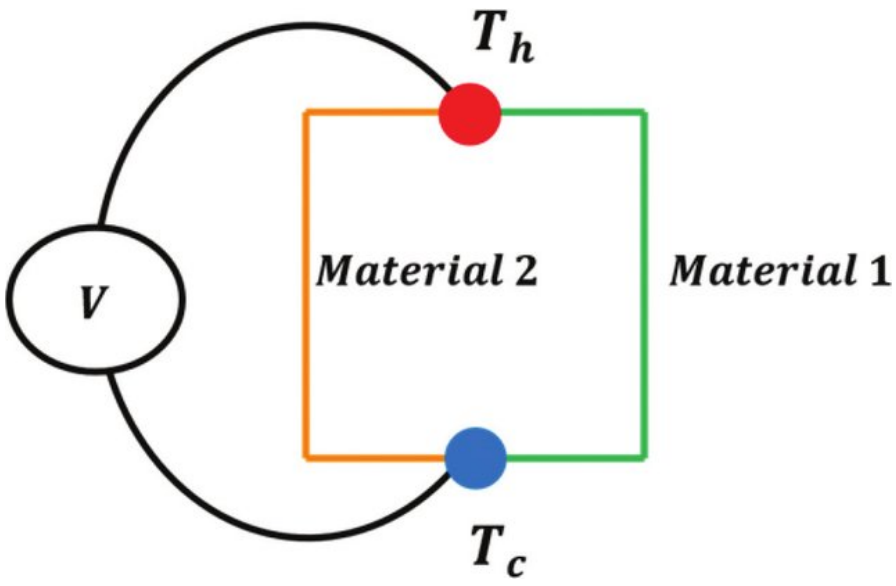

Figure I- 1: Seebeck effect: A, B are two types of conductors, a temperature difference induces a voltage between the junctions.[4]

In the presence of temperature difference, charge carriers (electrons or holes) in the material moves from the hot side to the cold side generating an internal electrical field and building up a thermoelectric voltage. The thermoelectric voltage generated between the hot and cold side is defined as,

$$\Delta V = -\alpha \Delta T \tag{I-1}$$

where α is the Seebeck coefficient of the material and ΔT is the temperature difference between the hot and cold junctions. The Seebeck coefficient, also known as the thermopower of the material, is defined as the ratio of the thermoelectric voltage to the temperature difference,

$$\alpha = -\frac{\Delta V}{\Delta T} \tag{I-2}$$

The voltage generated between the junctions can be written as,

$$V = \int_{T1}^{T2} (\alpha B(T) - \alpha A(T)) dT \tag{I-3}$$

where α_A and α_B are the absolute Seebeck coefficients of the materials A and B, and T_1 and T_2 are the temperatures at the junction 1 and 2, respectively.

1.1.2 Peltier effect

Peltier effect is the inverse of the Seebeck effect and is associated with the thermoelectric refrigerator. This effect was discovered by the

French physicist Jean Peltier in 1834[5]. When an electric current passes through junctions of two dissimilar conductors or semiconductors, heat will be adsorbed at one junction and cooling will be developed at the other junction. The heating and cooling of the junctions depends on the flow of the current.

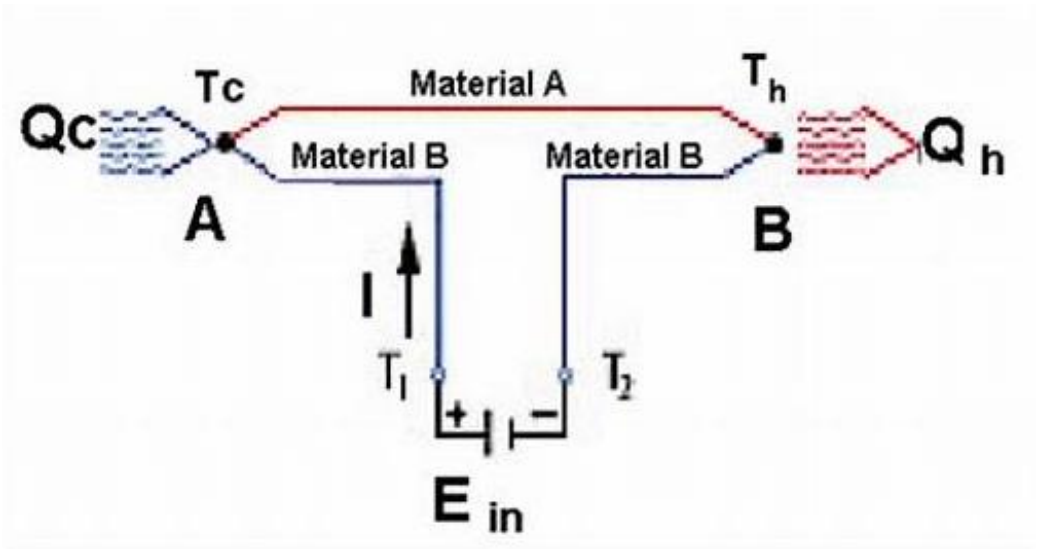

Figure I- 2: Peltier effect in two dissimilar materials A and B in the presence of external voltage ΔV.[6]

When a potential difference is applied across the junction in the direction as shown in *Figure I- 2*, heat is generated at one junction, T_h, and cooling is developed at another junction, T_c. In the Peltier effect the heat absorbed by T1 per unit of time can be written as,

$$Q = (\Pi_A - \Pi_B)I \qquad \text{(I-4)}$$

where Π_A and Π_B are called Peltier coefficients of each material.

1.1.3 Thomson's effect

The last of the thermoelectric effects, the Thomson effect relates to the rate of generation of reversible heat q which results from the passage of a current along a portion of a single conductor along which there is a temperature difference ΔT. Providing the temperature difference is small, $q = \beta I \Delta T$, where β is the Thomson coefficient. Although the Thomson effect is not primary importance in thermoelectric devices it should not be neglected in detailed calculations.

1.1.4 The Kelvin relationships

The above three thermoelectric coefficients are related by the Kelvin relationships[7]:

$$\alpha_{ab} = \frac{\Pi_{ab}}{T} \tag{I-5}$$

$$\frac{d\alpha_{ab}}{dT} = \frac{\beta_a - \beta_b}{T} \tag{I-6}$$

These relationships can be derived using irreversible thermodynamics. Their validity has been demonstrated for many thermoelectric materials and it assumed that they hold for all materials used in thermoelectric applications.

1.2 Thermoelectric figure of merit

A good thermoelectric material should have high electrical conductivity to minimize thermal noise from Joule heating which is generated when a current passes through the thermoelectric material, a low thermal conductivity to minimize the heat loss to maintain a large temperature gradient across the junction and a large Seebeck coefficient to produce a large voltage. At the beginning of the XX century, Altenkirch incorporated all these qualities introducing the concept of figure of merit[8,9]. The figure of merit (Z) of a thermoelectric material can be formulated as,

$$ZT = \frac{\alpha^2 \sigma}{k} T \qquad \text{(I-7)}$$

$$k = k_{el} + k_{lat} \qquad \text{(I-8)}$$

where α is the Seebeck coefficient, σ is the electrical conductivity, k is the thermal conductivity and T is the absolute temperature. k consists of an electronic component, k_{el}, and a lattice component, k_{lat} (equation I-8). The expression $\alpha^2\sigma$ is also known as power factor[10].

The difficulty at the base of the synthesis of thermoelectric materials with high ZT is in obtaining at the same time a high electrical conductivity (σ), a large Seebeck coefficient (α) and the lowest possible thermal conductivity (k). However, for bulk materials there is an interrelation between the three parameters σ, α and k. Moreover σ, α and k are also strongly dependent on the materials crystal

structure, electronic structure and carrier concentration[11]. The most of materials can be classified into metals, semiconductors and insulators. The thermoelectric properties of metals, semiconductors and insulators at 300 K are tabulated in Table I-1, while the trend of thermoelectric properties as function of carrier concentration are plotted in Figure I- 3.

Table I-1: Thermoelectric properties of metals, semiconductors and insulators at 300 K[12]

Property	Metals	Semiconductors	Insulators
α (μVK^{-1})	~ 5	~ 200	~ 1000
σ ($\Omega^{-1}Cm^{-1}$)	~ 10^{6}	~ 10^{3}	~ 10^{-12}
Z (K^{-1})	~ 3 x 10^{-6}	~ 2 x 10^{-3}	~ 5 x 10^{-17}

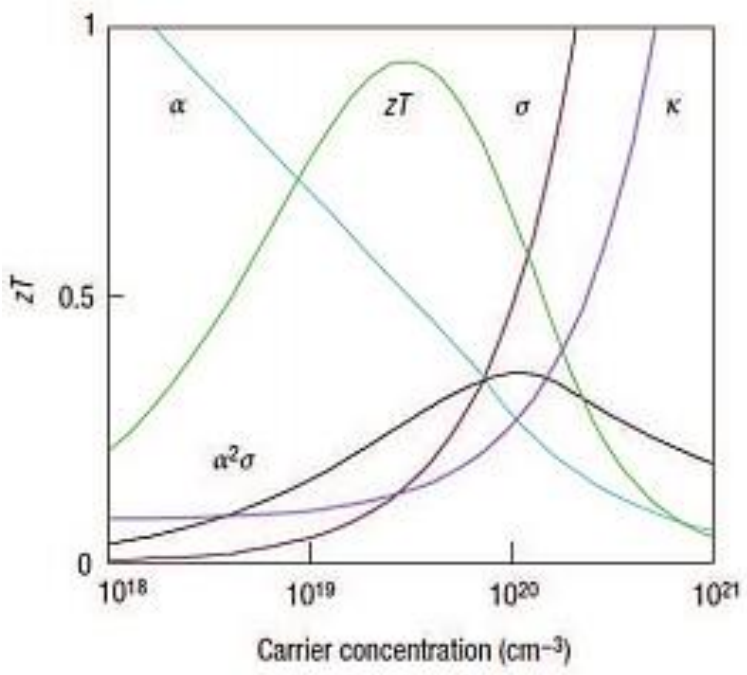

Figure I- 3: Seebeck coefficient (α), electrical conductivity (σ), power factor ($\alpha^2\sigma$) and electronic (k_{el}) and lattice (k_{lat}) thermal conductivity as a function of free charge carrier concentration n[13].

As the carrier concentration increases, the electrical conductivity increases. However, in the same time the Seebeck coefficient decreases and the thermal conductivity increases. An increase in σ implies an increase in k_{el} because correlated by the Wiedmann-Franz law[14],

$$k_{el} = L\sigma T \qquad \text{(I-9)}$$

where L is known as Lorentz number and T is the absolute temperature. Lorenz number is not a completely constant value (it depend on temperature and material); Charles Kittel gives values

ranging from 2.23 x 10^{-8} V^2K^{-2} for the copper at 0 °C to 3.2 x 10^{-8} V^2K^{-2} for tungsten at 100 °C[15].

1.3 Transport properties

The relation I-7 shows a strong dependence of the ZT parameter on, both, electrical and thermal conductivities. In order to find the better compromise and maximise the figure of merit, we have to perfectly understand the influence of both parameters.

1.3.1 Seebeck coefficient

From the Boltzmann's transport equation, a general expression for the Seebeck coefficient can be deived in a simplified form as,

$$\alpha = \frac{1}{eT}\frac{\int \sigma(E)(E-E_F)dE}{\int \sigma(E)\frac{f_0}{E}dE} \qquad \text{(I-10)}$$

where *e* is the electron charge, $\sigma(E)$ is the electrical conductivity for the electrons that fill the energy levels between E and $E+dE$, f_0 is the Fermi-Dirac distribution function, E_F is the Fermi energy equals to the chemical potential at 0 K and T is the absolute temperature[16]. Equation I-10, shows that the Seebeck coefficient is proportional to E-E_F. Thus, in theory, higher Seebeck coefficient can be expected if the low energy carriers are cut off, which is called energy filtering[17].

1.3.2 Electrical conductivity

For semiconductors, a general expression of the electrical conductivity can be calculated again from Boltzmann's transport equation by using the Fermi-Dirac distribution function and an isotropic parabolic band energy model[18].

$$\sigma = \frac{2e^2\tau}{m^*}\left(\frac{m^* K_B T}{2\pi\hbar^2}\right)^{3/2} e^{-\frac{|E_F|}{K_B T}} \qquad \text{(I-11)}$$

where e is the electron charge, τ a relaxation time, which corresponds to the mean scattering time between carrier collisions, m^* is the effective mass of the carriers, k_B is the Bolzmann constant, $\hbar$ the reduced Plank constant and E_F the Fermi energy of the semiconductor. Therefore, the electrical conductivity is strongly correlated to the dopant species and concentration. Through the Fermi level, it is also linked to the material intrinsic properties, as the electronic and crystalline structure and the atomic mass, for example. Finally, the electrical conductivity is also influenced by the different scattering mechanisms activated in the material.

1.3.3 Thermal conductivity

The thermal conductivity characterizes the transport of heat in solids. Thermal energy is transferred by thermalized electrons in the conduction band and the lattice vibrations (phonons). Thus, the total thermal conductivity, k, can be written as reported in equation I-8.

- Electronic thermal conductivity

When the carriers are passing through the material and transport electrical energy, they also transport heat. The thermal conductivity due to the carriers can be an important feature especially for heavily doped semiconductors. In according to the Wiedemann-Franz law[14] the electrical contribution to the thermal conductivity can be written as reported in equation I-9.

- Lattice thermal conductivity

Another contribution to the thermal conductivity of a material is the heat carried by lattice vibrations also known as phonons. A good approximation for it can be derived from the classical kinetic theory[19]

$$k_{lat} = \frac{C_v v_s l}{3} \qquad \text{(I-12)}$$

where C_v is the specific heat capacity at constant volume, v_s is the average sound velocity and l is the mean free path of phonons. At very low temperatures, because of the low amount of phonon excitation and because of their very long wavelength associated, phonon scattering in negligible and the lattice thermal conductivity is dominated by the Debye thermodynamic law, given by[20]:

$$k_{lat} = \frac{C_v v_s l}{3} \approx \frac{v_s l}{3}\left(\frac{T}{\theta_D}\right)^3 \qquad \text{(I-13)}$$

with θ_D the Debye temperature.

However, above the Debye temperature, C_v approaches the classical constant value 3NR with N the number of moles of the considered material. Thus, the lattice thermal conductivity is dominated by the behaviour of the mean free path of phonons, *l*, since the phonon velocity is almost independent of the temperature and accordingly the short wavelength phonons are dominant.

1.4 Phonon scattering mechanisms

Scattering of carriers and phonons have to be understood. As the electrical conductivity and the Seebeck coefficient values are directly affected by carrier scattering, whereas phonon scattering impacts on the thermal conductivity value of a given material. The main scattering mechanisms in thermoelectric materials are described below. All scattering mechanisms limit the mean free path of carriers. Thus, the total relaxation time, τ, is proportional to the sum of the inverse of every single scattering time, τ_i, from each source, and it can be written as[21]:

$$\frac{1}{\tau} = \frac{1}{\tau_1} + \frac{1}{\tau_2} + \cdots + \frac{1}{\tau_i} \qquad \text{(I-14)}$$

1.4.1 carrier scattering

In thermoelectric material, carriers can be electrons, holes or both. When these latter moving, they can be scattered by various mechanisms such as interactions with impurities, phonons, defects or

other carriers[22]. The most important mechanism in metals and semiconductors is the electron-phonon scattering[23]. In metals, most of the Brillouin zone is occupied by electrons. Thus, scattering takes place from one point to another one on the Fermi surface with large momentum changes. Whereas in semiconductors, this zone being mostly unoccupied, the change in momentum vector occurs only at small angles. Thus, this is reason why small angle scattering is critical in semiconductors. The carrier-phonon scattering mechanism in the semiconductor depends on the probability that a carrier will move from an initial to a final position. Thus, it is proportional to the availability of the energy states, to the probability of absorbing or emitting a phonon and the strength of the carrier-phonon interaction. Other well-known carriers scattering processes are acoustic phonons scattering scattering, dominating at room temperature, and optical phonon scattering dominating at high temperatures.

1.4.2 Phonon-phonon scattering

In most semiconductors, phonons are predominantly scattered by other phonons. Peierls showed that the most important scattering process involves three phonons[20]: either two phonons combine to create a third one (normal situation), as shown in Figure I- 4a, or one phonon breaks up into two phonon (Umklapp situation), as in Figure I- 4. In the normal situation, the energy and momentum are conserved in the collision, all the phonons scatter with a wave vector conservation equation:

$$\vec{k}_1 + \vec{k}_2 = \vec{k}_3 \qquad \text{(I-15)}$$

The wave vector of the third phonon lies within the first Brillouin zone, like in Figure I- 4a. Consequently, there is a redistribution of phonons without any thermal resistance. On the contrary, for the Umklapp situation, the energy is conserved but not the momentum, as shown in the following equation:

$$\vec{k}_1 + \vec{k}_2 = \vec{k}_3 + \vec{G} \qquad \text{(I-16)}$$

Here, k_3 lies outside the Brillouin zone. It can be mapped back into this zone by adding the reciprocal lattice vector, G, as in Figure I- 4b. G contributes to the thermal resistance. Moreover, Peierls showed that the Umklapp situation is predominant at high temperatures and therefore it is responsible for lowering the lattice thermal conductivity of a given material. From the second order perturbation theory, the relaxation time for three phonons in the Umklapp scattering situation, τ_U, above room temperature, is given by[24]:

$$\frac{1}{\tau_U} = 2\gamma^2 \frac{k_B T}{V_0 \mu} \frac{\omega^2}{\omega_D} \qquad \text{(I-17)}$$

where μ is the shear modulus, V_0 is the volume per atom of the crystal lattice, ω_D is the Debye frequency and γ represents the Gruneisen parameter which measures the anharmonicity of the lattice vibrations.

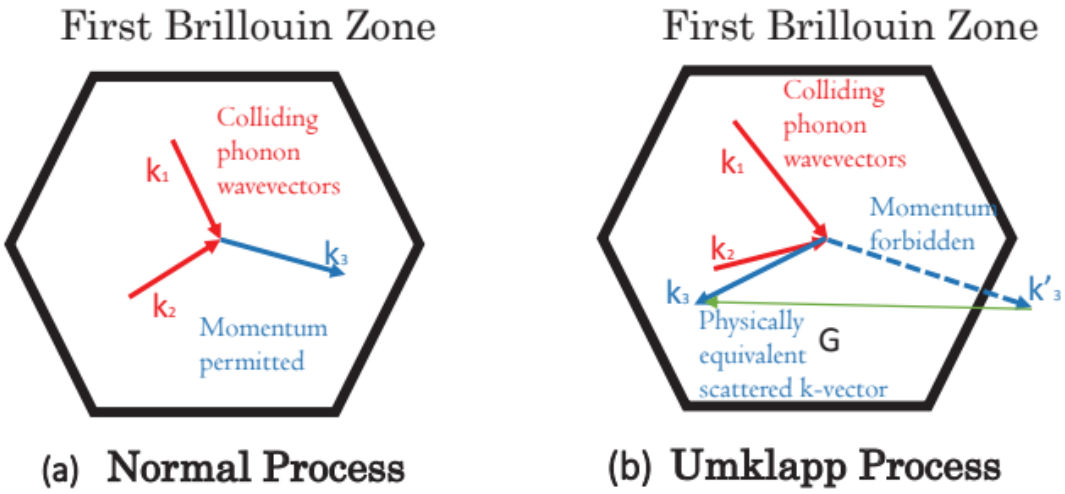

Figure I- 4: Normal scattering (a), Umklapp scattering (b).[25]

1.4.3 Boundary scattering

Another important scattering mechanism, for polycrystalline materials, involves grain boundaries. Boundary scattering is an important mechanism, especially at low temperatures and for long wavelength phonons. It depends typically on grain size and its relaxation time is given by[26]:

$$\frac{1}{\tau_B} = \frac{v}{D}(1-p) \qquad \text{(I-18)}$$

where D is the average grain diameter of a polycrystalline material, v is the phonon velocity and p is the boundary specularity parameter. In fact $1-p$ represents the probability that the phonon undergoes diffusive scattering at the different interfaces. In the case of very interacting interfaces (roughness, non-linearity for example), the

scattering is purely diffusive and $p = 0$, as in Figure I- 5b. Then equation I-18 is reduced to the well-known Casimir limit[26]:

$$\frac{1}{\tau_B} = \frac{v}{D} \tag{I-19}$$

The grain boundaries in a polycrystalline material can also scatter charge carrier, lowering the carrier's mobility and thus the electrical conductivity. Nevertheless, in most cases, the reduction of electrical conductivity due to carrier scattering is compensated by the reduction in thermal conductivity because of phonon scattering. Indeed, according to relation (I-18) a grain size reduction promotes an improvement of the thermoelectric performances of a given polycrystalline material[27].

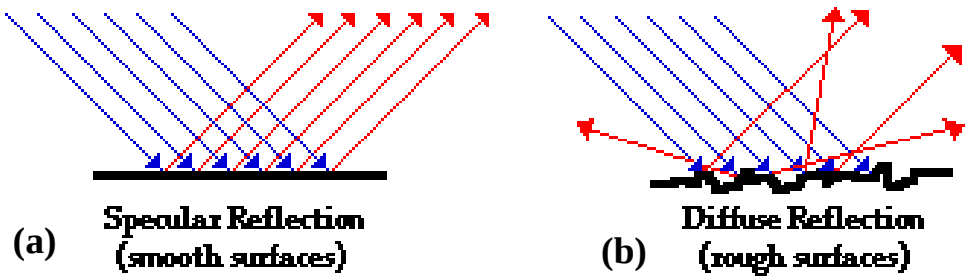

Figure I- 5: specular boundary scattering (a) and diffuse boundary scattering (b).[28]

1.4.4 Defects scattering

Defects scattering involves something locally in the crystal that is different from all the atoms that surrounding it. For example, it can be

due to impurity sites, different isotopes, solid solutions or lattice vacancies in the host material[29]. The atom mass is possibly different from the host atoms and so it creates a point defect in the thermoelectric material, as shown in Figure I- 6. At high temperatures, only the short wavelength phonons are strongly scattered by point defects in the lattice. The phonon relaxation time, τ_D, for this scattering mechanism can be expressed as:

$$\frac{1}{\tau_D} = \frac{V_0 \Gamma \omega^4}{4\pi v^3} \qquad \text{(I-20)}$$

where Γ is a disorder parameter proportional to the strength of the scattering point defect, V_0 is the volume per atom of the crystal lattice, v and ω are the phonon velocity and frequency, respectively. Once again, this phenomenon can also affect carriers'motion, but phonons scattering is stronger in intensity and therefore it leads to a final improvement of the thermoelectric performance by reducing strongly the lattice contribution to the thermal conductivity.

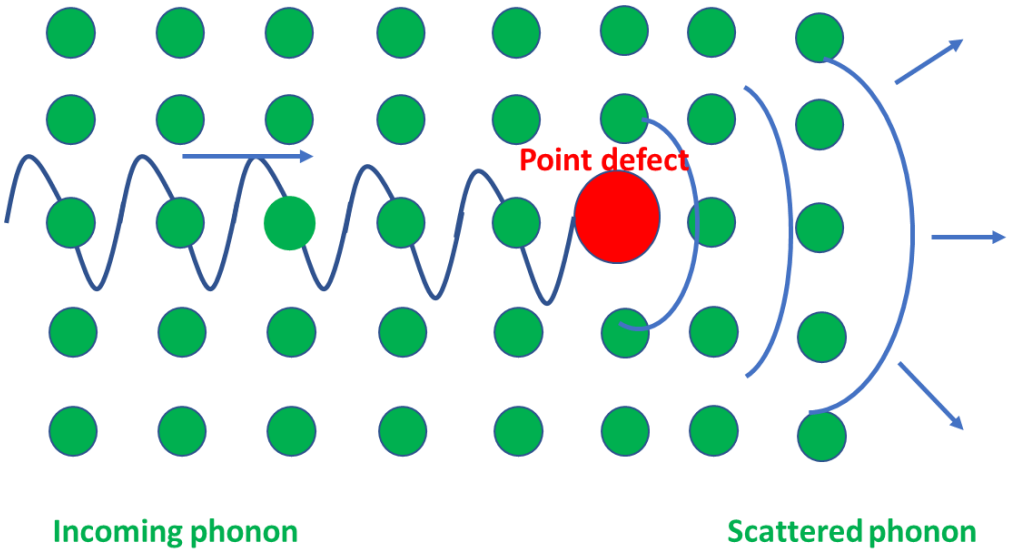

Figure I- 6: Phonon scattering by a point defect

1.5 Thermoelectric efficiency

The efficiency of thermoelectric power generator is defined as the ratio of electric power delivered to the load W to the total power drawn from heat source Q and can be expressed as equation I-21,

$$\eta = \frac{W}{Q} = \frac{T_H - T_C}{T_H}\left[\frac{(1+ZT)^{1/2}-1}{(1+ZT)^{1/2}+\frac{T_C}{T_H}}\right] \quad (21)$$

where T_H and T_C are temperatures at hot and cold junctions respectively, ZT is the aforementioned dimensionless figure of merit and the term $\frac{T_H - T_C}{T_H}$ is known as the Carnot's efficiency. Similarly, the coefficient of performance (COP), which measures the efficiency of a refrigerator or cooling device is defined as the ratio of the heat drawn

from the source Q to the total power consumption, and can be expressed as equation I-22,

$$COP = \frac{Q}{W} = \frac{T_C\left[(1+ZT)^{1/2} - \frac{T_H}{T_C}\right]}{T_H - T_C\left[(1+ZT)^{1/2}+1\right]} \qquad \text{(I-22)}$$

Equations I-21 and I-22 clearly show that the efficiency of thermoelectric power generator and the COP of the thermoelectric refrigerator directly depend on ZT of the material used in thermoelements. Hence a higher ZT is required for better performance of thermoelectric generators and refrigerators.

1.6 Strategies to increase ZT

As discussed in the section 1.2, ZT is a combination of more physical parameters ($\alpha, \sigma, k\ and\ T$). The three fundamental parameters ($\alpha, \sigma\ and\ k$) are interconnected to each other, so it is not straightforward to enhance ZT simply optimizing one of these parameters. Anyway, in order to simplify the discussion, the optimization of three fundamental parameters ($\alpha, \sigma\ and\ k$) will be discussed separately. In most cases the ZT improvement results from combined strategies which optimize two or all of the fundamental parameters.

1.6.1 Strategies to increase electrical conductivity

The electrical conductivity can be calculated by the following equation:

$$\sigma = \frac{1}{\rho} = ne\mu \qquad \text{(I-23)}$$

where n is the carrier concentration, e is the elementary charge and μ is the carrier mobility. In order to increase σ, carrier concentration and/or carrier mobility should be increased.

1.6.1.1 optimizing carrier concentration

One of the effective method to improve thermoelectric properties of most TE materials is to optimize the carrier concentration[30]. The optimum carrier concentration for good TE materials is typically in the range of 10^{19} to 10^{21} cm^{-3}. There are two different approaches to tune carrier concentration, for example, substitution and introducing point defects.

- Substitution:

The substitution is a conventional approach to adjust the carrier concentration[31]. Typically, the method is achieved by filling some guest atoms in a caged structure or alloying with elements from the nearby columns in the periodic table[32]. According to the types of charge carriers (n-type or p-type), the elements (left column or right column) will be chosen. Even if the method seems simple, choosing a

suitable dopant is not easy. In fact, in many cases the higher TE performances theoretically predicted have not been realized in the experiments because the optimum carrier concentration cannot be achieved because of solubility limit[33]. Thus, knowledge of the solubility limits in multi-components phase diagrams is necessary [34]. For example, in $CoSb_3$ skutterudite, the research of the solubility limits depending on whether it is Co-rich or Sb-rich in this material[35].

- Point defects:

Introducing point defects, such as interstitials, vacancies and antisites, it is possible to tune the carrier concentration, [36]. The types and concentrations of these intrinsic point defects are very sensitive to the composition of the materials. In principle, a smaller difference of covalent radius and the electronegativity between the cation and the anion leads to a smaller formation energy of the cation antisite defects[37]. For example, in the p-type $Bi_{2-x}Sb_xTe_3$ difference in covalent radius and electronegativity between Sb and Te is smaller than that between Bi and Te. So the formation energy of antisite defects will be reduced and thus carrier concentration will be increased with the increasing Sb content[36,38].

1.6.1.2 Improving carrier mobility

A high carrier mobility is required to improve the electric conductivity and the thermoelectric performance as well. The carrier mobility in a semiconductor is related to the electronic structure and different

scattering mechanisms. When there are several different parallel carrier scattering mechanisms, their contributions could be expressed in the Matthiessen's rule, equation I-14.

- Acoustic phonon scattering

Normally, at room temperature acoustic phonon scattering is dominant among the different scattering mechanisms in thermoelectric materials. The scattering of carriers and the perturbation of the energy bands is caused by the local strain when an acoustic phonon wave goes through the lattice in the crystal. The process is deformation potential scattering from acoustic phonons, in which deformation potential is used to describe the coupling strength between carriers-phonons[39]. Normally different deformation potential coefficients can affect the carrier mobility greatly. According to the single parabolic band (SPB) model[40], the acoustic phonon scattering carrier mobility is expressed as:

$$\mu_{ac} \sim \frac{C_l}{m_I^* {m_b^*}^{3/2} E^2 T^{3/2}} \tag{I-24}$$

where C_l is the average longitudinal elastic modulus, m_I^* is the transport effective mass along the direction of the conduction, m_b^* is single-valley density of states effective mass and E is the deformation potential. So to increase carrier mobility the material should have a large C_l and small m_I^*, m_b^* and E.

- Ionized impurity scattering

In most heavily doped TE materials, the carrier concentration is in the range of 10^{19} to 10^{21}. So in these materials, the ionized impurity atoms in the atoms can provide scattering centers for charge carriers. The modulation doping is proposed to improve the carrier mobility and to solve the problem. Embedding a heavily doped minor secondary phase into the pristine matrix is possible to obtain the modulation doping which allows at the charge carriers in the minor secondary phase to be separated from their parent grains and moved into the pristine matrix. This strategy in many cases allows to increase the carrier mobility, as consequence of the reduced carrier scattering around the ionized impurities. This strategy has successfully demonstrated by *Chen et al.* embedding some heavily doped silicon nanograins into pristine SiGe matrix[41,42]. The schematic diagram, shown in Figure I- 7, illustrates the modulation doping used by *Chen* in his experiment in which a large improvement in power factor as well as *ZT* value has been achieved.

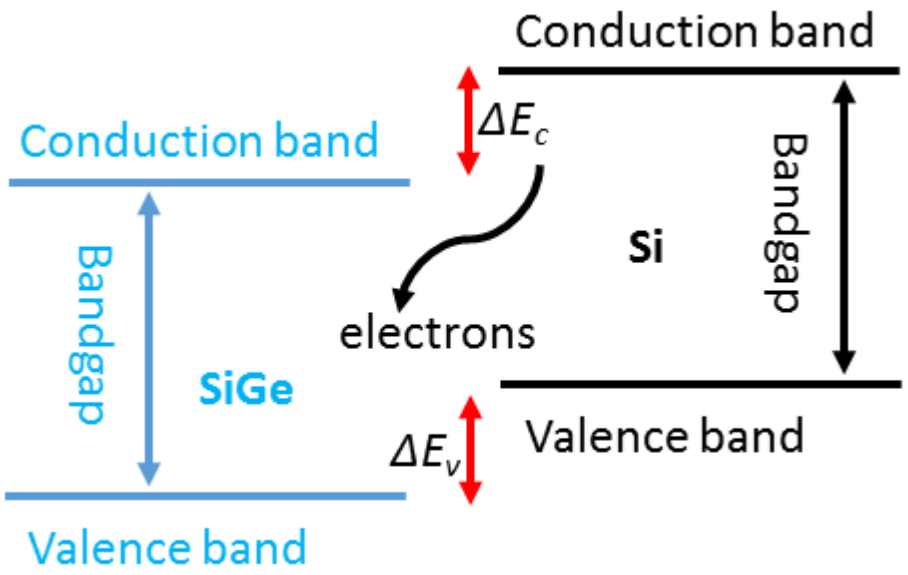

Figure I- 7: A schematic diagram illustrating the modulation doping.[43]

- Grain-boundary scattering

In nanostructured material, when the grain size is comparable to the electron mean free path, grain-boundary scattering will be noticeable[44]. The anisotropy of carrier mobility in the single crystal is generally strong, while the anisotropy of carrier mobility in polycrystalline samples is generally weak because of the random orientation of the grains. We need to reduce to reduce the impact of different grain boundaries on the transport in order to have a good carrier mobility, especially in polycrystalline anisotropic structure samples[45]. So a good strategy could be reconstructing the random grain boundaries in the polycrystal to somewhat-ordered structure. One approach is the mechanical alignment of the grains through

uniaxial compression during the synthesis, such as hot press and spark plasma sintering (SPS)[46,47]. For example, in both n-type $Bi_2Te_{2.1}Se_{0.9}$ and p-type $Bi_{0.4}Sb_{1.6}Te_3$ samples obtained by SPS, an obvious electrical conductivity anisotropy is observed, which mean the existence of texture.

1.6.2 Strategies to increase Seebeck coefficient

Recently some unique physical mechanisms related to band structure engineering have been proposed and experimentally achieved in thermoelectric research, such as energy filtering in PbTe-based nanocomposites embedded with Pb nanoparticles[17,48], distortion of the electronic density of states (resonant energy level) in Tl doped PbTe[49], and band convergence[50-51].

1.6.2.1 Through energy filtering to enhance thermoelectric performance

The potential barriers formed at grain boundaries and interfaces can negatively affect the carrier mobility, but in thermoelectric materials they can also play a positive role through enhanced energy filtering effect (EFE)[52-53]. EFE is an additional scattering mechanism introduced through preferentially scattering low energy electrons. Figure I- 8 shows the calculated normalized Seebeck distribution versus energy for heavily doped bulk n-type $Si_{80}Ge_{20}$[54]. The Seebeck coefficient is proportional to the integral of the calculated Seebeck

distribution versus the energy for heavily doped bulk n-type $Si_{80}Ge_{20}$ curve. In a nanocomposite system the grain boundary scattering and interface scattering, which can reduce the carrier mobility, scatter the carriers with energies lower than the barrier height[55], enhancing the Seebeck coefficient, which would have been reduced by low energy electrons because this portion of the Seebeck distribution is negative. EFE is a good example of how nanostructured materials can be used to improve electrical transport properties while still maintaining good thermal transport properties[16,56,57].

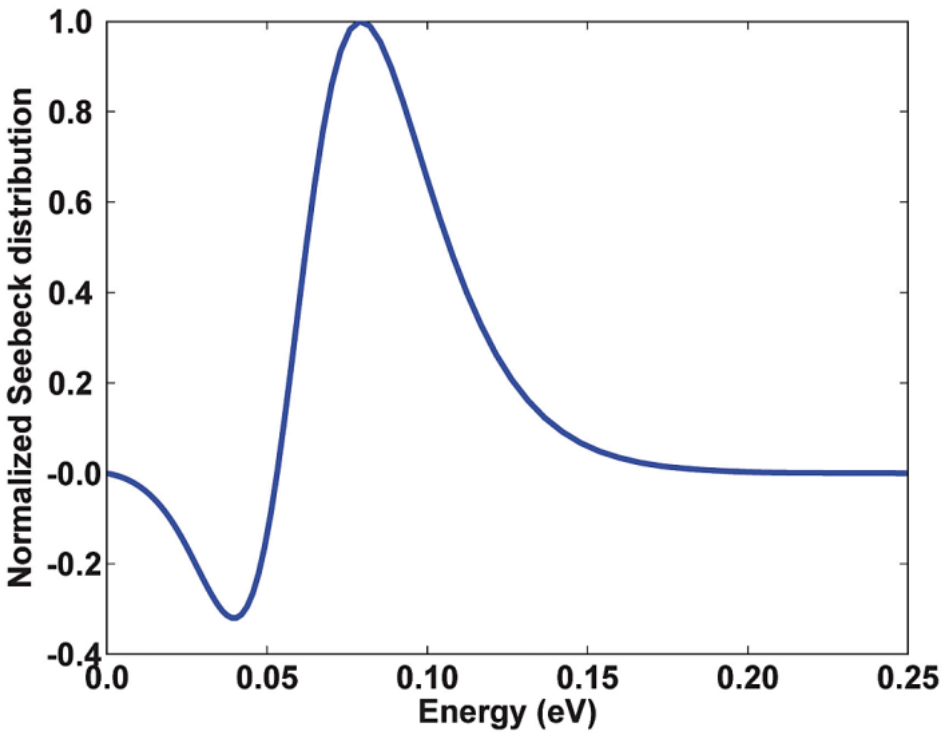

Figure I- 8: Calculated normalized Seebeck distribution versus energy for heavily doped bulk n-type $Si_{80}Ge_{20}$[54]

1.6.2.2 Through resonant levels to enhance the density of electrical states

The Mott equation describes a relationship between the Seebeck coefficient and the carrier properties, and is defined as:

$$\alpha = \frac{\pi^2 k_B^2 T}{3q}\left[\frac{\ln(\sigma(E))}{E}\right]_{E=E_F} =$$

$$\frac{\pi^2 k_B^2 T}{3q}\left[\frac{1}{p}\frac{\partial p(E)}{\partial E} + \frac{1}{\mu}\frac{\partial \mu(E)}{\partial E}\right]_{E=E_F} \quad \text{(I-25)}$$

with carrier mobility $\mu(E) = q\tau/m^*$, where q is the carrier charge, $p(E)$ and $\mu(E)$ are the energy dependence of carrier density and mobility, m^* is the effective mass and E_F is the Fermi energy. From the equation, one approach to enhance the Seebeck coefficient is the introduction of resonant distortion of electrical density of states (DOS) near the Fermi level (E_F) reflected by increased effective mass m^*. The introduction of resonant impurities have been shown to enhance the Seebeck coefficient resulting in an increase in figure of merit[49,58]. Resonant impurities is a concept introduced in solid state physics for metals first[59-60]. Theoretically Hicks[61] and Mahan[62] predict enhancements in thermoelectric properties due to an increase in the electronic density of states first. The resonant level can be regarded as a bound level with an energy that falls above the conduction band edge or below the valence band edge[63], creating a local maximum in the electronic density of states, as shown in Figure I- 9. The figure

represents schematically the case for In:PbTe, where the resonant states are in conduction band. Band structure calculations show not only impurities create sharp DOS peaks close to the Fermi level, but also those peaks should be of the similar character as the host band structure. Results show that d- or even f-state impurities are useful to improve the Seebeck coefficient of metals, but s- or p-state resonance levels are more suited to improve thermoelectric properties of semiconductors[64-65].

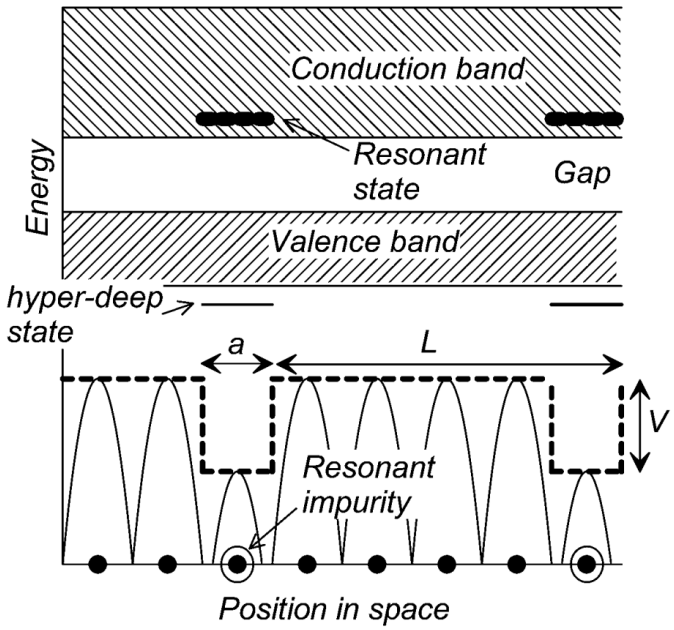

Figure I- 9: Schematic energy versus distance diagram where the spheres on the bottom represent atoms. The periodic potential of the host atoms of the solid is experienced by conduction electrons and results in the formation of conduction and valence bands, extended states available to the nearly-free electrons. The resonant impurities perturb this potential, diffusing the nearly-free electrons over that area of the crystal, and creating a range of additional available energy levels, some bound (deep states inside the gap, or even hyper-deep states in the next gap below the valence band) and some at energies falling inside the extended states, here the conduction band. The figure represents schematically the case for In:PbTe, where the resonant states are in the conduction band[63].

1.6.3 Strategies to reduce lattice thermal conductivity

In a semiconductor, normally the thermal conductivity k consists of two contributions as reported in equation I-8, a lattice contribution k_{lat} and an electronic contribution k_{el}. There are different strategies to decrease the k_{lat}. The lattice thermal conductivity can be estimated by the Matthiessen's rule. So, the combined relaxation time is attained by the addition of the inverse relaxation times for different scattering processes. Furthermore, the inverse relaxation time is proportional to the frequencies of the specific phonon scattering modes. So, lattice thermal conductivity is related to different phonons scattering modes and frequencies. Thus. the transmission of phonons with various frequencies have to be suppressed to reduce the lattice thermal conductivity. We can reduce the k_{lat} introducing simultaneously all-scale hierarchical scattering centers into the host, such as point defects, nanoscale grain boundaries and precipitates, dislocations[66]-[67], as shown in Figure I- 10. The point defects (vacancies, interstitials, antisites and alloying) give a contribution quite important in the scattering of short wavelength, but have the disadvantage that could also scatter the carriers, implying a decrease in mobility[68]-[69].The nanostructure engineering is usually employed in the scattering of short to medium wavelength phonons[70]. The most successful nanostructure engineering method in TE research is to increase grain boundaries or form nanoscale precipitates. The rapid solidification by melt-spinning and mechanical alloying by ball milling are two typical

techniques to obtain refined microstructures[71]. Another effective method to scatter the medium wavelength phonons and consequently reduce k_{lat} is the formation of dislocations. It could be formed by deliberate plastic deformation of the samples during the fabrication process of TE materials[72]-[73]. *Kim et al.* report that a large decrease in k_{lat} of the $Bi_{0.5}Sb_{1.5}Te_3$ because of the dense dislocation arrays formed at the ordered boundaries of nanograins in the matrix through liquid-phase sintering[74].

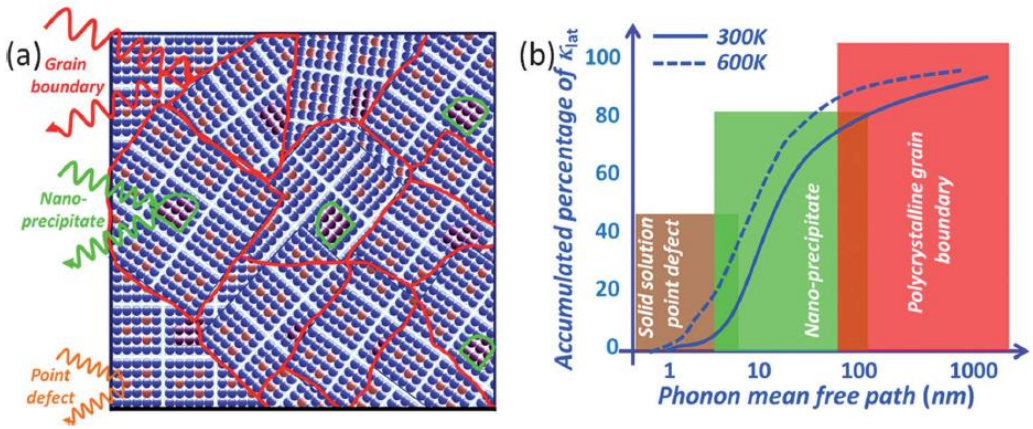

Figure I- 10: All-scale hierarchical architectures and lattice thermal conductivity: (a) all-scale hierarchical architectures, and (b) cumulative distribution function of lattice thermal conductivity with respect to the phonon mean free path in Si or PbTe bulk[75].

1.7 Thermoelectric materials

In this section, the most common of thermoelectric materials that have been investigated in literature will be presented.

1.7.1 Materials for thermoelectric applications

Ioffe was the pioneer of thermoelectric materials investigations by introducing doped semiconductors in 1952[3]. Thermoelectric materials, for Ioffe, had to have a high Seebeck coefficient value and a high value of the mean atomic mass of the atoms of the composition[76]. Few years later, Goldsmid et al. discovered Bi_2Te_3 as the first high-potential thermoelectric material for application around room temperature[77]. In 1956, Ioffe et al. suggested the use of isomorphs solid solutions to create local mass fluctuations through the crystal lattice, in order to induce point defects and phonon scattering leading a significantly lower thermal conductivity values for the same kind of alloys. After these preliminary developments, different classes of thermoelectric materials have been developed, as shown in Figure I- 11.

- Chalcogenides

Birholz used the concept based on solid solution of isomorphs by alloying the already promising Bi_2Te_3 to Sb_2Te_3 compounds[38]. Nowadays, the chalcogenides still remain basic materials group for thermoelectric application in the low temperature range since n-types $Bi_2Te_{3-x}Se_x$ and p-types $Bi_{2-x}Sb_xSe_3$ exhibit a *ZT* value around 1.4 at 100 °C[71]. Subsequently tin chalcogenides have attracted a great interest. A high *ZT* value of about 2.6 at 650 °C has been reported for SnSe single crystal according to peculiar orientations[78]. PbTe family

are another well-known chalcogenide-based materials. They have been used in practical application and depending on the dopant used n and p-type compound have been obtained. Despite the high performance of these materials their application has been limited because of rareness of Te and environmental ot toxicity problems linked to the Te and Pb elements.

- Si based materials

Abeles et al. synthesized a solid solution between silicon and germanium[79]. Even if the individual elements are bad thermoelectric materials, the solid solution Si-Ge presents good thermoelectric properties, for example a maximum value of ZT about 0.95 at 950 °C for p-type SiGe have been obtained[80]. Nowadays, for the high cost of germanium the alloys germanium-poor are attracting more attention. Other materials Si-based are the higher manganese silicides (HMS), for example for an Al-doped $MnSi_{1.73}$ a ZT close to 0.7 at 500°C are reported[81].

- PGEC approach

Another approach to achieve a maximum ZT value, known as the "phonon glass lectron crystal" (PGEC) was introduced in 1979 by Slack[82]. The electron-crystal requirement stems from the fact that crystalline semiconductors have been the best at meeting the compromises required from the electronic properties (Seebeck coefficient and electrical conductivity). Phonon-glass requirement

stems from the need for as low a lattice thermal conductivity as possible. These features can be obtained by rattling motion of loosely bonded atoms within a large cage, generating strong scattering of lattice vibrations (phonons) but having a few impacts on the electron displacement. Among the PGEC materials, skutterudites and clathrates have been extensively investigated. These materials have the feature to have a cage structure, where a large metal atom can be inserted in order to scatter phonons. Since the void-filling atoms can act as electron donors or acceptors and can be small and heavy, good Seebeck coefficients can be obtained. In the same time, the specific structure promotes a large structural disorder, reducing the lattice thermal conductivity and leading to *ZT* values higher than 1. For example, a *ZT* value of 1.7 was reported in filled n-type skutterudites $Ba_{0.08}La_{0.05}Yb_{0.04}Co_4Sb_{12}$ at 580 °C[83] and a *ZT* around 1.35 at 630 °C was found for an n-type $Ba_8Ga_{16}Ge_{30}$ clathrate[84]. Other material, as the half-Heusler group, exhibit an optimised complex crystalline structure and their chemical composition incorporate a large variety of atoms, limiting the mean free path of phonons. They appear to be a good thermoelectric candidate for high temperature range because of their chemical stability and also they are easily synthetized.

- Nanostructuration

In the past 20 years, the thermoelectric community realized about the importance of the low structure dimension for thermoelectric materials[85]. For polycrystalline materials, the nanostructuration

consists of decreasing as much as possible the grain size, promoting phonon scattering at the increased amount of grain boundaries. Considering the phonon mean free path (100-200 nm at room temperature)[86], nanostructures are supposed to scatter phonons more efficiently than charge carriers (mean free path around 10-30 nm at room temperature). Therefore, nanostructuration reduces thermal conductivity more than electrical conductivity resulting in a *ZT* enhancement[87].

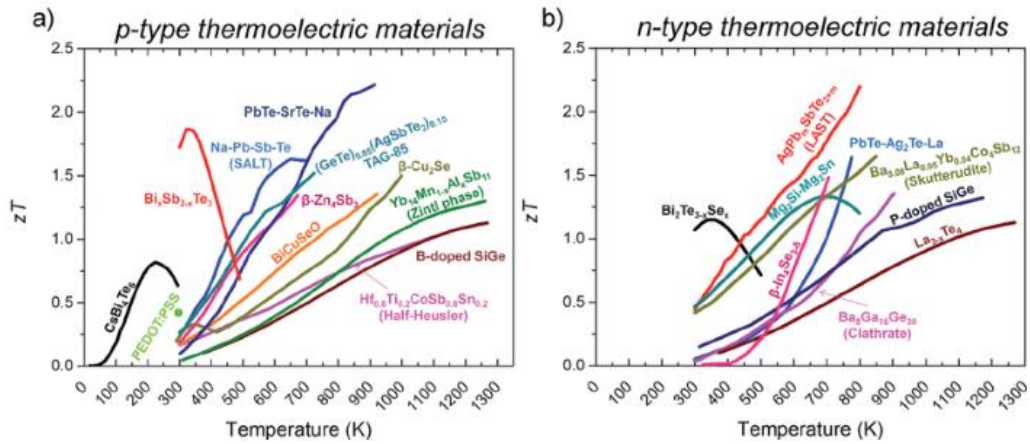

Figure I- 11: Examples of (a) n and (b) p-type thermoelectric materials from the literature[88]

1.7.2 Material selection

As shown in the section 1.7.1 many families of thermoelectric materials, for different range of temperature, have been investigated. Most of these have been improved and new class have been developed, leading to high improvement of *ZT*, but a thermoelectric material to be efficient and viable for large scale production of power

generator has to fulfil several requirements, as shown in Figure I- 12. First, the raw materials chosen have to be non-toxic, cheap and abundant. Secondly, the manufacturing process should be robust and compatible with the production of a high volume of materials per day. Finally, the materials have to exhibit acceptable thermoelectric properties in the temperature range of interest for the final application. Furthermore, they must also have a long-term stability in different kinds of environments and good mechanical properties.

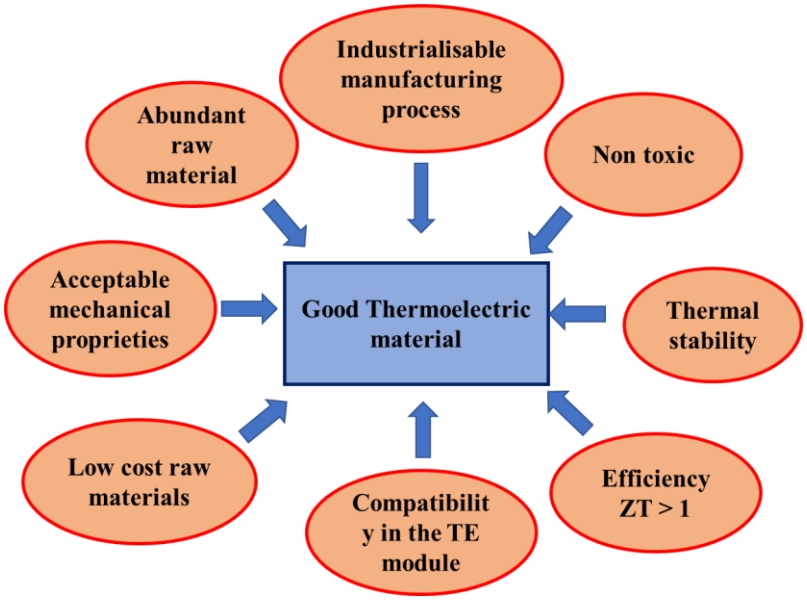

Figure I- 12: Requirements for a good thermoelectric material

1.8 Aim of the thesis

As said before, thermoelectricity is one way to improve the sustainability of our electricity base by scavenging waste heat by means of thermoelectric generators. The study of thermoelectricity goes from the synthesis of the material to the development of

thermoelectric generators involving more sectors (chemistry, physics, engineering). In this thesis, the following aspects related to selected intermetallic thermoelectric materials are considered:

- Development of processes for compounds that show complex solidification paths. In skutterudites (Chapter 3) and many half-Heusler compounds such as TiNiSn (Chapter 4) and TaCoSn (Chapter 5), the presence of peritectic transformations slows down phase formation because of long distance diffusion paths. In this work, I studied the effect of non-equilibrium techniques, such as rapid solidification and mechanical alloying, on the phase formation of these compounds.
- Microstructure control by means of non-equilibrium processing techniques such as rapid solidification and mechanical alloying in the case of Skutterudites (Chapter 3), TiNiSn (chapter 4) and TaCoSn (Chapter 5)
- Synthesis and characterization of new thermoelectric compounds such as half Heusler TaCoSn (chapter 5) and ullmannites (Ni,Pd)Sb(S,Se) (Chapter 6) during my periods abroad in UK and Japan, respectively.

References

1. *CRC Handbook of Thermoelectrics*. *CRC Handbook of Thermoelectrics* (2010). doi:10.1201/9781420049718

2. Rowe, D. M. Thermoelectrics handbook: macro to nano. *Thermoelectr. Handb. Macro to Nano* (2005). doi:10.1038/ki.2011.318

3. Seebeck, T. J. Ueber die magnetische Polarisation der Metalle und Erze durch Temperaturdifferenz [Magnetic polarization of metals and ores by temperature differences]. *Abhandlungen der K. Akad. der Wissenschaften zu Berlin (in Ger.* (1826). doi:10.1002/andp.19163561702

4. Kanimba, E. & Tian, Z. Modeling of a Thermoelectric Generator Device. in *Thermoelectrics for Power Generation - A Look at Trends in the Technology* (2016). doi:10.5772/65741

5. Peltier, J. C. A. Nouvelles Expériences sur la Caloricité des courans électriques. *Ann. Chim. Phys.* (1934).

6. Zhang, C. W. *et al.* Study on a battery thermal management system based on a thermoelectric effect. *Energies* (2018). doi:10.3390/en11020279

7. Apertet, Y. & Goupil, C. On the fundamental aspect of the first Kelvin's relation in thermoelectricity. *Int. J. Therm. Sci.* (2016). doi:10.1016/j.ijthermalsci.2016.01.009

8. Altenkirch, V. E. Über den Nutzeffekt der Thermosäule. *Phys. Zeitschrift* (1909).

9. Kim, H. S., Liu, W. & Ren, Z. The bridge between the materials and devices of thermoelectric power generators. *Energy Environ. Sci.* **10**, 69–85 (2017).

10. Fais, A., Actis Grande, M. & Forno, I. Influence of processing parameters on the mechanical properties of Electro-Sinter-Forged iron based powders. *Mater. Des.* **93**, 458–466 (2016).

11. Madsen, G. K. H. Automated search for new thermoelectric materials: The case of LiZnSb. *J. Am. Chem. Soc.* (2006). doi:10.1021/ja062526a

12. Wood, C. Materials for thermoelectric energy conversion. *Reports Prog. Phys.* (1988). doi:10.1088/0034-4885/51/4/001

13. Snyder, G. J. & Toberer, E. S. Complex thermoelectric materials. *Nature Materials* (2008). doi:10.1038/nmat2090

14. Franz, R. & Wiedemann, G. Ueber die Wärme-Leitungsfähigkeit der Metalle. *Ann. Phys.* (1853). doi:10.1002/andp.18531650802

15. Kittel C. *Introduction to Solid State Physics, 8th edition, Berkeley*. *John Wiley & Sons, New York* (1996).

16. Bahk, J. H., Bian, Z. & Shakouri, A. Electron energy filtering by a nonplanar potential to enhance the thermoelectric power factor in bulk materials. *Phys. Rev. B - Condens. Matter Mater. Phys.* (2013). doi:10.1103/PhysRevB.87.075204

17. Heremans, J. P., Thrush, C. M. & Morelli, D. T. Thermopower enhancement in lead telluride nanostructures. *Phys. Rev. B - Condens. Matter Mater. Phys.* (2004). doi:10.1103/PhysRevB.70.115334

18. Yaqub, R. Nanoinclusions on Transport Properties of Half Heuslers. (2011).

19. Balaguru, R. J. B. Lattice Vibrations, Phonons, Specific Heat Capacity, Thermal Conductivity. 1–24

20. Peierls, R. Zur kinetischen Theorie der Wärmeleitung in Kristallen. *Ann. Phys.* (1929). doi:10.1002/andp.19293950803

21. IV. On the influence of temperature on the electric conducting-power of alloys. *Philos. Trans. R. Soc. London* (1864). doi:10.1098/rstl.1864.0004

22. W. Ashcroft, N. & D. Mermin, N. *Solid State Physics*. *Solid State Physics* (1976).

23. Paufler, P. J. F. Nye. Physical Properties of Crystals. Clarendon Press — Oxford. First published in paperback with corrections and new material 1985. XVII + 329 p. £ 15.00. ISBN 0-19-851165-5. *Cryst. Res. Technol.* (1986). doi:10.1002/crat.2170211204

24. Sommerfeld, A. Zur Elektronentheorie der Metalle auf Grund der Fermischen Statistik. *Zeitschrift fur Phys.* (1928). doi:10.1007/bf01391055

25. Kittel, Introduction to solid state physics, Wiley (2006)

26. Casimir, H. B. G. Note on the conduction of heat in crystals. *Physica* (1938). doi:10.1016/S0031-8914(38)80162-2

27. Xie, W. *et al.* Recent Advances in Nanostructured Thermoelectric Half-Heusler Compounds. *Nanomaterials* (2012). doi:10.3390/nano2040379

28. Yang, M. F., Tuchin, V. V. & Yaroslavsky, A. N. Principles of light-skin interactions. in *Light-Based Therapies for Skin of Color* (2009). doi:10.1007/978-1-84882-328-0_1

29. Narayanamurti, V., Störmer, H. L., Chin, M. A., Gossard, A. C. & Wiegmann, W. Selective transmission of high-frequency phonons by a superlattice: The ‘dielectric’ phonon filter. *Phys. Rev. Lett.* (1979). doi:10.1103/PhysRevLett.43.2012

30. Zhao, L. D. *et al.* Ultrahigh power factor and thermoelectric performance in hole-doped single-crystal SnSe. *Science (80-.).* (2016). doi:10.1126/science.aad3749

31. Qiu, Y. *et al.* Charge-compensated compound defects in Ga-containing thermoelectric skutterudites. *Adv. Funct. Mater.* (2013). doi:10.1002/adfm.201202571

32. Bai, S. Q. *et al.* Enhanced thermoelectric performance of dual-element-filled skutterudites BaxCeyCo4Sb12. *Acta Mater.* (2009). doi:10.1016/j.actamat.2009.03.018

33. Fu, C. *et al.* High band degeneracy contributes to high thermoelectric performance in p-type Half-Heusler compounds. *Adv. Energy Mater.* (2014). doi:10.1002/aenm.201400600

34. Bajaj, S., Wang, H., Doak, J. W., Wolverton, C. & Jeffrey Snyder, G. Calculation of dopant solubilities and phase diagrams of X-Pb-Se (X = Br, Na) limited to defects with localized charge. *J. Mater. Chem. C* (2016). doi:10.1039/c5tc03970c

35. Tang, Y. *et al.* Phase diagram of In-Co-Sb system and thermoelectric properties of In-containing skutterudites. *Energy Environ. Sci.* (2014). doi:10.1039/c3ee43240h

36. Starý, Z., Horák, J., Stordeur, M. & Stölzer, M. Antisite defects in Sb2-xBixTe3 mixed crystals. *J. Phys. Chem. Solids* (1988). doi:10.1016/0022-3697(88)90130-8

37. Horák, J., Stary, Z., Lošťák, P. & Pancíř, J. Anti-site defects in n-Bi2Se3 crystals. *J. Phys. Chem. Solids* (1990). doi:10.1016/0022-3697(90)90017-A

38. Birkholz, U. Untersuchung Der Intermetallischen Verbindung Bi2Te3 Sowie Der Festen Lösungen Bi2-XSbXTe3 Und Bi2Te3-XSeX Hinsichtlich Ihrer Eignung Als Material Für Halbleiter-Therm. *Zeitschrift fur Naturforsch. - Sect. A J. Phys. Sci.* (1958). doi:10.1515/zna-1958-0910

39. Wollmann, L., Nayak, A. K., Parkin, S. S. P. & Felser, C. Heusler 4.0: Tunable Materials. (2016). doi:10.1146/annurev-matsci-070616-123928

40. Hundy, G. H., Trott, A. R. & Welch, T. C. *Refrigeration and Air-Conditioning*. *Refrigeration and Air-Conditioning* (2008). doi:10.1016/B978-0-7506-8519-1.X0001-1

41. Yu, B. *et al.* Enhancement of thermoelectric properties by modulation-doping in silicon germanium alloy nanocomposites. *Nano Lett.* (2012). doi:10.1021/nl3003045

42. Zebarjadi, M. *et al.* Power factor enhancement by modulation doping in bulk nanocomposites. *Nano Lett.* (2011). doi:10.1021/nl201206d

43. https://www.nanotech-now.com/news.cgi?story_id=44989.

44. Dresselhaus, M. S. *et al.* New directions for low-dimensional thermoelectric materials. *Adv. Mater.* (2007). doi:10.1002/adma.200600527

45. Delves, R. T., Bowley, A. E., Hazelden, D. W. & Goldsmid, H. J. Anisotropy of the electrical conductivity in bismuth telluride. *Proc. Phys. Soc.* (1961). doi:10.1088/0370-1328/78/5/329

46. Shen, J. J., Hu, L. P., Zhu, T. J. & Zhao, X. B. The texture related anisotropy of thermoelectric properties in bismuth telluride based polycrystalline alloys. *Appl. Phys. Lett.* (2011). doi:10.1063/1.3643051

47. Hu, L. P. *et al.* Shifting up the optimum figure of merit of p-type bismuth telluride-based thermoelectric materials for power generation by suppressing intrinsic conduction. *NPG Asia Mater.* (2014). doi:10.1038/am.2013.86

48. Heremans, J. P., Thrush, C. M. & Morelli, D. T. Thermopower enhancement in PbTe with Pb precipitates. *J. Appl. Phys.* (2005). doi:10.1063/1.2037209

49. Heremans, J. P. *et al.* Enhancement of thermoelectric efficiency in PbTe by distortion of the electronic density of states. *Science (80-.).* (2008). doi:10.1126/science.1159725

50. Pei, Y. *et al.* Convergence of electronic bands for high performance bulk thermoelectrics. *Nature* (2011). doi:10.1038/nature09996

51. Tang, Y. *et al.* Convergence of multi-valley bands as the electronic origin of high thermoelectric performance in CoSb3 skutterudites. *Nat. Mater.* **14**, 1223–1228 (2015).

52. O'Dwyer, M. F., Lewis, R. A., Zhang, C. & Humphrey, T. E. Electronic efficiency in nanostructured thermionic and thermoelectric devices. *Phys. Rev. B - Condens. Matter Mater. Phys.* (2005). doi:10.1103/PhysRevB.72.205330

53. Wang, S. & Mingo, N. Tailoring interface roughness and superlattice period length in electron-filtering thermoelectric materials. *Phys. Rev. B - Condens. Matter Mater. Phys.* (2009). doi:10.1103/PhysRevB.79.115316

54. Minnich, A. J., Dresselhaus, M. S., Ren, Z. F. & Chen, G. Bulk nanostructured thermoelectric materials: Current research and future prospects. *Energy and Environmental Science* (2009). doi:10.1039/b822664b

55. Ohtaki, M. & Hayashi, R. Enhanced thermoelectric performance of nanostructured ZnO: A possibility of selective phonon scattering and carrier energy filtering by nanovoid structure. in *International Conference on Thermoelectrics, ICT, Proceedings* (2006). doi:10.1109/ICT.2006.331368

56. Xiong, Z., Chen, X., Huang, X., Bai, S. & Chen, L. High thermoelectric performance of Yb0.26Co4Sb 12/yGaSb nanocomposites originating from scattering electrons of low energy. *Acta Mater.* **58**, 3995–4002 (2010).

57. Xiong, Z. *et al.* Effects of nano-TiO2 dispersion on the thermoelectric properties offilled-skutterudite Ba0.22Co4Sb12. *Solid State Sci.* (2009). doi:10.1016/j.solidstatesciences.2009.06.007

58. Gratz, E. & Zuckermann, M. J. Chapter 42 Transport properties (electrical resistivity, thermoelectric power and thermal conductivity) of rare earth intermetallic compounds. *Handb. Phys. Chem. Rare Earths* **5**, 117–216 (1982).

59. Korringa, J. & Gerritsen, A. N. The cooperative electron phenomenon in dilute alloys. *Physica* (1953). doi:10.1016/S0031-8914(53)80053-4

60. Moriya, T. Recent progress in the theory of itinerant electron magnetism. *J. Magn. Magn. Mater.* (1979). doi:10.1016/0304-8853(79)90201-4

61. Hicks, L. D. & Dresselhaus, M. S. Thermoelectric figure of merit of a one-dimensional conductor. *Phys. Rev. B* (1993). doi:10.1103/PhysRevB.47.16631

62. Mahan, G. D. & Sofo, J. O. The best thermoelectric. *Proc. Natl. Acad. Sci. U. S. A.* (1996). doi:10.1073/pnas.93.15.7436

63. Heremans, J. P., Wiendlocha, B. & Chamoire, A. M. Resonant levels in bulk thermoelectric semiconductors. *Energy and Environmental Science* (2012). doi:10.1039/c1ee02612g

64. Liu, M., Qin, X. Y., Liu, C. S. & Zeng, Z. Enhanced thermoelectric power factor with impurity-induced resonant level. *Appl. Phys. Lett.* (2011). doi:10.1063/1.3624467

65. Androulakis, J. *et al.* Thermoelectric enhancement in PbTe with K or Na codoping from tuning the interaction of the light- and heavy-hole valence bands. *Phys. Rev. B - Condens. Matter Mater. Phys.* (2010). doi:10.1103/PhysRevB.82.115209

66. Biswas, K. *et al.* High-performance bulk thermoelectrics with all-scale hierarchical architectures. *Nature* (2012). doi:10.1038/nature11439

67. Liu, Z. *et al.* Lithium Doping to Enhance Thermoelectric Performance of MgAgSb with Weak Electron-Phonon Coupling. *Adv. Energy Mater.* (2016). doi:10.1002/aenm.201502269

68. Wang, H., Lalonde, A. D., Pei, Y. & Snyder, G. J. The criteria for beneficial disorder in thermoelectric solid solutions. *Adv. Funct. Mater.* (2013). doi:10.1002/adfm.201201576

69. Hu, L., Zhu, T., Liu, X. & Zhao, X. Point defect engineering of high-performance bismuth-telluride-based thermoelectric materials. *Adv. Funct. Mater.* (2014). doi:10.1002/adfm.201400474

70. Xie, W. *et al.* Identifying the specific nanostructures responsible for the high thermoelectric performance of (Bi,Sb)2Te3 nanocomposites. *Nano Lett.* (2010). doi:10.1021/nl100804a

71. Poudel, B. *et al.* High-thermoelectric performance of nanostructured bismuth antimony telluride bulk alloys. *Science (80-.).* (2008). doi:10.1126/science.1156446

72. He, J., Girard, S. N., Kanatzidis, M. G. & Dravid, V. P. Microstructure-lattice thermal conductivity correlation in nanostructured PbTe 0.7 S 0.3 thermoelectric materials. *Adv. Funct. Mater.* (2010). doi:10.1002/adfm.200901905

73. Hu, L. *et al.* Tuning Multiscale Microstructures to Enhance Thermoelectric Performance of n-Type Bismuth-Telluride-Based Solid Solutions. *Adv. Energy Mater.* (2015). doi:10.1002/aenm.201500411

74. Kim, S. Il *et al.* Dense dislocation arrays embedded in grain boundaries for high-performance bulk thermoelectrics. *Science (80-.).* (2015). doi:10.1126/science.aaa4166

75. Zhao, L. D., Dravid, V. P. & Kanatzidis, M. G. The panoscopic approach to high performance thermoelectrics. *Energy and Environmental Science* (2014). doi:10.1039/c3ee43099e

76. Goldsmid, H. J. On the thermal and electrical conductivity of semiconductors. *Proc. Phys. Soc. Sect. B* **67**, 360–363 (1954)

77. Goldsmid, H. J. & Douglas, R. W. The use of semiconductors in thermoelectric refrigeration. *Br. J. Appl. Phys.* (1954). doi:10.1088/0508-3443/5/11/303

78. Zhao, L. D. *et al.* Ultralow thermal conductivity and high thermoelectric figure of merit in SnSe crystals. *Nature* (2014). doi:10.1038/nature13184

79. B. Abeles, D. S. Beers, G. D. C. and J. P. D. Thermal Conductivity of Ge-Si Alloys at High Temperatures. *Phys. Rev.* **125**, 1954–1956 (1962).

80. Joshi, G. *et al.* Enhanced thermoelectric figure-of-merit in nanostructured p-type silicon germanium bulk alloys. *Nano Lett.* (2008). doi:10.1021/nl8026795

81. Bernard-Granger, G. *et al.* Microstructure investigations and thermoelectrical properties of a P-type polycrystalline higher manganese silicide material sintered from a gas-phase atomized powder. *J. Alloys Compd.* (2015). doi:10.1016/j.jallcom.2014.08.164

82. Slack, G. A. The Thermal Conductivity of Nonmetallic Crystals. *Solid State Phys. - Adv. Res. Appl.* (1979). doi:10.1016/S0081-1947(08)60359-8

83. Shi, X. *et al.* Multiple-filled skutterudites: High thermoelectric figure of merit through separately optimizing electrical and thermal transports. *J. Am. Chem. Soc.* **133**, 7837–7846 (2011).

84. Saramat, A. *et al.* Large thermoelectric figure of merit at high temperature in Czochralski-grown clathrate Ba 8Ga 16Ge 30. *J. Appl. Phys.* (2006). doi:10.1063/1.2163979

85. Hicks, L. D. & Dresselhaus, M. S. Effect of quantum-well structures on the thermoelectric figure of merit. *Phys. Rev. B* (1993). doi:10.1103/PhysRevB.47.12727

86. Chen, G. Size and interface effects on thermal conductivity of superlattices and periodic thin-film structures. *J. Heat Transfer* (1997). doi:10.1115/1.2824212

87. Satyala, N., Norouzzadeh, P. & Vashaee, D. Nano Bulk Thermoelectrics: Concepts, Techniques, and Modeling. in (2014). doi:10.1007/978-3-319-02012-9_4

88. Rull-Bravo, M., Moure, A., Fernández, J. F. & Martín-González, M. Skutterudites as thermoelectric materials: Revisited. *RSC Adv.* **5**, 41653–41667 (2015).

CHAPTER II: SYNTHESIS AND CHARACTERIZATION TECHNIQUES

This chapter describes the synthesis and the characterization techniques employed in this work. The section 2.1 describes the synthesis techniques: arc-melting, melt spinning and ball milling. The section 2.2 describes the sintering techniques: Spark Plasma Sintering (SPS), Open Die Pressing (ODP) and Electro-Sinter-Forged (EFS). The section 2.3 describes the techniques for the characterization of structural and microstructural features as well as thermal stability: X-Ray Diffraction (XRD), Scanning Electron Microscopy (SEM), Differential Scanning Calorimetry (DSC) and Thermogravimetric Analysis (TGA). The section 2.4 covers thermoelectric characterization by measurements of electrical conductivity, Seebeck coefficient, Hall-effect and thermal diffusivity.

2.1 Synthesis techniques

2.1.1 Alloying by melting

2.1.1.a Muffle furnace

An electric muffle furnace is an oven used in analytical chemistry and metallurgy, generally for conducting laboratory tests. It is able to reach temperatures from 1000 to 1800 degrees Celsius, depending on the power and efficiency of the refractory material with which it is built. The samples are usually deposited inside it by pincers, and contained in crucibles of ceramic material. Temperature control is entrusted to a digital thermoregulator located on the lower part of the

oven. Typically, the pure elements were placed in a quartz vial, if necessary internally coated with a protective layer (for example boron nitride, graphite), with a diameter of 1 cm, sealed under vacuum of $5x10^{-5}$ Torr to avoid oxidation. The image of a typically muffle is reported in Figure II-1.

Figure II- 1: Muffle

2.1.1.b Arc-melting furnace

Arc melting is typically used for melting metals. The image of a typically arc-melting apparatus is reported in Figure II-2. There are three main parts to the system: a power source, chiller, and vacuum unit. The vacuum unit with a rotary and turbomolecular pump can attain a vacuum of 10^{-6} torr. The cold circulation water from the chiller cools both the copper hearth and the electrodes. Heating is via an electric arc struck between a tungsten electrode and metals placed in

a depression (crucible) in the copper hearth. In inert-gas arc melting, the chamber is evacuated and then back filled with argon gas prevent unwanted oxidation of the sample while molten. Often an oxygen getter (titanium or zirconium) is used as a secondary method to pre-emptively react trace amounts of O_2. Hence, melting is performed in an argon atmosphere. The metals can be heated to a temperature in excess of 3500 ºC. After elemental metals (or master compound) are melted and solidified, it can be 'turned over' by a 'tweezer mechanism' without “breaking” the inert atmosphere (and then remelted). The melting, solidification, turning over of the sample, the re-melting process is typically repeated at least three times to attain a better compositional homogeneity.

Figure II-2: Arc-melting furnace

2.1.1.b Melt-spinning

Melt spinning is a technique used for rapid cooling of molten metals. A wheel is cooled internally, usually by water or liquid nitrogen, and rotated. A typical melt-spinning system consists of a cooling system, power system, a vacuum chamber with rotary and turbomolecular pump, induction heating with vacuum casting device, spinning wheel with a maximum speed 50 meter /sec. By injecting a thin stream of melt onto the rotating wheel, causing rapid solidification. The cooling rates achievable by melt spinning are on the order of 10^4 - 10^7 K/s. The vacuum unit with a combination of rotary pump and turbomolecular pump can attain a vacuum of 10^{-6} torr. The high cooling rates allows to obtain metastable phase (e.g metallic glasses) and highly defective materials (grains refined, supersaturation, solid solutions) which could not be obtained by common annealing process.[1–3] The image of the melt-spinning apparatus used in this work is reported in Figure II-3.

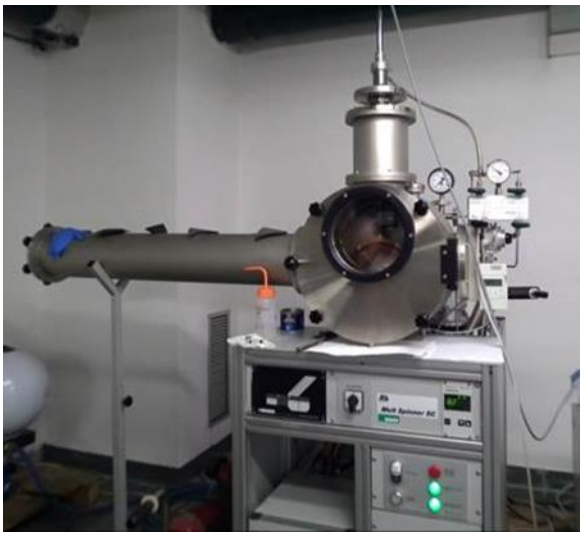

Figure II-3: Melt-spinning apparatus

In the melt-spinning process, the jet is brought so close to the rotating chill-wheel that it interferes with the molten metal flow on the wheel. Consequently, a molten bridge or “puddle” forms between the nozzle face and the spinning wheel (the “planar” gap), and the metal is spun off as a thin ribbon. The schematic illustration of the principle of melt spinning method is presented in Figure II-4. The common crucible is boron nitride or quartz, with a slit nozzle or round nozzle. Melting material from crucible is heated to the above melting temperature and injected through a nozzle onto the chilled spinning wheel. The wheel spinning speed is different for various materials and goals. For example to obtain amorphous alloys, a higher spinning speed is required. In the case of crystalline materials the grain size obtained is inversely proportional to wheel speed. This is important for magnetic materials, because the magnetic performance is associated with the

grain size of samples. Therefore, it is critical to choose the optimal spinning speed of the chill wheel. The width and thickness of the ribbon samples greatly depend on the size of the nozzle. The large size of the nozzle will cause the increase of the width and thickness of the ribbons.[1,2]

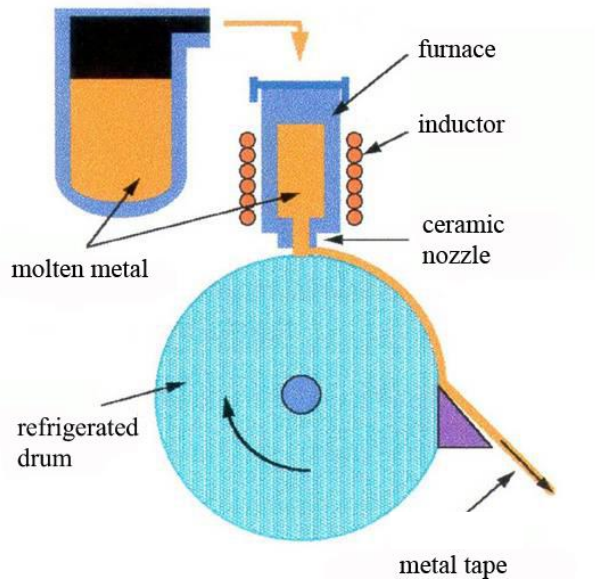

Figure II-4: Schematic illustration of the principle of melt-spinning.

2.1.2 Mechanical alloying

The ball milling technique is based on mechanical forces to transfer energy from the milling tools to the material. The material to grind is placed in a grinding jar, usually made of hardened steel or tungsten carbide, with different grinding balls having different diameters. Then the jar is attached to the planetary ball mill disk, which rotated around a central axis while the jar is simultaneously rotating around its own axis, as shown in Figure II-5.[4]

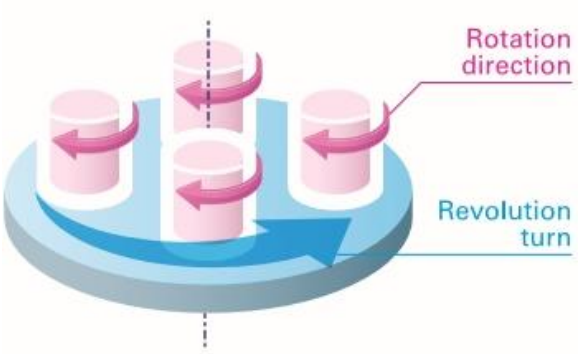

Figure II-5: Rotation and revolution – planetary ball miller.

During the jar motion, the material to grind is trapped and crushed between the moving balls. The size reduction occurs through a sequence of collisions inside the ball miller.[5] Moreover, several parameters can be controlled. For example, the revolution speed, the milling time, the balls and jar sizes and the ball to powder filling ratio can be tailored. All these parameters can change the intensity of the impacts and so the energy transferred to the material inside.[6] The image of a typical planetary ball mill is reported in Figure II-6.

Figure II-6: Planetary ball mill.

2.2 Sintering techniques

2.2.1 Spark Plasma Sintering (SPS)

Spark Plasma Sintering (SPS) has become a routine method for the densification of thermoelectric materials.[7,8] SPS also named field-assisted sintering technique (FAST) is a pressure-assisted sintering method, where the atmosphere can be controlled. A pulsed current, characterized by a low voltage and a high intensity, is imposed between two electrodes to a stack made of a graphite punches, spacers and a pressing die, leading to joule heating of the powders introduced into the die, as shown in Figure II-7. In the same time, the powder bed is compacted using the controlled displacement of the graphite punches. Such a configuration enables heating rates from 1 to 600°C/min to be achieved. Regarding the cooling rate, it can be easily tailored.

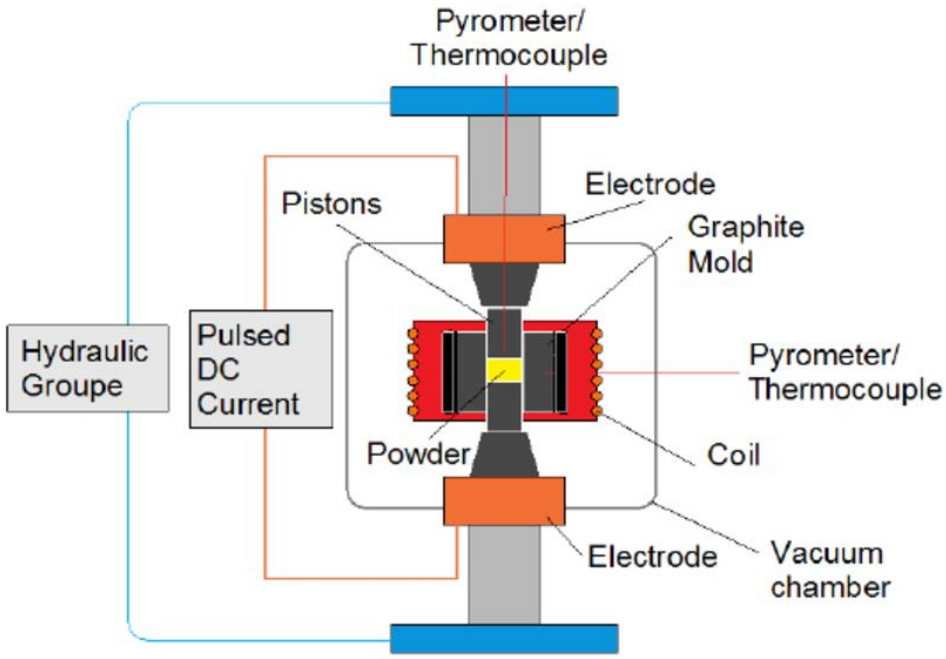

Figure II-7: Detailed illustration of the SPS configuration.[9]

2.2.2 Open Die Pressing (ODP)

Open Die Pressing (ODP) is an original sintering technique developed by the Institute of condensed matter chemistry and technologies for the energy (ICMATE) of the National Research Council (CNR). The powdered material is placed inside a cylindrical sheath of Fe (low expansion coefficient) covered internally with BN to prevent the attachment of the same to the shealth and as a protection for chemical diffusion. The cylindrical shealth, after a quick preheating at the processing temperature in an oven, is placed between two heated plates to maintain the temperature during the whole process and

pressed by compressive load for 30 seconds along the direction perpendicular to that of the length of the tube. After deformation, the sample is kept under load at the same temperature for a few minutes, in order to obtain the complete sintering of the powders.[10] Peculiar aspects of this technique are simplicity, easy scalability, as it is possible to process from a few grams to hundreds of grams of material at a time obtaining a good reproducibility of the results, and the economy. The characteristics of the process, speed and lower temperatures compared to other sintering techniques, allow the realization of nano-structured bulk with limited or absent grain growth or dispersion of nano-inclusions. Furthermore, the technique induces a high degree of texture in the bulk product, allowing, for anisotropic materials, the possibility of exploiting the anisotropy for the optimization of the final properties. Detailed illustration of ODP technique is reported in Figure II-8.

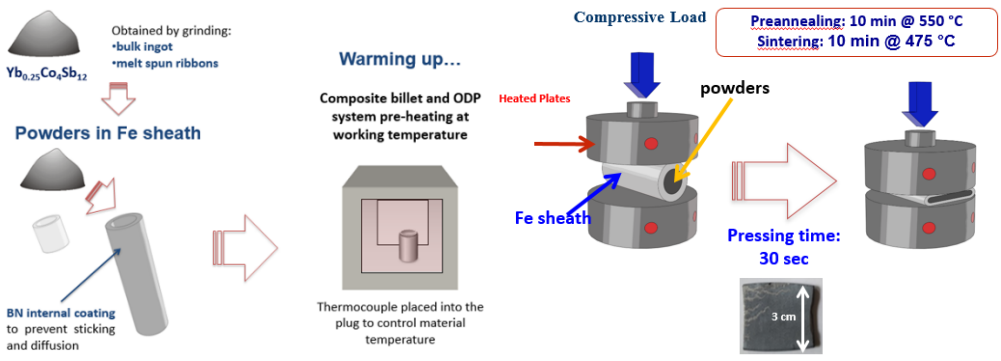

Figure II-8: Detaied illustration of the ODP technique. The processing parameters refers to the sintering of Yb-filled $CoSb_3$ skutterudite.

2.2.3 Electro-Sinter-Forging (EFS)

Electro-Sinter-Forging is an industrial sintering technique that with a single electromagnetic pulse allows to rapidly produce a wide range of small metallic components, based on alloys, intermetallics, hard metals and composites. The ESF technique was developed by the EPos company[11]. The ESF differs from other sintering techniques by:

- Pulse type and duration, a single pulse with low voltage (<50 V) and high current density (> 0.5 KA / mm^2) with a pulse time of around 30 ms.

- Overlap of a mechanical pulse to the electromagnetic one in the same time interval.

- Absence of a controlled atmosphere.

- High repeatability proposed by the solid state power circuit generating the pulse.

The consolidation is obtained by means of a single electromagnetic pulse and two axis to high-speed, numerically controlled to apply a mechanical pulse synchronized with the electromagnetic pulse (as shown in figure II-9).[12]

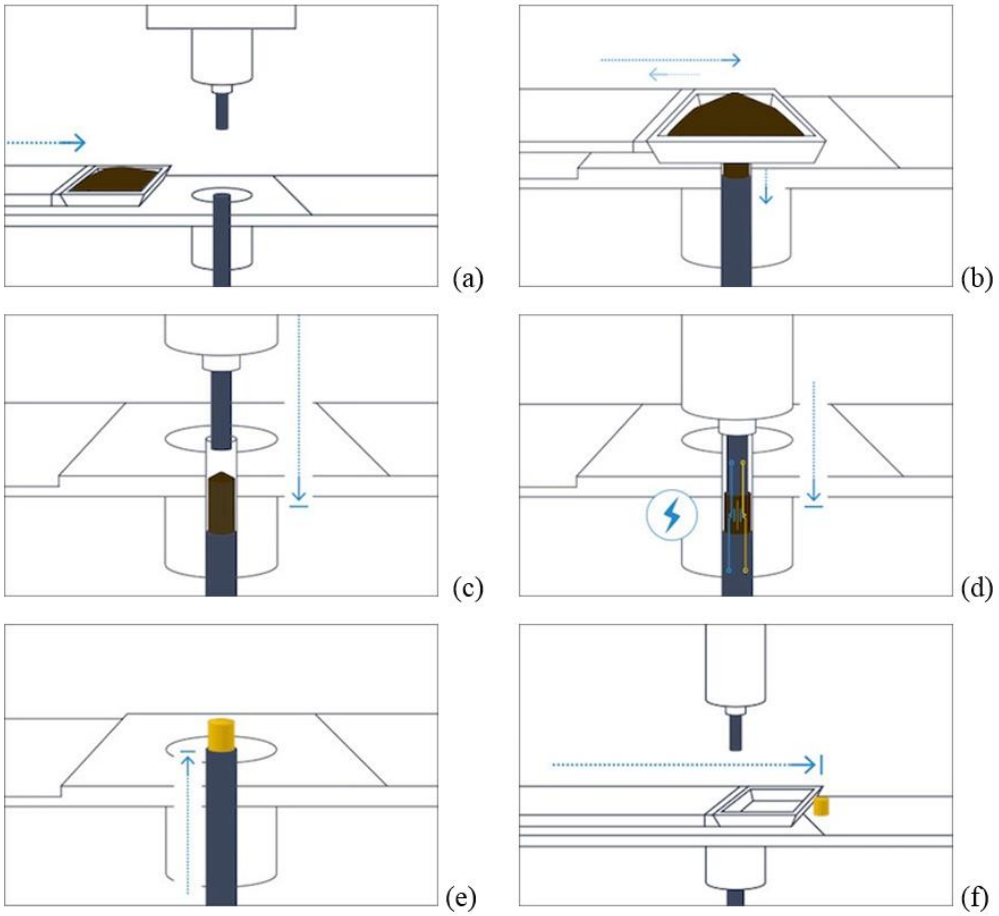

Figure II-9: Sequence of the steps used in the ESF technique to obtain a bulk sample from powders[11]

2.3 Characterization techniques

2.3.1 Structural characterization

- **X-Ray Diffraction (XRD)**

X-Ray powder diffraction is a rapid analytical technique primarily used for phase identification of a crystalline material and can provide quantitative information on the phases (lattice parameter, mutual

quantitaty, coherent scattering domains, defects). The analyzed material is finely ground, homogenized, in order to obtain averaged composition of the whole sample. The diffraction is based on Bragg diffraction, which occurs when radiation, with a wavelength comparable to atomic spacings, is scattered in a specular way by the atoms of the crystalline system and undergoes constructive interference. For a crystalline solid, the waves are scattered from lattice planes separated by interplanar distance *d*. When the scattered waves interfere constructively, they remain in phase since the difference between the path lengths of the two waves is equal to an integer multiple of the wavelength. The path difference between two waves undergoing interference is given by $2dsin\theta$, where θ is the scattering angle, as shown in Figure II-10.

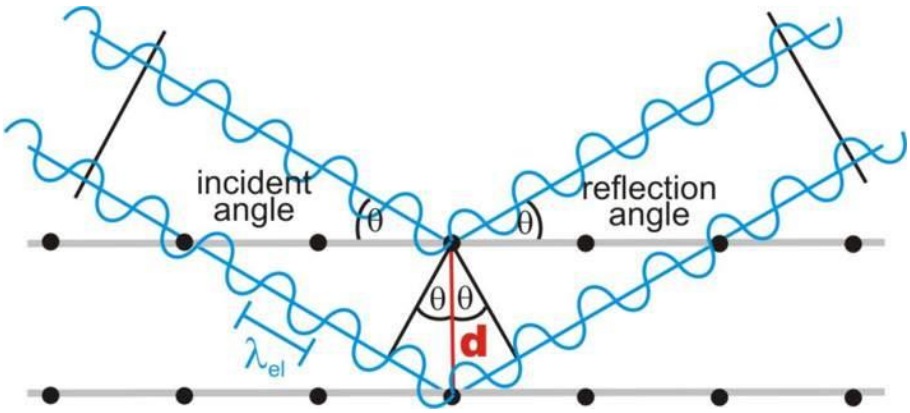

Figure II-10: Schematic illustration of Bragg scattering

The effect of the constructive or destructive interference because of the cumulative effect of reflection in successive crystallographic

planes of the crystalline lattice (as described by Miller notation). This leads to Bragg's law,

$$2d_{hkl}\sin(\theta) = n\lambda \qquad \text{(II-1)}$$

where *h, k, l,* are Miller indices, n is a positive integer and λ is the wavelength of the incident wave. Note that moving particles, including electrons, protons, and neutrons, have an associated wavelength called De Broglie wavelength. A diffraction pattern is obtained by measuring the intensity of scattered waves as function of scattering angle. Very strongly intensities known as Bragg peaks are obtained in the diffraction pattern at the points where the scattering angles satisfy the Bragg condition. Diffraction peaks are associated with planes of atoms and Miller indices (hkl) are used to identify different planes of atoms.[13] The x-ray diffractometers used for structural characterization in this dissertation use both Bragg-Brentano (Panalytical X'Pert Pro) and parallel beam (Panalytical PW3020) geometries with Cu K_α radiation (K_α = 1.5406 Å).

(a)

(b)

Figure II-10: X'Pert Pro (a) and PW3020 (b) X-ray diffrattometers

- **Rietveld refinement**

The Rietveld refinement is a computer-based analytical technique for the characterization of crystalline materials. The Rietveld method uses a least squares approach to refine a theoretical line profile until it matches the measured profile (best fit). It considers and treats the whole pattern in order to match peak position, intensity and profile. At first, for a Rietveld refinement, it is essential to collect a good powder diffraction pattern. Factors to consider prior to data collection are the geometry of the diffractometer, the quality of the instrument alignment and calibration (i.e. instrumental function to be obtained with a standard material), the most suitable radiation and its wavelength, appropriate sample preparation and thickness, slit sizes, and necessary counting time. As much as possible on the sample composition, size, absorption or microstructure should be known in

order to carry on the refinement with a good starting model. The first step of the Rietveld analysis should be the identification of the phases present in the sample, considering both crystalline and amorphous contributions, and the first estimation of the relative amount considering the intensity of the peaks. Then, knowing the instrumental function, which takes into account various instrumental contributions to the pattern, the background should be carefully modelled. Either the background can be estimated by linear interpolation between selected points between peaks or it can be modelled by a poynomial function containing several parameters. When a good starting model it is manually obtained, the refinement can be run in order to optimize the background parameters and intensity. Then, the scale factor can be adjust and refined. After the background, the parameters related to the sample can be refined. Among the analytical peak-shape functions, the pseudo-Voigt approximation of the Voigh function is probably the most widely used.[14] The pseudo-Voigt function is a linear combination of Lorentzian and Gaussian components. An additional function to allow a more precise description of asymmetry due to axial divergence of the diffracted beam at low angles can be refined as well. With a complete structural model and a good starting values for the background contribution, the unit-cell parameters and the profile parameters, the Rietveld refinement of structural parameters can begin. It is usually advisable to start the refinement of structural parameters with the positions of the heavier atoms and then to proceed

with the lighter atoms. The scale, the occupancy parameters and the thermal parameters are highly correlated with one another, and are sensitive to the background correction. The thermal factor B is a thermal motion factor that can slightly tune the results, modifying the intensity and broadening of the reflections. In addition, the modification of size and strain of the crystallites can affect the broadening of the reflections. In conclusion, structure refinement using the whole-pattern Rietveld method is a powerful technique for extracting structural details from powder diffraction data but it is essential to proceed with careful and precise approach to obtain a good and reliable best fit. In this work, the Rietveld refinement of selected diffraction patterns has been performed using the MAUD program[15]. The instrumental function was determined using LaB_6 or Si as a standard.

- **Scanning Electron Microscopy (SEM)**

Scanning electron microscopy (SEM) is very useful technique for the microstructural analysis of materials[16]. It has a greater range of magnifications with respect to optical microscopy. In this dissertation microstructural observations were performed by Scanning Electron Microscopy (SEM) using a ZEISS EVO 50XVP-LaB_6 equipped with an Oxford instruments Inca-Energy 250 for energy-dispersive X-ray analysis (EDS). This SEM provides an LaB_6 cathode which when crossed by a current, generates a cloud of electrons in the head of the instrument (due to the thermionic effect). An acceleration device

(electron gun) through a potential difference (of the order of kV) sends the electrons towards the lower part of the instrument. These are conveyed onto the surface of the sample, with which they will interact, using magnetic lenses capable of confining and collimating them. When the electron beam hits the surface of the sample, the phenomena of interaction with the matter are multiple:

Formation of backscattered electrons (BSE) They are the result of elastic collisions of the inelastic electrons with the sample surface and they have energy close to the initial one. The intensity of the backscattered electrons is proportional to the atomic number Z, so the zones constituted by elements with high atomic weight appear lighter and brighter, while those composed of light elements are darker;

Secondary electron formation (SE) They are the result of inelastic collisions of the electrons with electrons belonging to the sample that are expelled from its surface. Unlike BSE, secondary electrons possess much lower energy because they lose a considerable fraction of them on their way to the surface, remaining involved in inelastic collisions. The secondary electrons give rise to a true image that represents the surface morphological structure of the sample under examination since the contrast is determined by the topographical characteristics of the surface. The image obtained also has a high depth of field and provides maximum resolution.

X-ray emission an electron of the primary beam can interact with the atomic structure of the sample ionizing it and displacing an electron from the innermost orbitals, the structure thus excited relaxes returning to its fundamental state through the emission of a photon X; the signal comes from very high depths (1-2 μm) and gives information regarding the composition of the sample. With this technique is also possible to perform quantitative analysis as the amounts of X-rays emitted is proportional to the concentration of the element itself, after calibration with a suitable metallic standard, using the Energy Dispersive X-ray (EDX) microprobe.

Figure II-11: Scanning Electron Microscopy (SEM) equipped with EDS microprobe

2.3.2 Thermal characterization

DSC, and TGA are two thermoanalytical techniques that allows to study materials by heating the sample in a controlled way[17]. These two

analyses can be carried out separately or simultaneously in the same instrument.

- **Differential Scanning Calorimetry (DSC)**

DSC follows the heat flow between the sample and a reference during heating or cooling in a controlled way. By measuring how the sample absorbs or releases heat with varying temperature, it is possible to study chemical reactions and sample thermal stability. Exothermic or endothermic phenomena are identified as peaks which can be integrated to estimate the relative variation in enthalpy. In details, a difference of thermic flow is registered between sample and a reference. This is related to the difference of temperature registered by thermocouples positioned at the sample and reference. The sample is placed in a crucible that is inert and stable with temperature. The same type of crucible with no sample is used as reference. A furnace is hermetically closed to isolate the measuring environment to avoid heat exchange with the surroundings. The measurement can be carried out in an inert atmosphere under a flux of inert gas, like N_2, Ar or He. The sample and the reference are heated or cooled at the same way and a difference of temperature between the reference and sample is measured when the sample undergoes an exothermic or an endothermic event. A dedicated software allows firstly to insert the temperature program for the measurement and then to collect and elaborate the data from the thermocouples. The DSC signal could be express as a function of temperature or time. Two types of instrument

exist, a power-compensated DSC or a heat-flux DSC. The first one measures the power needed to compensate the difference of temperature between sample and reference. The heat flow is then directly proportional to the difference of power registered because of the difference of temperature. Heat-flux DSC measures the difference of heat flow directly from the temperature difference between sample and reference registered by the thermocouples. The schematic representation of the two type of DSC instruments are reported in Figure II-12.

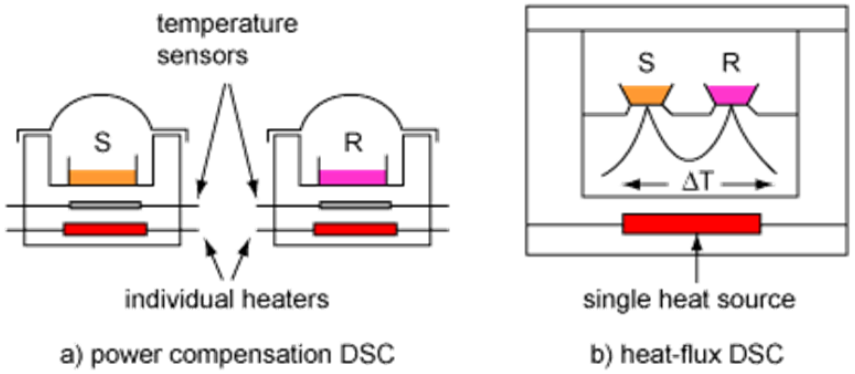

Figure II-12: schematic representation of the two type of DSC instrument. Power compensation (a) and heat-flux (b)

In this dissertation both heat-flux (TA-Q200) and power-compensated (Perkin Elmer DSC-7) DSC were used. The instruments were properly calibrated with standards. Nitrogen and argon were used as protective and purge gas at flow 100 ml/min. The measurements were performed using alumina pans.

 **(a)**  **(b)**

Figure II-13: TA-Q200 (a) Perkin Elmer DSC-7 (b)differential scanning calorimeters

- **Heat capacity measurement by differential scanning calorimetry**

In order to obtain accurate data to calculate a specific heat value at constant pressue for a given sample, three measurements are required: baseline, reference and analysed sample. All these measurements have to be performed with the exact same condictions: same crucible position, same measurement program and the same gas flow. In this dissertation specific heat capacity (Cp) was determined by differential scanning calorimetry, DSC (Perkin Elmer DSC 7), according to the following procedure. Heating ramps at 10 K/min were performed in a temperature range of 30 K. Each ramp was preceded and followed by a long isotherm in order to stabilize the signal. The measurement was repeated with the empty alumina pans, a standard (zaffire) and the sample. The specific heat of the sample, C_p^s , at different temperatures was obtained by comparing the signals measured for the sample and

the standard using the "height method" and the "area method" through the relationships

$$C_p^s = C_p^z \frac{(\Delta Y_s - \Delta Y_0)}{(\Delta Y_z - \Delta Y_0)} \frac{m_z}{m_s} \qquad \text{(II-2)}$$

where C_p^z is the specific heat of the standard, ΔY_s and ΔY_z are the calorimetric signals of the sample and the standard, respectively, ΔY_0 is the calorimetric signal of the empty pans, m_z and m_s are the mass of the standard and the sample, respectively, and

$$C_p^s = C_p^z \frac{(\Delta H_s - \Delta H_0)}{(\Delta H_z - \Delta H_0)} \frac{m_z}{m_s} \qquad \text{(II-3)}$$

Where C_p^z is the specific heat of the standard, ΔH_s and ΔH_s are the integrated areas under the calorimetric signals of the sample and the standard, respectively, ΔH_s is the integrated area under the calorimetric signal of the empty pans, m_z and m_s are the mass of the standard and the sample, respectively.

- **Thermogravimetry analysis (TGA)**

TGA measures the variation of weight during a controlled heating ramp. It is a destructive technique from which quantitative information is obtained. It is used to study the thermal and thermo-oxidative stability. The measurement can be conducted in a controlled inert or reactive atmosphere, depending on the type of study. The resulting thermogram displays the variation of mass in percentage or absolute value as a function of time or temperature. The instrument

includes a precision balance with a sample pan located inside a furnace with a programmable control temperature. The sample has to be weighed in a very accurate way, since the instrument balance is very sensitive and can measure mass changes of the order of μg. The schematic TGA instrument is reported in Figure II-14.

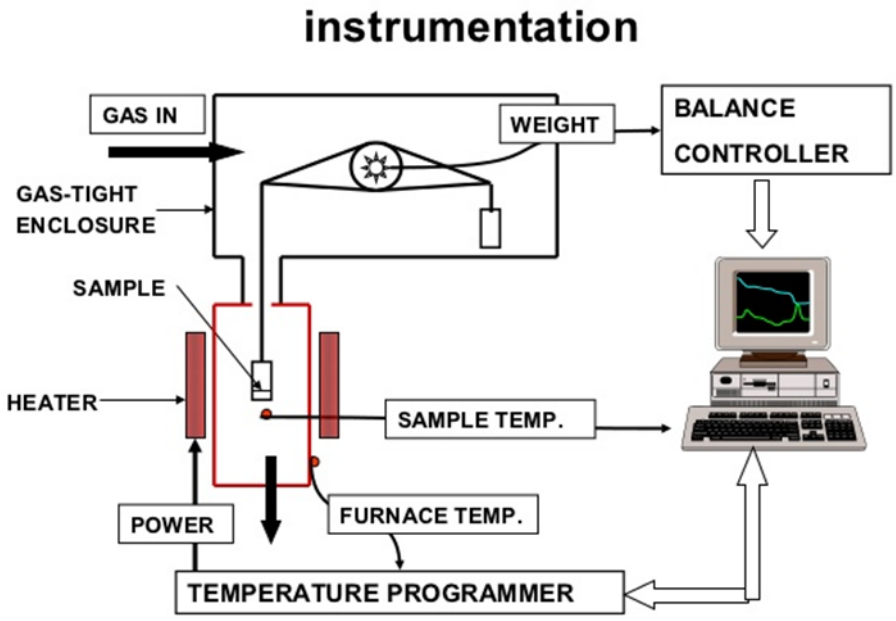

Figure II-14: Schematic TGA instrument

In this dissertation TA-Q600 instrument was used for thermogravimetric analysis.

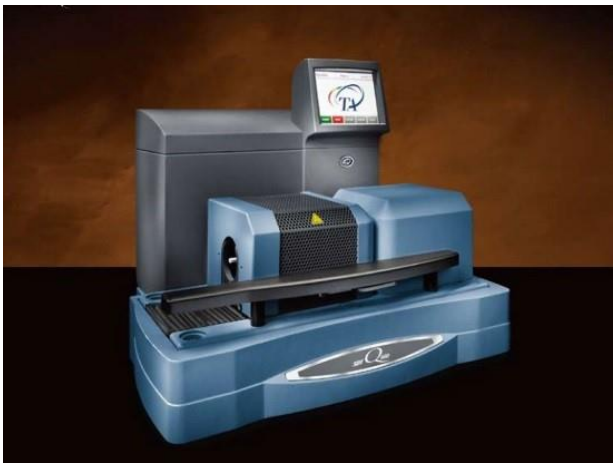

Figure II-15: TA-Q600 TGA

2.3.3 Thermoelectric characterization

As seen in the first chapter, the efficiency of a thermoelectric material is characterized by a dimensionless figure of merit defined as:

$$ZT = \frac{\alpha^2 \sigma}{k} T \qquad \text{(II-4)}$$

where α is the Seebeck coefficient, σ the electrical conductivity,, k the thermal conductivity and, T the absolute temperature. The thermal conductivity of a material, is given by the relationship:

$$k = \rho C_p D \qquad \text{(II-5)}$$

with ρ is the density of the sample, C_p is the specific heat at constant pressure and D its thermal diffusivity. As explained in chapter 1, the thermal conductivity is the addition of two contributions: the lattice thermal conductivity, k_{lat} (heat transfer occurring through elastic vibration of the lattice, also called phonons), the other phenomena is

the electronic thermal conductivity, k_{el} (heat is transferred by the carriers). The electronic thermal conductivity is given by

$$k_{el} = L\sigma T \qquad \text{(II-6)}$$

where L is the Lorenz number, widely used to estimate k_{el} from σ measurements. It is a common practice to treat L as a universal factor with a value of $2.44 \times 10^{-8} W\Omega K^{-2}$. However, significant deviations from the degenerated limit are known to occur for non-degenerated semiconductors where L converges to $1.5 \times 10^{-8} W\Omega K^{-2}$ for acoustic phonon scattering. The decrease in L is correlated with an increase in thermopower (absolute value of Seebeck coefficient). Thus, a first order correction to the degenerate limit of L can be based on the measured thermopower, $|\alpha|$, independent of temperature or doping. Kim et al. reported the approximate equation to calculate the Lorenz number[18]:

$$L = 1.5 + e^{-\frac{|\alpha|}{116}} \qquad \text{(II-7)}$$

where L is in $10^{-8} W\Omega K^{-2}$ and α in $\mu V K^{-1}$. The expression II-6 was used to calculate the electronic contribution to thermal conductivity when needed during our investigations. The ZT value can be directly obtained by a ZT-meter method[19]. However, a precise measurement of each individual parameter, in function of temperature, is of prime interest to understand the relationship between the microstructure and the thermoelectric properties of a given material. For this reason

below the different methods used to characterize the individual electronic and thermal properties of a bulk material, in function of temperature, are described.

- **Electrical conductivity and Seebeck coefficient measurements**

Even if some rapid techniques are available to directly measure ZT,[20] separate knowledge of thermal and electrical (Seebeck coefficient and electrical conductivity) transport properties is fundamental for functional characterization of thermoelectric material. For example, Seebeck coefficient, electrical conductivity and electrical contribution to the thermal conductivity are sensitive to doping and carrier concentration while the lattice contribution to the thermal conductivity is sensitive to structural and microstructural features. Furthermore, to develop and optimize a thermoelectric material, knowing these parameters is mandatory. For this is important to measure α and σ on a single sample, in the same direction, and possibly within the same measurement, thus avoiding different thermal histories. In this dissertation a test rig was used to measure the Seebeck coefficient and electrical conductivity of the samples investigated. The apparatus was developed by the Institute of Condensed Matter Chemistry and Technologies for the Energy (ICMATE) of the National Research Council (CNR) for simultaneous measurements of thermopower and electrical conductivity. Figure II-16 shows a scheme of the test rig apparatus.

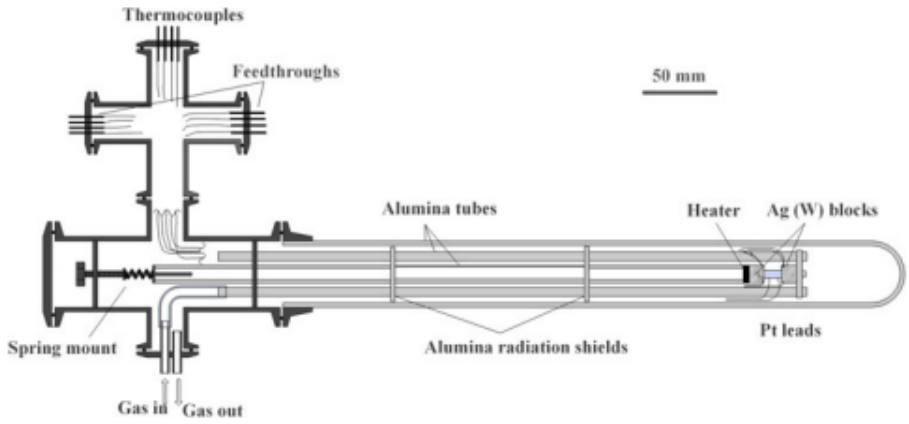

Figure II-16: Schematic illustration of test rig apparatus

The typical samples are in the form of 10-20 mm length rods or bars with section generally lower than 0.25 cm^2. The sample is placed between two Ag cylinders. One of the two metallic blocks is in thermal contact with a small heating coil. This heating coil is mounted on an alumina bar and pressed towards the sample by a spring mounting placed outside the furnace. The k-type thermocouples and the Pt leads are placed into small holes drilled into Ag blocks as close as possible to the surface in contact with the thermoelectric sample. Two Pt leads are connected directly to the sample for the conductivity measurements. The choice of employing Ag and W for higher temperature was based upon their thermal diffusivity and also on their volumetric heat capacity as described in Ref. 21. The apparatus is inserted into a fused silica tube, sealed with high temperature epoxy to a flange connected with the low temperature stainless-steel body, which contains the spring mounting and the connections to

instruments, pump and gas lines. The measurement operations are carried out while the furnace slowly increases (or decreases) the temperature of the system, normally at a rate generally lower than 2 $Kmin^{-1}$. All the procedures and the data processing are performed by a specifically made LabView program. The conductivity measurement, performed in a four-wire configuration, takes place as follows: a signal sequence formed of positive and negative alternating current short pulses is imposed onto the silver blocks, and the voltage between the two probes on the sample is recorded by a nanovoltmeter (Keithley 2182A). This allows to eliminate the additional thermopower caused residual thermal gradients in the sample or produced by the heat flow induced by the measurement current. The conductivity is then calculated from the resulting resistance value R as

$$\sigma = \frac{l}{RA} \qquad \text{(II-8)}$$

where l is the distance between the probes and A is the transversal section of the sample.

Immediately after the previous step, the LabView software controls the heater to increase the temperature of the hot side block. After a few seconds, the thermoelectric voltage is measured by the nanovoltmeter between the Ag blocks as a function of their temperature difference for a time set to allow for partial thermalization

of the system (generally some tens of seconds). The slope of the resulting line, α_M, enables calculation of the thermopower as

$$\alpha_{TE} = \alpha_{Pt}\text{-}\alpha_M \qquad \text{(II-9)}$$

being α_{Pt} the Seebeck coefficient of Pt leads at the average temperature of the measurement. The measurement cycle ends with a time of the order of minutes to allow for complete thermalization before the next measurement.

- **Thermal diffusivity measurement**

The thermal diffusivity of the bulk samples was determined using the laser flash method.[22,23] It is difficult to evaluate this parameter correctly due to surface heat loss and laser flash method has been proved to give more precise results. During such a measurement, the front surface of a parallelepipedic or cylindrical sample is heated by a laser pulse (up to 18 J, ≈ 300 μs FWHM), while the temperature emerging from the rear surface is measured using an infra-red InSb detector, as shown in Figure II-17.

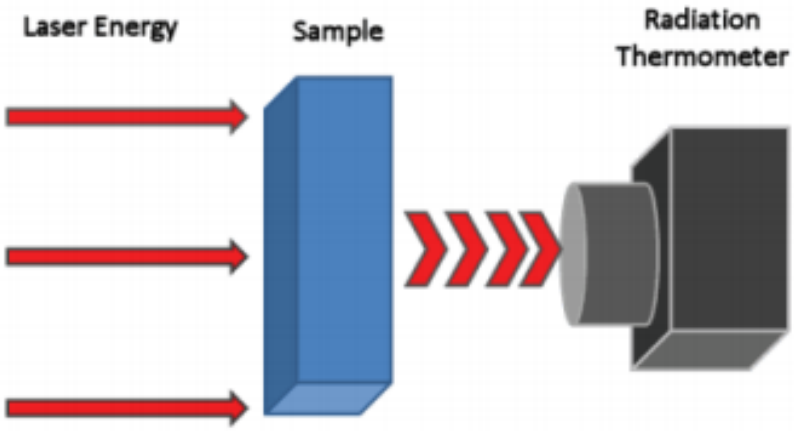

Figure II-17: Laser flash method

The temperature versus time graph is plotted. Eventually, the temperature increases to a limit T_{max}. The thermal diffusivity, D, is then determined using the expression:[24]

$$D = \frac{1.37}{t_{1/2}} \frac{d^2}{\pi^2} \qquad \text{(II-10)}$$

where d is the sample thickness and $t_{1/2}$ is the time needed by the rear surface to reach the temperature $T_{max}/2$, being T_{max} the maximum temperature recorded by the IR detector from the rear surface. It is important to notice that the laser flash apparatus can also be used to measure the specific heat at constant pressure.[22] However, in this dissertation, DSC was used as described previously. For our investigations, square samples 10 x 10 mm^2 and from 2 to 3 mm thickness, were entirely covered by a thin graphite layer, in order to maximize heat absorption from laser and surface emissivity at the detector side of the sample. Afterwards, they were mounted on a SiC

sample holder and placed into a LFA-457 MicroFlash apparatus (Figure II-18). All the measurements were completed under argon atmosphere.

Figure II-18: LFA 457 MicroFlash equipment

The analysis software available on the equipment proposes various models to fit the experimental data to determine a precise value of the diffusivity. In our case the Cape-Lehman theoretical model is used.[23]

- **Carrier density and mobility measurement**

Van Der Pauw and Hall measurements have been performed using a MMR instrument. The system is composed by a Al vacuum chamber equipped with a Joule-Thompson temperature controller. The thermal stage operating range is 70K-700K. On the surface of the stage, a squared sample is mounted using thermal paste for the thermal

coupling. The samples dimensions range between 4 and 10 mm for the side and between 0.4 and 2 mm in thickness. The samples are electrically connected with thin (0.125-0.2 mm) copper wires on the corners of the square using silver paste. This configuration allows resistivity measure of the samples using Van Der Pauw method. The same configuration is used for Hall measurements. Three steps are necessary for the result: a starting measurement of the resistivity by Van Der Pauw without magnetic field applied is followed by cross measurement with magnetic field applied in the two directions (positive and negative fields) across the squared surface of the sample. The three steps allow to determine for each temperature the resistivity of the sample, its carrier concentration, associated to the character (electrons or halls), and the carrier mobility. The equation used for the results determination are:

$$R = \frac{V_2\text{-}V_1}{I_2\text{-}I_1} \qquad \text{(II-11)}$$

where Vi are voltages and Ii currents where I2 and I1 are taken with opposite polarity. The resistance R is the one collected applying the current to two opposite contacts across the sample and measuring the voltage on the other two probes. This allows to define for each side of the sample the ratio:

$$X = \left|\frac{R_{12,34}}{R_{23,41}}\right| \qquad \text{(II-12)}$$

To obtain the resistivity of the sample the Form Factor is calculated as:

$$F = \frac{-2 \ln 2}{\ln a + \ln(1-a)} \qquad \text{(II-13)}$$

where a satisfies the equation a^Z=1-a with Z = X if X ≤ 1 and Z = 1 / X if X > 1.

The resistivity is so derived as:

$$\rho = \frac{\pi d F \left(R_{12,34} + R_{23,41}\right)}{2 \ln 2} \qquad \text{(II-14)}$$

where d is the thickness of the sample. The value is calculated for each side and averaged for each temperature. For mobility, μ, calculation, the equation is:

$$\mu = \frac{10^8 \left(\Delta R_{13,24} + \Delta R_{24,31}\right) d}{2 \rho \Delta B} \qquad \text{(II-15)}$$

with ΔB the external magnetic field applied producing ΔR13,24 and ΔR24,31. So the carrier density is calculated as:

$$n = \frac{1}{e \rho \mu} \qquad \text{(II-16)}$$

The apparatus used is reported in Figure II-19

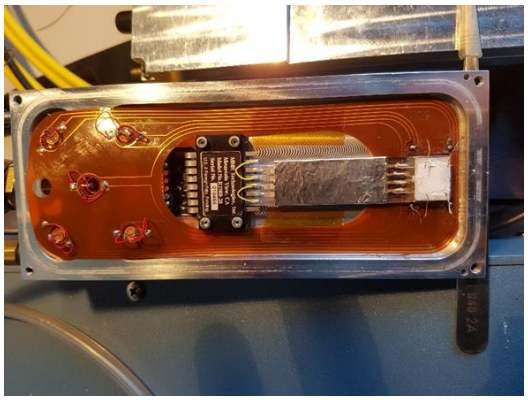

Figure II-19: MMR instrument

References

1. Jin, Y. L. *et al.* Phase composition and nanostructure of Zr2Co11-based alloys. in *Journal of Applied Physics* (2014). doi:10.1063/1.4867226

2. Jin, Y., Fan, X., Men, H., Liu, X. & Shen, B. FePCCu nanocrystalline alloys with excellent soft magnetic properties. *Sci. China Technol. Sci.* (2012). doi:10.1007/s11431-012-4928-0

3. Inoue, A., Ohtera, K., Kita, K. & Masumoto, T. New amorphous Mg-Ce-Ni alloys with high strength and goodductility. *Jpn. J. Appl. Phys.* (1988). doi:10.1143/JJAP.27.L2248

4. Burmeister, C. F. & Kwade, A. Process engineering with planetary ball millss. *Chem. Soc. Rev.* (2013). doi:10.1039/c3cs35455e

5. Costa, P. Nanomatériaux - Structure et élaboration. *Tech. l'Ingénieur* (2001).

6. Abdellaoui, M. & Gaffet, E. Mechanical alloying in a planetary ball mill: kinematic description. *J. Phys. IV JP* (1994).

7. Du, B. *et al.* Flash spark plasma sintering of magnesium silicide stannide with improved thermoelectric properties. *J. Mater. Chem. C* (2017). doi:10.1039/c6tc05197a

8. Gonzalez-Julian, J. *et al.* Effect of Internal Current Flow during the Sintering of Zirconium Diboride by Field Assisted Sintering Technology. *J. Am. Ceram. Soc.* (2016). doi:10.1111/jace.13931

9. Yushin, D. I., Smirnov, A. V., Solis Pinargote, N. W., Peretyagin, P. Y. & Torrecillas San Millan, R. Modeling process of spark plasma sintering of powder materials by finite element method. *Mater. Sci. Forum* (2015). doi:10.4028/www.scientific.net/MSF.834.41

10. Fanciulli, C., Codecasa, M., Passaretti, F. & Vasilevskiy, D. Effects of metal particles decoration on n-type chalcogenides processed by open die pressing. *J. Electron. Mater.* (2014). doi:10.1007/s11664-014-3052-2

11. https://www.eposintering.com/.

12. Fais, A., Actis Grande, M. & Forno, I. Influence of processing parameters on the mechanical properties of Electro-Sinter-Forged iron based powders. *Mater. Des.* **93**, 458–466 (2016).

13. Cullity, B. D. & Stock, S. R. Elements of X-ray diffraction, 3rd edition. *Prentice Hall* (2001). doi:citeulike-article-id:3998040

14. Balzar, D. Defect and Microstructure Analysis by Diffraction. *Powder Diffr.* (1999).

15. Lutterotti, L., S. Matthies, and H. R. W. MAUD: a friendly Java program for material analysis using diffraction. *IUCr Newsl. CPD* **21**, 14–15 (1999).

16. Goldstein, J. I. *et al. Scanning electron microscopy and x-ray microanalysis*. *Scanning Electron Microscopy and X-ray Microanalysis* (2017). doi:10.1007/978-1-4939-6676-9

17. R. F. Speyer. *Thermal analysis of materials*. (1994).

18. Kim, H. S., Gibbs, Z. M., Tang, Y., Wang, H. & Snyder, G. J. Characterization of Lorenz number with Seebeck coefficient measurement. *APL Mater.* (2015). doi:10.1063/1.4908244

19. Harman, T. C. Special techniques for measurement of thermoelectric properties. *Journal of Applied Physics* (1958). doi:10.1063/1.1723445

20. Harman, T. C., Cahn, J. H. & Logan, M. J. Measurement of thermal conductivity by utilization of the peltier effect. *J. Appl. Phys.* (1959). doi:10.1063/1.1735334

21. Boldrini, S. *et al.* Test rig for high-temperature thermopower and electrical conductivity measurements. *J. Electron. Mater.* (2013). doi:10.1007/s11664-012-2437-3

22. Parker, W. J., Jenkins, R. J., Butler, C. P. & Abbott, G. L. Flash method of determining thermal diffusivity, heat capacity, and thermal conductivity. *J. Appl. Phys.* (1961). doi:10.1063/1.1728417

23. Cape, J. A. & Lehman, G. W. Temperature and finite pulse-time effects in the flash method for measuring thermal diffusivity. *J. Appl. Phys.* (1963). doi:10.1063/1.1729711

24. Taylor, R. *In CRC Handbook of Thermoelectrics*. (1995). doi:10.1201/9781420049718

CHAPTER III:

PROCESSING AND PROPERTIERS OF Yb-FILLED Co_4Sb_{12} SKUTTERUDITES

3.1 Introduction

The origin of the name skutterudite derives from its place of finding, namely the cobalt mines in Skutterud (Norway), where the naturally occurring mineral $CoAs_3$ was firstly discovered and described.[1] Binary skutterudites have a general form of MX_3, where M is the metal atoms such as Co, Rh, Ir, and X represents the pnicogen atom such as P, As, and Sb. It comprises a cubic structure (Body-centered-cubic) with 32 atoms corresponding to the space group $Im\bar{3}$, where the transition metals occupy the 8c-sites (1/4, 1/4, 1/4) and the pnicogen atoms the 24g-sites (0, y, z), respectively.[2] The pnicogen atoms form a rectangle (four-membered ring) and enclose the transition metal in an octahedral coordination, as shown in Figure III- 1. Furthermore *Jeitschko et al.*[3] have shown that the skutterudite structure can be modified by insertion of maximal two additional atoms, which fill the 2a vacant sites (0,0,0) of the unit cell and occupy a body-centered position in the cubic structure.

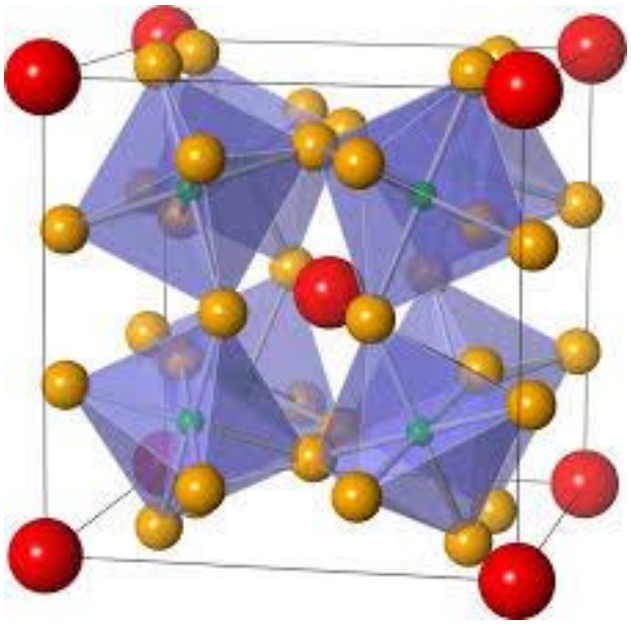

Figure III- 1: Schematic illustration of a filled skutterudite crystal structure (transition metal M in green, pnicogen X in orange, filler atom in red). The unit cell shows the octahedra, which are formed by the pnicogen atoms and surround the transition metal.[4]

Generally, binary skutterudites are semiconductors with small bandgaps ~0.1 eV, high carrier mobilities and modest Seebeck Coefficients but very high thermal conductivities. The open structure is the key to their potential for thermoelectric applications. Filling the voids with foreign atoms could possibly depress the lattice thermal conductivity dramatically and modify the electronic properties to enhance the figure of merit.[5] Since there are two relatively large voids in the unit cell, the cubic unit cell can be written in a general way as $\square_2M_8X_{24}$, where □ represents a void. Filled skutterudites have been formed where rare earth[6,7], alkaline[8] and alkaline-earth[9,10], IIIA[11,12] and IVA[13] ions interstitially occupy these voids. Filled skutterudites can have high electrical conductivity like a crystal and low thermal

conductivity like a glass, which make them excellent thermoelectric material according to the phonon glass electron crystal (PGEC) concept. The atomic displacement parameter (ADP) is known as the measure of the mean-square displacement amplitude of an atom about is equilibrium lattice site. The magnitude of the ADP depends on how vigorously the atoms are vibrating and possible also on whether any static disorder is present on the site. From the first time filled skutterudites were synthesized, large X-ray atomic displacement parameters (ADP) have been reported for the guest ions, indicating that they may rattle or participate in soft phonon modes in the voids. The ADP values of the ions increase with decreasing ionic size. It is possible that, if the caged ions are smaller than the void, they may rattle and interact randomly with the lattice phonons resulting in substantial phonon scattering. The ADP dependence on temperature measured on $La_{0.75}Fe_3CoSb_{12}$ as shown in Figure III- 2. The ADP values of La are large and have strong temperature dependence. This indicates that La is rattling about its equilibrium position and is thereby creating localized dynamic disorder. The dynamic disorder is the cause of the unique thermal transport in these compounds.

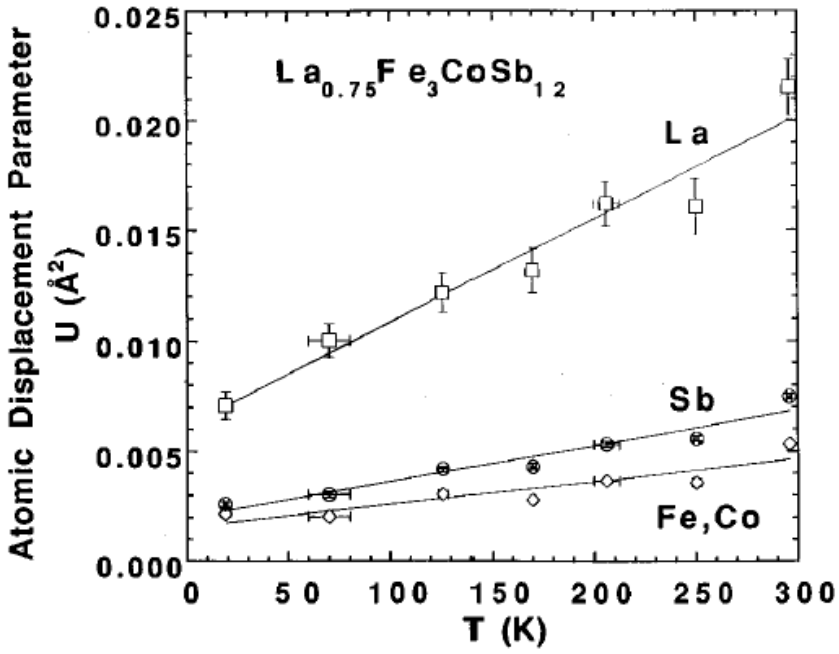

Figure III- 2: Atomic displacement parameters obtained on a single crystal $La_{0.75}Fe_3CoSb_{12}$[14]

3.2 State of the art and aim of the work

Study of binary skutterudites for thermoelectric purposes started in the 1950s, and soon it was realized that even though they have high electrical conductivity and large Seebeck coefficient, their high thermal conductivity limits their application as thermoelectric materials[15–17]. Skutterudites have two interstitials which allow foreign atoms to actively fill the structure, as previously reported in the paragraph 4.1[3]. In fact, the presence of two large interstices inside the elementary cell allows to insert interstitial atoms such as lanthanides[6,7]

or alkaline earth metals,[10,18] acting as phonon scattering centres. The filler content is ruled by electronic issues.[19–23] Skutterudites based on the elements of the group 9 (Co, Rh, Ir) and pnictogen elements (P, As, Sb) are electronically stable and can be only partially filled according to the valence state of the filler ion. In the case of Co_4Sb_{12}, Yb is one of the ideal filler species, due to its heavy mass and small radius compared to others. Conversely to trivalent lanthanide ions, Yb allows to optimize electronic properties as a consequence of the mixed valence state (Yb^{2+} and Yb^{3+}).[6,21] It was shown that the contribution of Yb^{2+} ion increases with the Yb occupancy factor in the cell,[23] allowing the extension of the solubility range of the filler. The effect of the filler amount in $Yb_xCo_4Sb_{12}$ on the thermoelectric properties was studied by several authors.[24–33] The solubility of Yb in the skutterudite cell depends on the synthesis process,[33,34] the temperature and the Co/Sb ratio.[26] The actual amount of Yb in the cell is usually lower than the nominal one,[21,35] due to its volatility and tendency to form oxides, affecting thermoelectric performance. The desired amount of Yb in the compound can be attained by adding an excess of Yb (30-50 mol.%).[21,35] A step forward for the commercial exploitation of skutterudites in thermoelectric applications is to establish a reliable, reproducible and affordable processing route. Skutterudites processed directly from the melt are affected by solidification segregation, originating from the formation of dendrites of the primary phase (CoSb) and the peritectic reactions, as shown by

the binary phase diagram (Figure III- 3) that induces porosity, chemical inhomogeneity, secondary phase formation, incomplete filling of the skutterudite cell, and, consequently, poor thermoelectric performances[29,33].

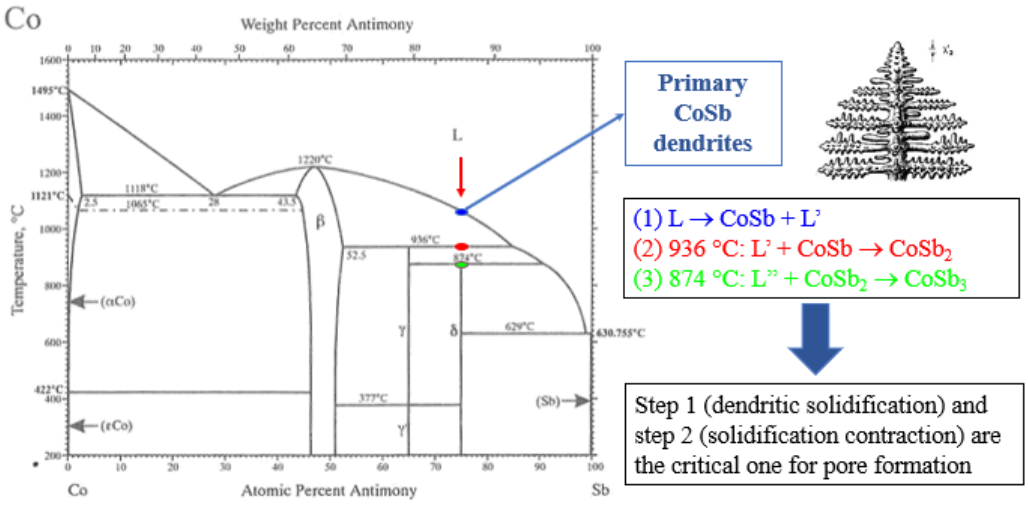

Figure III- 3: Co-Sb (cobalt-antimony) phase diagram [36] *and solidification path.*

Possible solutions to this problem are:

1) performing a solid/liquid reaction between $CoSb_2$ and Sb[29]

2) stirring the liquid before casting[33]

3) cooling following an oscillating temperature gradient[37]

4) direct formation of the skutterudite by deep undercooling of the liquid through rapid solidification technique[38]

Rapid solidification allows to obtain refined microstructures, and in some cases, even amorphous phases.[39] The introduction of a high

density of interfaces in grain refined materials leads to a reduction of the lattice thermal conductivity with respect to coarse microstructures, obtained by conventional processing routes.[40] Our approach was to employ rapid solidification as an intermediate step in the processing of Yb-filled Co_4Sb_{12} and to evaluate its effect on the kinetics of single phase formation and Yb filling. Furthermore, the effect of the Yb filling on thermoelectric properties was critically discussed in the frame of a literature survey. Part of the results of this chapter were published in Ref. 41.

3.3 Experimental

Elemental Co (rod, 99.995%), Sb (shots, 99.999%) and Yb (powder, 99.9%) were weighed according to the nominal stoichiometry ($Yb_{0.25}Co_4Sb_{12}$) and placed into graphite coated quartz ampoules. The ampoules were sealed under vacuum (10^{-5}mbar) and placed in a muffle furnace for the following heat treatment:

1) slow heating (3 K/min) from room temperature to 1473 K

2) isotherm at 1473 K for 5 h (the ampoule was shacked every hour to guarantee homogenization of the melt)

3) free cooling in the furnace to room temperature

In this way, ingots of the master alloy were obtained. Rapid solidification of the alloy was performed by planar flow casting (described in chapter 2) where the master alloy ingot was induction

melted in a boron nitride crucible under Ar atmosphere and the melt was injected under a pressure of 0.2 bar onto a capper wheel rotating at 20 ms^{-1}, forming ribbons 20-30 μm thick. The cooling rate during the rapid solidification is estimated to be 10^5 Ks^{-1}. Phase evolution in master alloy ingots (bulk) and rapidly solidified samples (RS) was studied by isothermal annealing at 898 K for 1, 2, 4 days.

Powders for sintering were obtained by hand grinding in an agate mortar the following precursors:

- Master alloy ingots annealed 4 days at 898 K (powder 1)
- Rapidly solidified ribbons annealed for 4 days at 898 K (powder 2)
- As quenched rapidly solidified ribbons without annealing (powder 3)

Finally, the powders were sintered using two different sintering techniques ESF and ODP (described in chapter 2). On the one hand the powders 1 and 3 were sintered by ESF[42] obtaining samples ESF1 and ESF3 respectively. On the other hand the powders 1, 2 and 3 were sintered by ODP[43] obtaining samples ODP1, ODP2 and ODP3 respectively. In the ODP, powders were loaded in Fe sheath, preheated at 823 K for 10 min before sintering between two heated plates at 748 K for 10 min applying a load of 200 MPa. At the end of the ODP sintering procedure, load was released and heating of the plates was switched off. In the case of samples ODP1 and ODP2, the samples

were slowly cooled between the plates passing from 748 K to 373 K into 2 h, while in the case of ODP3 the sample was subjected to free cooling, covering the same temperature gap in 30 min. Structural characterization was carried out by X-ray diffraction (XRD). The values of lattice parameter and Yb occupancy factor at 2a site in the skutterudite cage were refined by Rietveld method using the software MAUD[44]. The microstructure and chemical composition were monitored by SEM/EDX. Thermoelectric properties of the ODP sintered samples were measured as a function of temperature. ODP2 was measured up to 873 K, while ODP3 was measured up to 688 K (below the sintering temperature) in order to avoid the annealing of the sample and preserve the microstructure obtained after sintering. Seebeck coefficient, α, and electrical conductivity, σ, were measured by means of a custom built apparatus[45], described in chapter 2, applying a heating ramp of 2 $Kmin^{-1}$ and working under He flow. The thermal conductivity was calculated according to the formula $k = D\rho C_p$, where D is the thermal diffusivity, ρ is the mass density and C_p is the specific heat capacity. The thermal diffusivity was measured by LFA, as described in chapter 3, under Ar flow. The mass density was evaluated by Archimedes' principle with a pycnometer and specific heat capacity was determined by DSC using height method and area method (described in chapter 3). Measurements were performed on ODP2 and ODP3 samples and the values of specific heat obtained for

the two samples with the two methods were averaged at each temperature.

3.4 Results and Discussions

3.4.1 Alloying

EDX analysis of the all samples revealed a ratio Sb/Co slightly larger than the stoichiometry (3:1), as reported in Table III- 1 and Table III- 2, indicating that equilibrium is attained in the two phases region ($CoSb_3$ + Sb), as shown by the isothermal section of the ternary phase diagram Yb-Co-Sb reported in Figure III- 4a. The lattice parameter of the filled skutterudite linearly scales with the amount of Yb solubilized in the cell, as shown in Figure III- 4b. The trend of the lattice parameters indicates that the solubility of Yb in the skutterudite depends on the Sb/Co ratio, as shown in Figure III- 4c.[26]

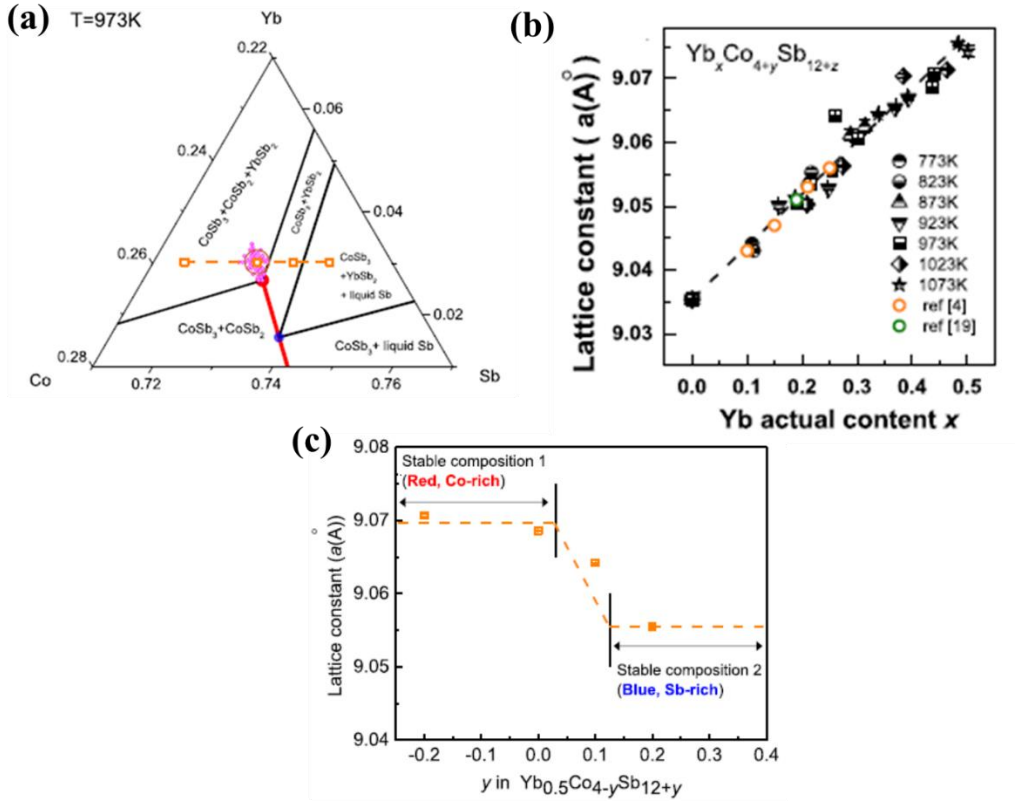

Figure III- 4: (a) Magnified region of the isothermal section at 973 K near $CoSb_3$ of the Yb-Co-Sb ternary phase diagram system with two stable skutterudite compositions (red and blue points) and solubility line (red line). Scattered points (empty magenta circles) indicate possible synthesis error near the stable composition (red point) in the three phases region of $CoSb_3$, $CoSb_2$ and $YbSb_2$. (b) Dependence of the lattice parameter on the actual Yb content, x, in $Yb_xCo_{4+y}Sb_{12+z}$. (c) Dependence of the lattice constant derived from X-ray Diffraction data on the Co/Sb ratio for nominal compositions with the same Yb content x = 0.5 marked as empty orange rectangles in (a).[26]

Even if close to the detection limit of the technique, the total amount of Yb measured by EDX (1.0-1.2 at.%) is lower than the expected equilibrium value (1.5 at.%), indicating that a fraction of the Yb powder was not successfully alloyed and confirming the difficulty to

maintain the Yb stoichiometry in the alloy, as already highlighted in Ref. 21 and Ref. 34.

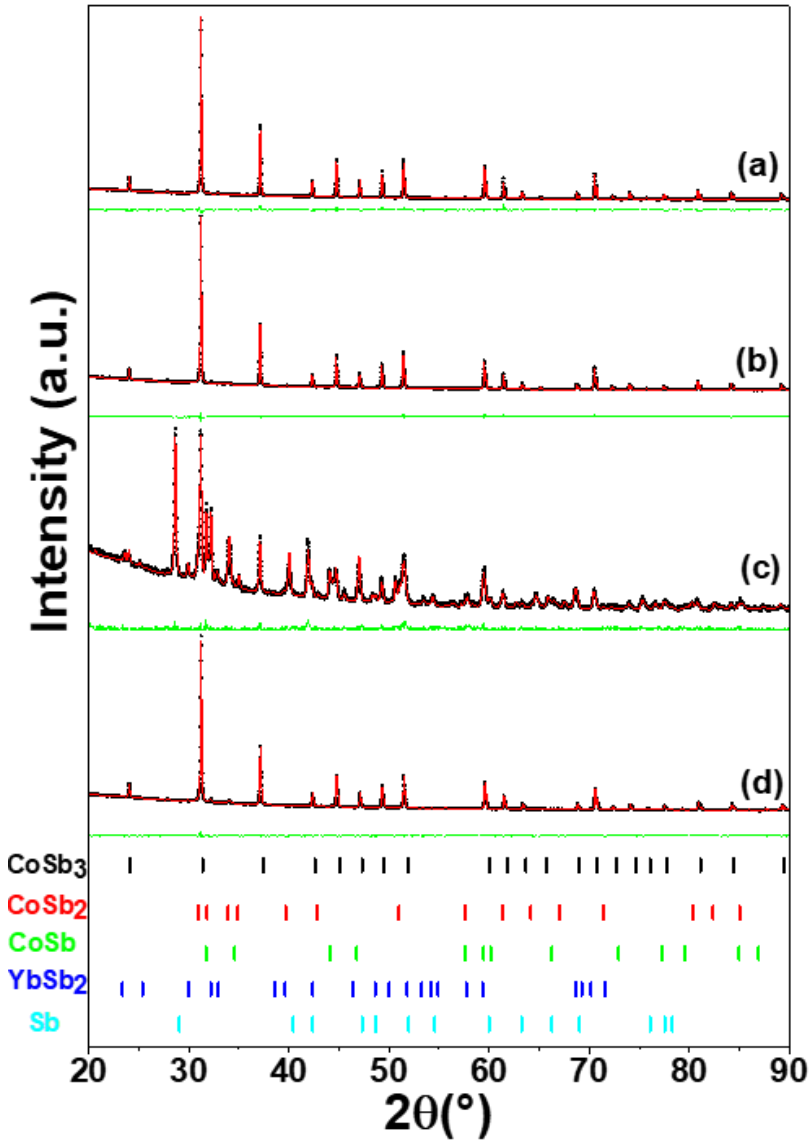

Figure III- 5: X-ray diffraction (XRD) patterns. (a) as prepared bulk ingots. (b) annealed (4 days at 898 K) bulk ingots. (c) as prepared rapidly solidified (RS) ribbons. (d) annealed (4 days at 898 K) rapidly solidified (RS) ribbons. Black points, red curves and green curves represent experimental data, refined patterns and differences between experimental and refined patterns, respectively.

The XRD pattern of the as prepared master alloy ingot (bulk), Figure III- 5a, shows only the crystallographic reflections of the $CoSb_3$ phase. However, backscattered electrons SEM micrographs of the same sample reveal the presence of the additional phases ($CoSb_2$, CoSb, $YbSb_2$) dispersed in the $CoSb_3$ matrix, as shown in Figure III- 6a, indicating that the alloy did not reach the equilibrium because of the slow kinetics of the peritectic reactions

$$CoSb + \text{liquid} \longrightarrow CoSb_2 \qquad \text{(III-1)}$$

$$CoSb_2 + \text{liquid} \longrightarrow CoSb_3 \qquad \text{(III-2)}$$

After annealing at 898 K for 4 days, the XRD pattern of the bulk shows only the crystallographic reflections of the $CoSb_3$ phase, Figure III- 5b. Again, backscattered electrons SEM micrographs of the annealed bulk, Figure III- 6b show the presence of the same additional phases ($CoSb_2$. CoSb, $YbSb_2$) observed in the corresponding as prepared sample, indicating that the alloy did not reach the equilibrium, even after annealing at high temperature. In the case of the as quenched ribbon, the XRD pattern, Figure III- 5c, reveals the presence of five phases ($CoSb_3$, $CoSb_2$, CoSb, $YbSb_2$ and Sb) indicating that the system is out of the equilibrium, as a consequence of the high cooling rate experienced by the alloy during rapid solidification. Figure III- 6c shows the SEM micrograph of the longitudinal cross section of the ribbon, obtained with the backscattered electrons detector. The lower edge of the ribbon is

smooth while the upper edge is rough, indicating that the former solidified in contact with the copper substrate (wheel side) and the latter solidified in contact with the argon atmosphere (free side). The micrograph is characterized by different levels of grey, indicating the presence of several phases, in agreement with the XRD pattern, Figure III- 6c.

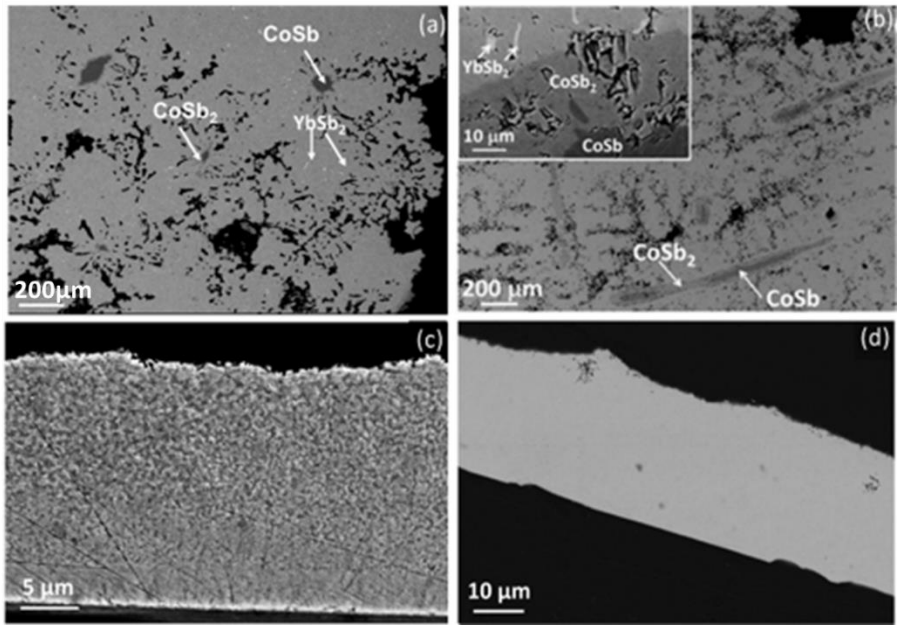

Figure III- 6: Backscattered electron SEM images. (a) as prepared bulk ingots. (b) annealed (4 days at 898 K) bulk ingot. (c) as prepared rapidly solidified ribbon (RS). (d) annealed (4 days at 898 K) rapidly solidified (RS) ribbon.

The microstructure becomes progressively coarser from the wheel side to the free side, because of the progressive reduction of the cooling rate from the wheel to the free side. After annealing the ribbon at 898 K for 4 days, the formation of a single phase is promoted, as shown by the XRD pattern, Figure III- 5d, and by the backscattered

electrons SEM micrograph, Figure III- 6d, that shows uniform grey contrast.

Table III- 1

Lattice parameter, a, Yb occupancy factor in the 2a site, Yb_{2a}, ratio (Yb_{2a}/Yb_{tot}) between Yb in the skutterudite cage, Yb_{2a}, and the total amount of Yb, Yb_{tot}, Sb/Co ratio as a function of the annealing time at 898 K ($Yb_{skutterudite}$). Lattice parameter and Yb_{2a} occupancy factor were determined by Rietveld refinement of the XRD patterns of *Figure III- 5*, the Sb/Co ratio was determined by EDX analysis.

Annealing time (days)	Bulk				Ribbon			
	a (Å)	Yb_{2a}	Yb_{2a}/Yb_{tot}	Sb/Co	a (Å)	Yb_{2a}	Yb_{2a}/Yb_{tot}	Sb/Co
0	9.0459	0.12(2)	0.76	3.40	9.0530	0.19(2)	0.98	3.30
1	9.0458	0.12(1)	0.75		9.0482	0.14(2)	0.72	
2	9.0471	0.12(9)	0.80		9.0522	0.18(4)	0.93	
4	9.0486	0.14(4)	0.90		9.0527	0.18(8)	0.98	

Table III- 1 shows the lattice parameter, the Yb occupancy factor in the 2a site and the ratio Yb_{2a}/Yb_{tot} in bulk and ribbon samples as a function of annealing time at 898 K. The bulk shows a progressive increase of the two parameters during annealing without levelling off at a constant value, suggesting that equilibrium is not reached even after 4 days of annealing, as shown in Figure III- 7, in agreement with literature data reporting that complete solubilization of Yb is accomplished after at least 7 days of annealing at 1073 K.[35,46] In the case of the ribbon, the values reported in Table III-1 drop after one day of annealing, subsequently increase reaching a plateau after 2-4 days of annealing, as shown in Figure III- 7, indicating attainment of the equilibrium.

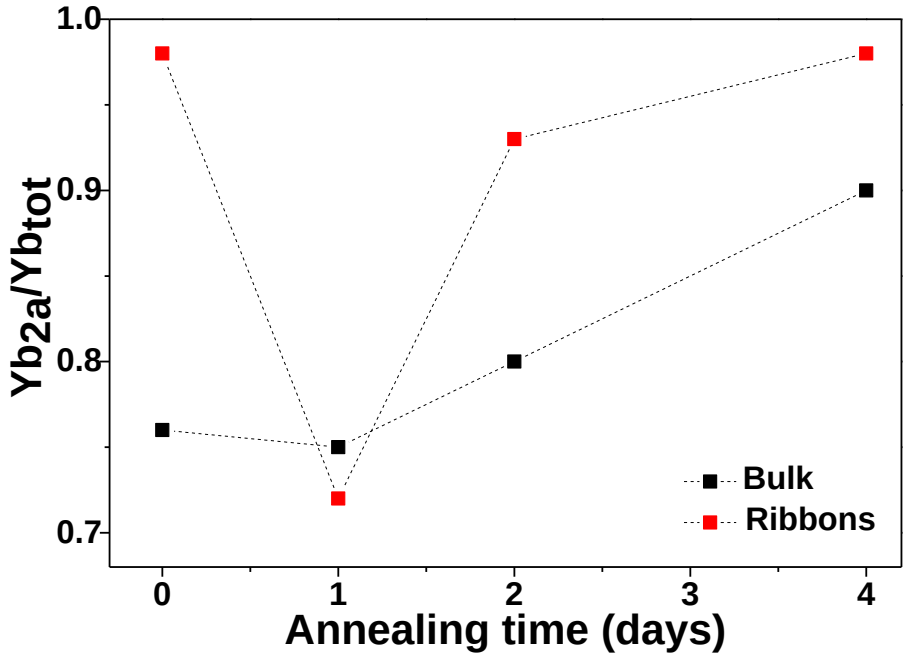

Figure III- 7: Ratio between the amount of Yb filling the skutterudite Yb_{2a} and the total amount of Yb in the alloy Yb_{tot} as function of the annealing time.

The larger amount of solubilized Yb in the as prepared ribbon is due to the quenching of the sample from a higher temperature where the Yb solubility is larger with respect to the annealing temperature[26]. The maximum amount of Yb solubilized in the skutterudite (around 0.19 for the ribbon annealed for 4 days) is lower than the stoichiometry (i.e. 0.25), indicating that about 25% of Yb was lost during processing, in agreement with the results of EDX analysis. The filling of the skutterudite cage occurs faster in the ribbon than in the bulk, as a consequence of the presence of a finer microstructure. The apparent diffusion coefficient, D_{app}[47], is given by

$$D_{app} = D_l + D_b \frac{\delta}{d} \qquad (III\text{-}3)$$

where D_l is the lattice diffusion coefficient, D_b is the grain boundary diffusion coefficient, δ is the grain boundary width and d is the grain size.

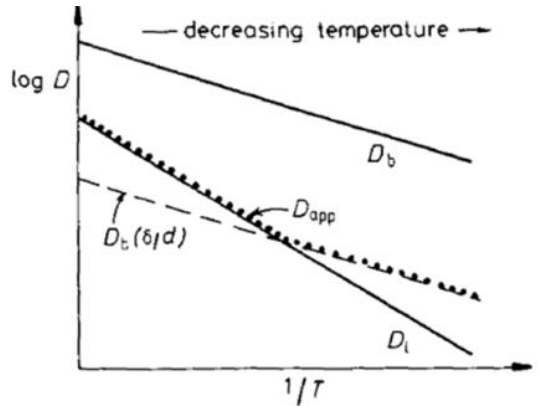

Figure III- 8: Effect of temperatures on diffusion in a polycrystalline material.

Figure III- 8b shows the effect of temperature on both D_l and D_b. although $D_b > D_l$ at all temperatures the difference increases as temperature decreases. This is because the activation energy for diffusion along grain boundaries is lower than that for lattice diffusion. This means that when the grain boundary diffusion is scaled by the factor δ/d the grain boundary contribution to the apparent diffusion coefficient is negligible in comparison to the lattice diffusion at high temperature but dominates at low temperature. In the case of the rapidly solidified ribbon, the grain size is around 0.1 µm, while for the bulk, grain size is of the order of several tenths of microns. Thus,

considering a constant value of the grain boundary width, the value of the δ/d ratio for the rapidly solidified ribbons is about two/three orders of magnitude larger than in the bulk, increasing the contribution of the grain boundary diffusion and the apparent diffusion coefficient in the ribbons. As a consequence, the filling of the skutterudite cell with Yb atoms during annealing occurs faster in the ribbon than in the bulk, confirming that rapid solidification can be used as an intermediate step to reduce the total processing time.

3.4.2 Sintering

- **Electro-Sinter-Forging (ESF)**

ESF samples were prepared varying the following processing parameters: starting pressure (P_{start}), maximum pressure (P_{max}), electromagnetic pulse (SEI). Table III-2 shows the values of the processing parameters for two representative samples.

From the definition of specific heat $C_p = \frac{dH}{dT}$, we can write $\Delta H = \int_{T_1}^{T_2} C_p dT$. Assuming a constant value of C_p (about 0.25 $Jg^{-1}K^{-1}$ [48]) over a wide temperature range, the equation becomes $\Delta H = C_p \Delta T$, where $\Delta T = T_2 - T_1$ is the temperature increase, T_1 and T_2 are the starting temperature (room temperature) and the maximum temperature of the sample, respectively, and ΔH is the enthalpy increase in the sample. Considering the ESF sintering as an adiabatic process, ΔH becomes equal to the specific energy input (SEI) due to the electromagnetic

pulse and an estimate of the adiabatic temperature increase (ΔT) and the maximum temperature (T_2) can be obtained.

Table III- 2

The starting pressure (P_{start}), the maximum pressure (P_{max}), the electromagnetic pulse (SEI) applied during the sintering process, the relative density, the ΔT adiabatic and the temperature (T) reached by the sintered samples during the process.

Sample	P_{start} (MPa)	P_{max} (MPa)	SEI (Jg^{-1})	ΔT	T (K)	Relative density (%)
EFS1	5	239	244	979	1004	82
EFS2	20	90.5	856	3424	3449	96

Figure III- 9 shows the XRD patterns of two of the several sintered samples (ESF1 and ESF2) obtained by ESF of powder 1, that were taken as a representative case.

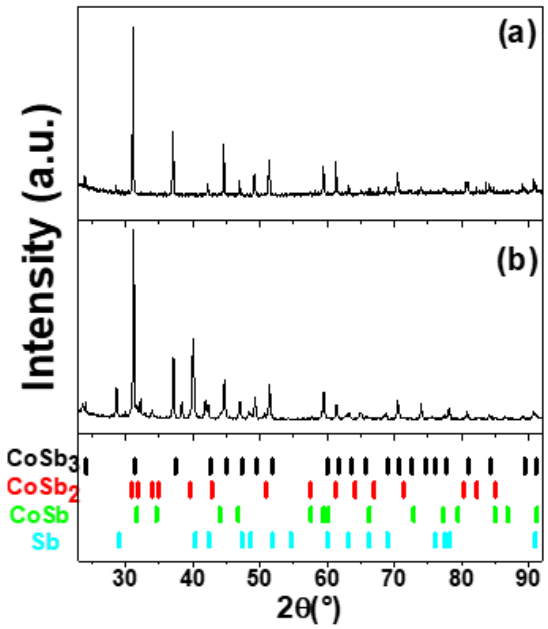

Figure III- 9: X-ray diffraction (XRD) patterns. (a) Sintered EFS1. (b) Sintered EFS2

The XRD pattern of the EFS1 sample, *Figure III- 9*a, shows only the crystallographic reflections of $CoSb_3$ phase. Backscattered electron SEM micrographs of the same sample, *Figure III- 10*a, in according to the XRD pattern shows uniform contrast but the sample did not show an effective compaction (82%) due to the use of too low starting pressure, as reported in Table III- 2. The XRD pattern of the EFS2 sample, shown in Figure III- 9b, reveals the presence of four phases ($CoSb_3$, $CoSb_2$, CoSb and Sb). Backscattered electrons SEM micrographs, Figure III- 10b, shows the presence of dendrites, indicating a passage in the liquid state, according with the maximum temperature estimate reported in Table III- 2.

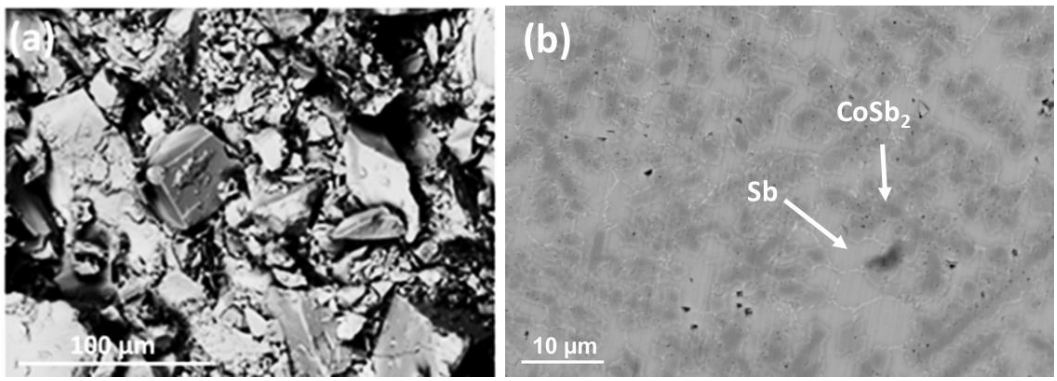

Figure III- 10: Backscattered electron SEM images. (a) Sintered EFS1. (b) Sintered EFS2.

- **Open Die Pressing**

The XRD patterns of the sintered samples show exclusively the crystallographic reflections belonging to $CoSb_3$, as shown in *Figure III- 11*, for ODP2 that was taken as a representative case.

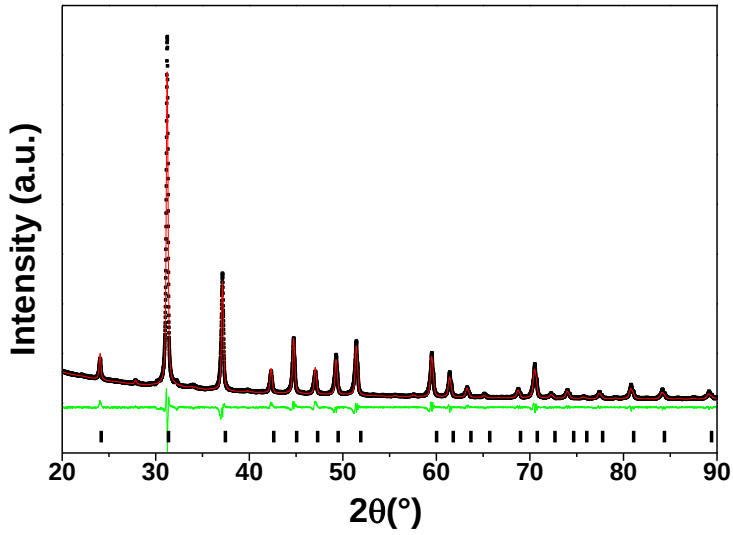

Figure III- 11: ODP2 sintered sample. Black points, red curves and green curves represent experimental data, refined patterns and differences between experimental and refined patterns, respectively.

However, SEM backscattered electron micrographs, *Figure III- 12*(a-c), reveal the presence of residual unreacted phases that are progressively less evident in ODP3 ($CoSb$, $CoSb_2$, Sb, $YbSb_2$), *Figure III- 12*c, ODP1 ($CoSb_2$, $YbSb_2$), *Figure III- 12*a, and ODP2 ($CoSb_2$, Sb, $YbSb_2$), *Figure III- 12*b.

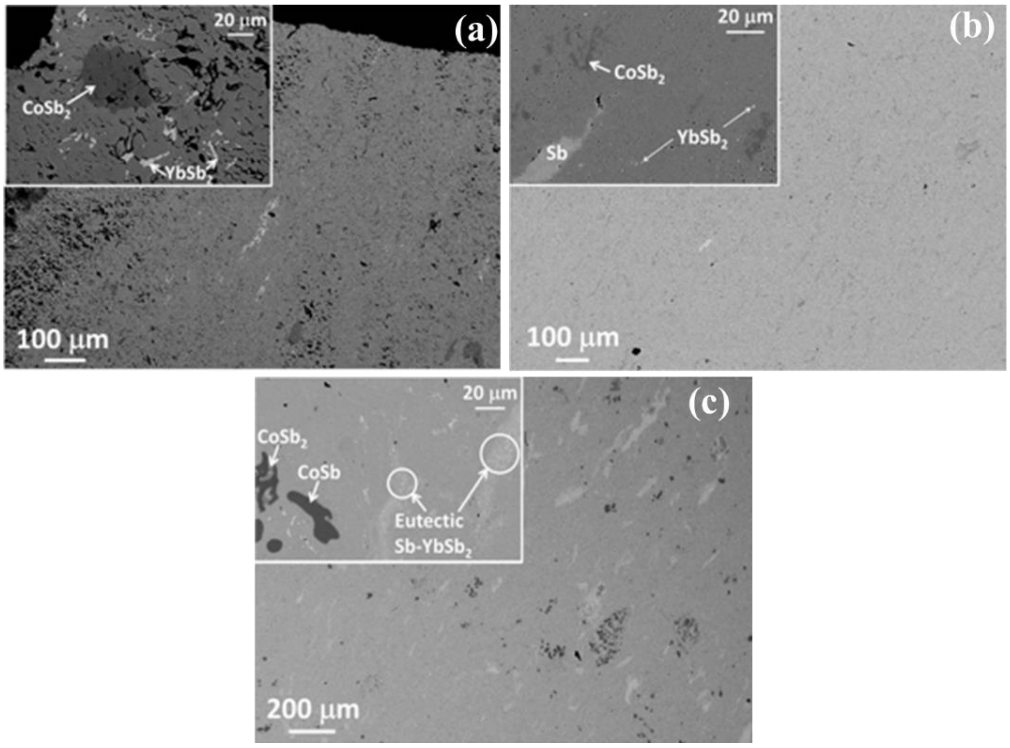

Figure III- 12: (a), (b) and (c) sintered ODP1, ODP2 and ODP3 samples, respectively.

In the case of ODP3, sintering of the starting multiphase powder (powder 3) promoted the homogenization of the sample forming an almost single phase dense massive material where some unreacted phases are still present, as shown in *Figure III- 12*c. Table III- 3 shows the values of the lattice constant and the Yb occupancy factor in 2a site for the sintered samples. In the case of ODP1 and ODP2, the values obtained after sintering are slightly lower than those of the starting powders (powder 1 and powder 2), Table III- 1, because the data refer to different batches. However, the ratio between

Yb_{2a}(ribbon)/Yb_{2a}(bulk) (about 1.30) is maintained in the corresponding ODP samples.

Table III-3

Lattice parameter, Yb_{2a} occupancy factor, relative density and Sb/Co ratio of the as sintered ODP1, ODP2 and ODP3 samples.

Sample	Lattice parameter (Å)	Yb_{2a} occupancy factor	relative density (%)	Sb/Co
ODP1	9.0478	0.13(6)	75	3.40
ODP2	9.0512	0.17(6)	95	3.24
ODP3	9.0462	0.12(6)	90	3.35

The amount of Yb dissolved in the skutterudite is not expected to be affected by the sintering process because this was performed at a temperature lower than the annealing of the starting materials. The value of Yb occupancy factor in ODP2 is very close to the maximum solubility at 900 K (0.19) reported in Ref. [26], indicating that the system is almost at the equilibrium. In fact, only small traces of unreacted phase ($CoSb_2$, Sb, $YbSb_2$) are still present after sintering, as shown in *Figure III- 12*b. In the case of ODP1, *Figure III- 12*a, the amounts of secondary phases are larger than in ODP2, as a consequence of the slower diffusivity in the bulk. The presence of secondary phases different from those predicted by the phase diagram,[26] indicates that phase equilibrium as well as equilibrium Yb solubility were not attained in ODP1. A similar consideration can be made for ODP3 where non equilibrium secondary phases are also present, *Figure III- 12*c. In addition, the lower values of lattice constant and Yb occupancy factor with respect to ODP1 and ODP2 can be further explained by the lower solubility of Yb in the

skutterudite at the temperature at which the sintering was performed.[26] The sintered samples show different values of relative density, as reported in Table III- 3. The significantly lower density of sample ODP1 (75%) with respect to ODP2 (95%) and ODP3 (90%) can be explained by the different particles size distributions of the corresponding starting powders, estimated by SEM image analysis, that are reported in *Figure III- 13*. In fact, a multimodal distribution of the particles size, here represented by the broader peak (ODP2 and ODP3), allows a better packing of the powders before the sintering process. The slightly larger value of relative density of ODP2 (95%) with respect to ODP3 (90%) is probably due to the slower cooling rate of the sample, that reduced the effect of internal stresses induced by the different thermal contractions of the metallic sheath and the thermoelectric sintered powders. Conversely ODP3, experiencing a faster cooling, suffered a compressing action at low temperature inducing a loss in compaction of the grown grains, inducing a residual micro-porosity in the bulk.

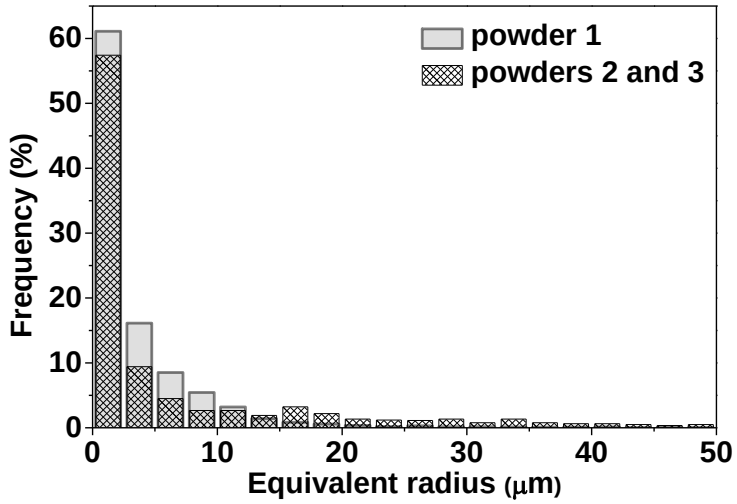

Figure III- 13: Particle size distribution for powder 1, obtained by grinding the annealed bulk ingot, powder 2 and powder 3, obtained by grinding annealed and as quenched rapidly solidified ribbons, respectively.

3.4.3 Thermoelectric properties

Thermoelectric properties were measured only on ODP2 and ODP3 because ODP1 and ESF1 show a value of relative density too low (75% and 82% respectively). ODP2 and ODP3 show similar values of the Seebeck coefficient as a function of temperature, *Figure III- 14*a, indicating an n-type behaviour and suggesting that the presence of secondary phases in ODP3 and the different levels of filling with Yb between the two samples is too small to significantly affect the thermopower. As recently reported, secondary phases affect thermoelectric properties of Yb-filled Co_4Sb_{12} skutterudites when they exceed a critical value (i.e. around 8 wt%).[49] Both ODP2 and ODP3 show decreasing values of the electrical conductivity, σ, as a

function of temperature, revealing a behaviour typical of heavily doped semiconductors, *Figure III- 14*b. This can be explained by the increased carrier concentration due to the filling with Yb.[28,31,35] However, ODP2 shows larger values of σ than ODP3. The effective electrical conductivity depends on the relative density of the sample and was calculated applying the Bruggeman symmetric model, where porosity is described as spherical inclusions.[50,51] For relative densities of 90% (ODP3) and 95% (ODP2), the calculated effective electrical conductivities are 0.85 and 0.925 times the electrical conductivity of the fully dense material, respectively. The ratio between the calculated effective electrical conductivities of ODP3 and ODP2 is 0.92, while the ratio between the corresponding measured electrical conductivities is 0.89 at room temperature and 0.92 at 688 K. The agreement between the calculated and measured values suggests that the different relative densities of ODP2 and ODP3 are responsible for the different measured electrical conductivities. *Figure III- 14*c shows thermal diffusivity, D, as a function of temperature. Both samples show similar trends with a minimum around 600 K, however ODP2 shows lower values of D with respect to ODP3. *Figure III- 14*d shows the values of the specific heat at different temperature. Each point was obtained averaging four values obtained by means of the "height" and "area" methods on ODP2 and ODP3 samples. The error bars represent the standard deviation and the relative error is lower than 5%, in agreement with the typical values for this technique. We can see that

at room temperature the specific heat approaches the limit given by the Dulong-Petit approximation (Cp = 3R). To extend the temperature dependence of the specific heat across a wider range, the experimental data were fitted according to the following expression.[52]

$$C_p = 3R + aT + bT^2 \qquad \text{(III-4)}$$

where R is the gas constant (8,314472 $Jmol^{-1}K^{-1}$), a and b are fitting parameters, which turn out equal to 3.13 10^{-3} K^{-1} and 9.15 10^{-6} K^{-2}, respectively. From the data of thermal diffusivity, density and specific heat, the thermal conductivity was determined at different temperatures according to the relationship $k = D\rho C_p$, as shown in *Figure III- 14*e. It can be seen that ODP2 and ODP3 show similar values between 300 K and 500 K, then above 500 K thermal conductivity of ODP2 becomes lower than the one of ODP3. The total thermal conductivity, k, is given by $k = k_{el} + k_{lat} + k_{bip}$, where k_{el}, k_{lat} and k_{bp} represent the electronic, lattice and bipolar contributions, respectively. The electronic contribution to the thermal conductivity, k_{el}, was calculated through the Wiedemann-Franz law $k_{el} = L\sigma T$, where L is the Lorentz constant (2 10^{-8} V^2K^{-2}), σ is the measured electrical conductivity and T is the absolute temperature. The bipolar contribution, k_{bp}, is due to the thermal excitation of charge carriers (i.e. holes for n-type semiconductors) opposite to the dominant ones (i.e. electrons for n-type semiconductors) above a critical temperature.[53]

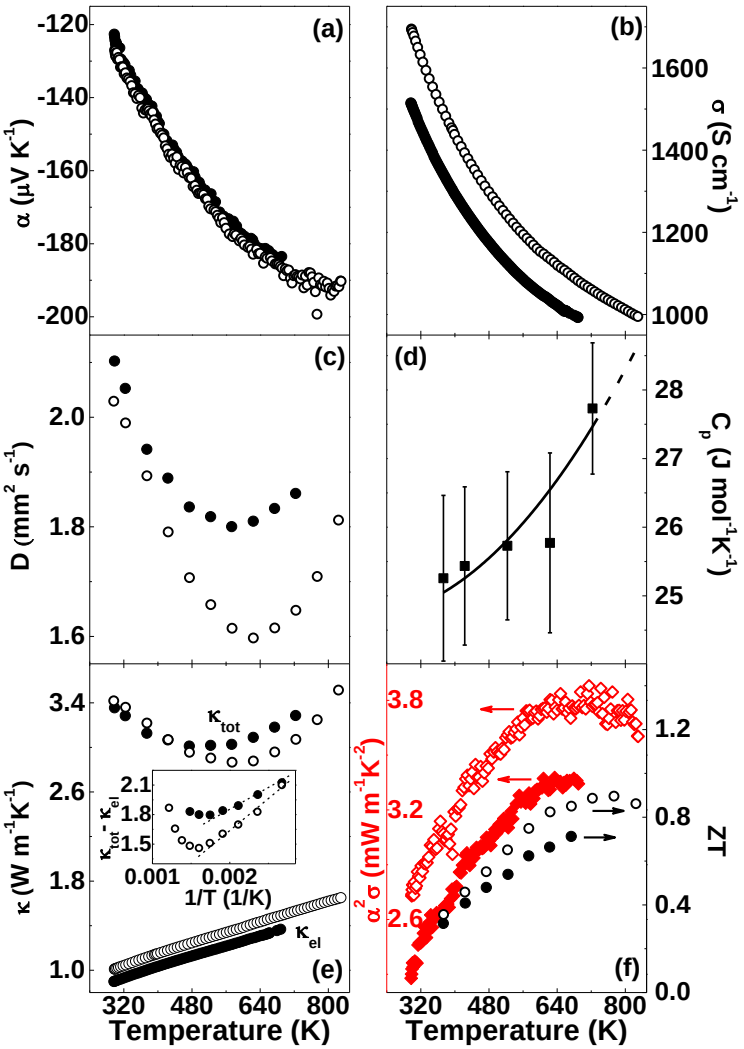

Figure III- 14: Thermoelectric and thermophysical properties of sintered ODP2 (open symbols) and ODP3 (filled symbols) samples as a function of temperature. (a) Seebeck coefficient, α. (b) Electrical conductivity, σ. (c) Thermal diffusivity, D. (d) Averaged experimental values of the specific heat, Cp, measured on ODP2 and ODP3 samples (black squares) with the corresponding fitting curve (continuous line); on the basis of the fitting result, specific heat is extrapolated in a larger temperature range (dashed line). (e) Thermal conductivity, k; k_{tot} and k_{el} represent the total and electronic thermal conductivities, respectively; the inset shows the difference between k_{tot} and k_{el} as a function of the inverse of temperature: the deviation from linearity at high temperature indicates the onset for bipolar conduction. (f) Left hand side (diamonds): power factor, $\alpha^2\sigma$. Right hand side (circles): figure of merit, ZT.

In order to separate the contributions of k_{lat} and k_{bp}, we plotted the difference between k and k_{el} as a function of 1/T, as shown in the inset of *Figure III- 14*e. The contribution of the bipolar thermal conductivity,[53] that is favoured at high temperature, becomes relevant when ($k - k_{el}$) vs. 1/T deviates from linearity (dotted lines are a guide to the eye). This behaviours explains the reason of the minimum in thermal conductivity, k, observed around 600 K. ODP2 shows lower values of ($k - k_{el}$) than ODP3, because of the larger amount of Yb hosted in the skutterudite structure, that leads to an increase of phonon scattering and, consequently, to a reduction of lattice thermal conductivity. The phonon scattering due to the larger Yb filling fraction compensates the increased electronic thermal conductivity caused by the larger density, leading to an overall lower thermal conductivity in ODP2 with respect to ODP3. Power factor was calculated from the measured values of the electrical conductivity and Seebeck coefficient as a function of temperature, as reported on the left hand side of *Figure III- 14*f (open and filled diamonds). The higher values shown by ODP2 with respect to ODP3 are due to the larger values of the electrical conductivity, related to higher density of the sample, since the two samples show the same values of the Seebeck coefficient. Finally, the figure of merit, ZT, as a function of temperature is reported on right hand side of *Figure III- 14*f (open and filled circles). ODP2 shows larger values of ZT with respect to ODP3 as a consequence of the larger power factor and the lower thermal

conductivity. In the case of ODP2, ZT reaches a maximum value of 0.9 at 773 K, in agreement with the values reported in Refs. [28,34] for similar values of Yb. *Figure III- 15* shows the thermoelectric properties (electrical conductivity, σ, Seebeck coefficient, α, lattice thermal conductivity, k_{tot} -k_{el}, and figure of merit, ZT) measured at 673 K as a function of the Yb content in Co_4Sb_{12}. The squares, diamond and triangles represent data from the literature (the reference is indicated by the corresponding number) while the stars are the data from this work.

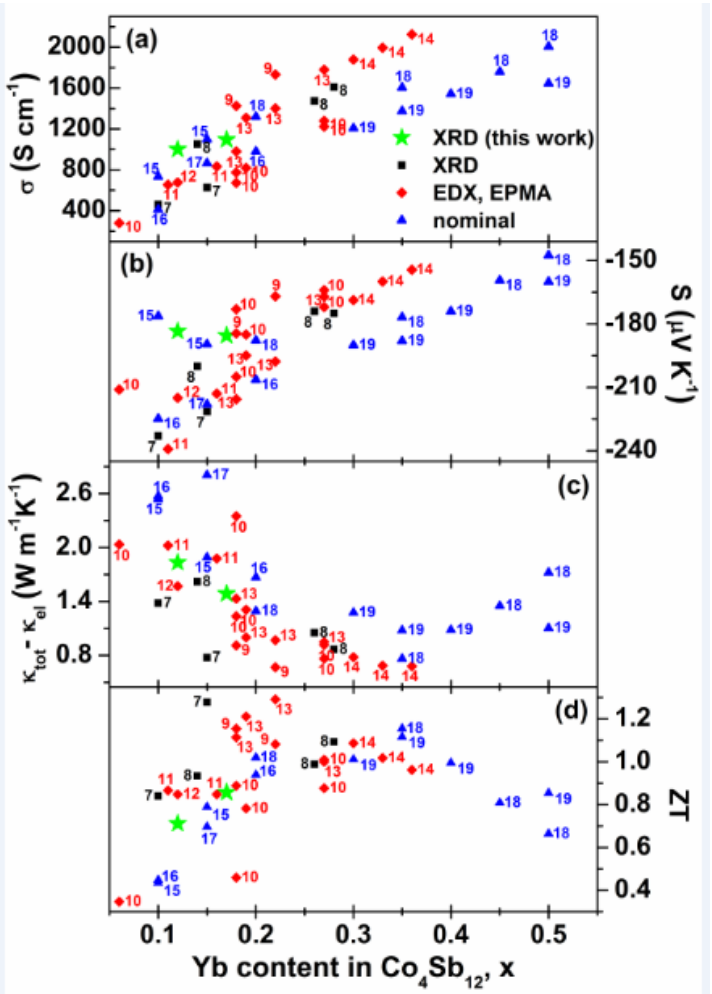

Figure III- 15: Thermoelectric properties at 673 K as a function of the Yb content in the Co_4Sb_{12} cell. (a) electrical conductivity, σ. (b) Seebeck coefficient, α. (c) lattice thermal conductivity, assessed as k_{tot}-k_{el}. (d) figure of merit, ZT. The squares, diamonds and triangles represent data literature (the numbers indicate the corresponding references), while the stars represent data from this work. The legend for the different symbols indicates the method how the actual Yb content was determined (XRD, EDS/EPMA, nominal composition).[41]

Data from the literature were grouped according to different symbols, depending on the technique used for determining the Yb content in the skutterudite phase. The data show some scattering likely due to presence of small amounts of secondary phases, different density of

the samples, difference between nominal and actual Yb content. As a general trend, when the Yb content increases, electrical conductivity, σ, increases, while the absolute value of the Seebeck coefficient, |α|, decreases, as show in *Figure III- 15*a and b, respectively. This trend is in agreement with the increased density of charge carrier due to the insertion of Yb atoms in the skutterudite cage[28,31,35]. The actual Yb content in Co_4Sb_{12}, measured by XRD and EDX/EPMA (squares and diamonds, respectively), never exceeds 0.35, setting this value as the solubility limit.[25,26] It was shown for $Fe_2Ni_2Sb_{12}$ (isoelectronic with Co_4Sb_{12}) that, as the Yb occupancy factor at 2a site in the skutterudite cage increases, the valence state of the Yb ion progressively decreases from trivalent to divalent, leading to the observed maximum solubility of the filler[21,23]. This solubility limit was recently exceeded by using non equilibrium processing such as ball milling[49]. Since the samples obtained in Ref. [46] contained relevant amounts of secondary phases, that considerably affects thermoelectric properties, they were not taken in account in the present discussion. Considering the triangles, representing the thermoelectric property as a function of the nominal Yb content, we observe that, when $x < 0.35$, they follow the same trend of the squares and diamonds, while, when $x > 0.35$, they are shifted to the right with respect to the squares and diamonds, representing the thermoelectric property as a function of the actual Yb content. When the solubility limit of Yb is exceeded, the $YbSb_2$ secondary phase forms[25,26] and its amount increases as the total Yb

content increases. Thus, for $x > 0.35$, the triangles represent multiphase materials rather than single phase materials, and show an increasing metallic behaviour (i.e. increasing electrical conductivity, σ, and decreasing Seebeck coefficient, $|\alpha|$) as the amount of secondary phase increases. The opposite effect of Yb filling on electrical conductivity and Seebeck coefficient leads to an optimized power factor, $\alpha^2\sigma$, for $0.2 < x < 0.3$ (not shown). The effect of the Yb solubility limit is even more evident when the lattice thermal conductivity, taken as the difference between k_{tot} and k_{el}, is considered, *Figure III- 15*c. In this case, the presence of a minimum of k_{tot} - k_{el} around $x \cong 0.35$ indicates that phonon scattering is maximized in correspondence of the Yb solubility limit and that further addition of Yb is counterproductive. Finally, the combined effect of power factor and thermal conductivity leads to an optimized value of the figure of merit, ZT, for $0.20 < x < 0.25$, as shown in *Figure III- 15*d.

3.5 Conclusions

In this work, we explored the effect of different processing routes on the structure, microstructure and thermoelectric properties of Yb-doped $CoSb_3$ compound. Free cooling of the melt leads to the formation of a porous bulk with coarse microstructure. Rapid solidification by planar flow casting allows the formation of

fragmented ribbons with a refined microstructure and no porosity. In both cases, as prepared samples show multiple phases, thus annealing was needed to promote homogenization. The solubilisation of Yb in the skutterudite structure is significantly faster for the rapidly solidified ribbons as a consequence of the increased grain boundary diffusivity with respect to the bulk sample due to the finer microstructure of the ribbons. Thus, rapid solidification reveals to be a convenient intermediate step to decrease the total processing time for the synthesis of filled skutterudites.

Sintering of the powders by ESF from annealed bulk and ribbons did not allow to obtain a dense and single phase sample because of difficult temperature control of the technique.

Powders obtained by grinding the bulk show a narrower particle size distribution with respect to the powders obtained from the ribbons, leading to a lower density in the sintered samples. Sintering of the powders by ODP obtained from as quenched and annealed ribbons leads to almost single phase dense samples, however Yb filling is higher when annealed ribbons are used. Thermoelectric properties of the sintered samples depend on porosity and Yb filling. As expected, larger values of electrical conductivity were found in denser samples. Concerning thermal conductivity, the interplay between density and Yb filling is more complex. On the one hand, less dense samples are expected to show lower values of thermal conductivity. On the other hand, denser samples show a larger Yb filling that leads to a lower

lattice thermal diffusivity and, overall, to a lower thermal conductivity with respect to less dense samples. A survey of literature data shows a direct correlation between thermoelectric properties and Yb content when the latter is below the solubility limit. When the Yb content exceeds the solubility limit, thermoelectric properties show a deviation from the observed trend due to the presence of secondary phases affecting thermoelectric behaviour.

Reference

1. Breithaupt, A. Ueber eine neue Kies-Spezies von Skutterud. *Ann. Phys.* (1827). doi:10.1002/andp.18270850110

2. Oftedal, I. XXXIII. Die Kristallstruktur von Skutterudit und Speiskobalt-Chloanthit. *Zeitschrift für Krist. - Cryst. Mater.* (2014). doi:10.1524/zkri.1928.66.1.517

3. Jeitschko, W. & Braun, D. LaFe 4 P 12 with filled CoAs 3 -type structure and isotypic lanthanoid–transition metal polyphosphides . *Acta Crystallogr. Sect. B Struct. Crystallogr. Cryst. Chem.* (1977). doi:10.1107/s056774087701108x

4. Wee, D., Kozinsky, B., Marzari, N. & Fornari, M. Effects of filling in CoSb3: Local structure, band gap, and phonons from first principles. *Phys. Rev. B - Condens. Matter Mater. Phys.* (2010). doi:10.1103/PhysRevB.81.045204

5. Sales, B., Mandrus, D., Chakoumakos, B., Keppens, V. & Thompson, J. Filled skutterudite antimonides: Electron crystals and phonon glasses. *Phys. Rev. B - Condens. Matter Mater. Phys.* (1997). doi:10.1103/PhysRevB.56.15081

6. Sales, B. C., Mandrus, D. & Williams, R. K. Filled skutterudite antimonides: A new class of thermoelectric materials. *Science (80-.).* (1996). doi:10.1126/science.272.5266.1325

7. Nolas, G. S., Kaeser, M., Littleton IV, R. T. & Tritt, T. M. High figure of merit in partially filled ytterbium skutterudite materials. *Appl. Phys. Lett.* **77**, 1855–1857 (2000).

8. Pei, Y. Z. *et al.* Synthesis and thermoelectric properties of KyCo 4Sb12. *Appl. Phys. Lett.* (2006). doi:10.1063/1.2397538

9. Chen, L. D. *et al.* Anomalous barium filling fraction and n-type thermoelectric performance of BayCo4Sb12. *J. Appl. Phys.* **90**, 1864–1868 (2001).

10. Puyet, M. *et al.* High temperature transport properties of partially filled Ca xCo4Sb12 skutterudites. *J. Appl. Phys.* (2004). doi:10.1063/1.1688463

11. Sales, B., Chakoumakos, B. & Mandrus, D. Thermoelectric properties of thallium-filled skutterudites. *Phys. Rev. B - Condens. Matter Mater. Phys.* (2000). doi:10.1103/PhysRevB.61.2475

12. He, T., Chen, J., Rosenfeld, H. D. & Subramanian, M. A. Thermoelectric properties of indium-filled skutterudites. *Chem. Mater.* (2006). doi:10.1021/cm052055b

13. Takizawa, H., Miura, K., Ito, M., Suzuki, T. & Endo, T. Atom insertion into the CoSb3 skutterudite host lattice under high pressure. *J. Alloys Compd.* (1999). doi:10.1016/S0925-8388(98)00802-0

14. Uher, C. Chapter 5 Skutterudites: Prospective novel thermoelectrics. *Semicond. Semimetals* (2001). doi:10.1016/S0080-8784(01)80151-4

15. Morelli, D. T. *et al.* Low-temperature transport properties of p-type CoSb3. *Phys. Rev. B* (1995). doi:10.1103/PhysRevB.51.9622

16. Caillat, T., Borshchevsky, A. & Fleurial, J. P. Properties of single crystalline semiconducting CoSb3. *J. Appl. Phys.* (1996). doi:10.1063/1.363405

17. Caillat, T., Borshchevsky, A. & Fleurial, J.-P. Preparation and thermoelectric properties of p- and n-type CoSb3. in (2008). doi:10.1063/1.46835

18. Chen, L. D. *et al.* Anomalous barium filling fraction and n-type thermoelectric performance of BayCo4Sb12. *J. Appl. Phys.* (2001). doi:10.1063/1.1388162

19. Rowe, D. M. Thermoelectrics handbook: macro to nano. *Thermoelectr. Handb. Macro to Nano* (2005). doi:10.1038/ki.2011.318

20. Bourgoin, B. *et al.* Preparation and thermopower of new mischmetal-based partially filled skutterudites MmyFe4-x(Co/Ni)xSb12. *J. Alloys Compd.* (2005). doi:10.1016/j.jallcom.2005.03.032

21. Bérardan, D., Alleno, E., Godart, C., Rouleau, O. & Rodriguez-Carvajal, J. Preparation and chemical properties of the skutterudites (Ce-Yb) yFe4-x(Co/Ni)xSb12. *Mater. Res. Bull.* **40**, 537–551 (2005).

22. Artini, C. *et al.* Correlations between Structural and Electronic Properties in the Filled Skutterudite Smy(FexNi1-x)4Sb12. *Inorg. Chem.* **55**, 2574–2583 (2016).

23. Kaltzoglou, A., Vaqueiro, P., Knight, K. S. & Powell, A. V. Synthesis, characterization and physical properties of the skutterudites YbxFe2Ni2Sb12 (0≤x≤0.4). *J. Solid State Chem.* **193**, 36–41 (2012).

24. Shi, X. *et al.* Low thermal conductivity and high thermoelectric figure of merit in n -type Bax Yby Co4 Sb12 double-filled skutterudites. *Appl. Phys. Lett.* **92**, 2–4 (2008).

25. Wang, S. *et al.* High-performance n-type YbxCo4Sb12: From partially filled skutterudites towards composite thermoelectrics. *NPG Asia Mater.* (2016). doi:10.1038/am.2016.77

26. Tang, Y., Chen, S. wen & Snyder, G. J. Temperature dependent solubility of Yb in Yb–CoSb3 skutterudite and its effect on preparation, optimization and lifetime of thermoelectrics. *J. Mater.* **1**, 75–84 (2015).

27. Liu, H., Zhao, X., Zhu, T. & Gu, Y. Thermoelectric properties of YbxCo4Sb12 system. *J. Rare Earths* (2012). doi:10.1016/S1002-0721(12)60072-6

28. Park, K. H., Seo, W. S., Shin, D. K. & Kim, I. H. Thermoelectric properties of Yb-filled CoSb3 skutterudites. *J. Korean Phys. Soc.* (2014). doi:10.3938/jkps.65.491

29. Geng, H. Y., Ochi, S. & Guo, J. Q. Solidification contraction-free synthesis for the Yb0.15 Co4 Sb12 bulk material. *Appl. Phys. Lett.* (2007). doi:10.1063/1.2755926

30. Dahal, T. *et al.* Thermoelectric property enhancement in Yb-doped n-type skutterudites YbxCo4Sb12. *Acta Mater.* **75**, 316–321 (2014).

31. Yang, J. *et al.* Solubility study of Yb in n -type skutterudites Ybx Co4 Sb12 and their enhanced thermoelectric properties. *Phys. Rev. B - Condens. Matter Mater. Phys.* **80**, 1–5 (2009).

32. Zhao, X. Y. *et al.* Synthesis of YbyCo4Sb12/Yb2O3composites and their thermoelectric properties. *Appl. Phys. Lett.* **89**, 10–13 (2006).

33. Yao, Z., Li, X. Y., Tang, Y. S. & Chen, L. D. Genomic Effects of the Quenching Process on the Microstructure and Thermoelectric Properties of Yb0.3Co4Sb12. *J. Electron. Mater.* (2015). doi:10.1007/s11664-014-3582-7

34. Li, H., Tang, X., Su, X., Zhang, Q. & Uher, C. Nanostructured bulk YbxCo4Sb12 with high thermoelectric performance prepared by the rapid solidification method. *J. Phys. D. Appl. Phys.* **42**, (2009).

35. Salvador, J. R. *et al.* Transport and mechanical properties of Yb-filled skutterudites. *Philos. Mag.* **89**, 1517–1534 (2009).

36. Hiroaki Okamoto, Mark E. Schlesinger, E. M. M. *Handbook: Alloy Phase Diagrams*. (ASM International, 2016).

37. Alinejad, B., Castellero, A. & Baricco, M. Full dense CoSb3 single phase with high thermoelectric performance prepared by oscillated cooling method. *Scr. Mater.* (2016). doi:10.1016/j.scriptamat.2015.10.029

38. Artini, C., Castellero, A., Baricco, M., Buscaglia, M. T. & Carlini, R. Structure, microstructure and microhardness of rapidly solidified Smy(FexNi1-x)4Sb12 (x = 0.45, 0.50, 0.70, 1) thermoelectric compounds. *Solid State Sci.* (2018). doi:10.1016/j.solidstatesciences.2018.03.012

39. Baricco, M. *et al.* Thermal stability and hardness of Mg-Cu-Au-Y amorphous alloys. *J. Alloys Compd.* (2007). doi:10.1016/j.jallcom.2006.08.110

40. Bux, S. K., Fleurial, J. P. & Kaner, R. B. Nanostructured materials for thermoelectric applications. *Chemical Communications* (2010). doi:10.1039/c0cc02627a

41. Aversano, F. *et al.* Effect of rapid solidification on the synthesis and thermoelectric properties of Yb-filled Co4Sb12 skutterudite. *J. Alloys Compd.* (2019). doi:10.1016/j.jallcom.2019.04.337

42. Fais, A., Actis Grande, M. & Forno, I. Influence of processing parameters on the mechanical properties of Electro-Sinter-Forged iron based powders. *Mater. Des.* (2016). doi:10.1016/j.matdes.2015.12.142

43. Ceresara, S., Fanciulli, C., Passaretti, F. & Vasilevskiy, D. Texturing of (Bi0.2Sb0.8)2Te3 nanopowders by open die pressing. *J. Electron. Mater.* **42**, 1529–1534 (2013).

44. Lutterotti, L., S. Matthies, and H. R. W. MAUD: a friendly Java program for material analysis using diffraction. *IUCr Newsl. CPD* **21**, 14–15 (1999).

45. Boldrini, S. *et al.* Test rig for high-temperature thermopower and electrical conductivity measurements. *J. Electron. Mater.* (2013). doi:10.1007/s11664-012-2437-3

46. Xiong, Z., Chen, X., Huang, X., Bai, S. & Chen, L. High thermoelectric performance of Yb0.26Co4Sb 12/yGaSb nanocomposites originating from scattering electrons of low energy. *Acta Mater.* **58**, 3995–4002 (2010).

47. Porter, D. A., Easterling, K. E. & Sherif, M. Y. *Phase transformations in metals and alloys, third edition*. *Phase Transformations in Metals and Alloys, Third Edition* (2009). doi:10.1201/9781439883570

48. Feng, B., Xie, J., Cao, G., Zhu, T. & Zhao, X. Enhanced thermoelectric properties of p-type CoSb3/graphene nanocomposite. *J. Mater. Chem. A* (2013). doi:10.1039/c3ta13202a

49. Ryll, B. *et al.* Structure, Phase Composition, and Thermoelectric Properties of Yb x Co 4 Sb 12 and Their Dependence on Synthesis Method. *ACS Appl. Energy Mater.* (2018). doi:10.1021/acsaem.7b00015

50. Bruggeman, D. A. G. “Calculation of various physical constants of heterogeneous substances, part I: Dielectric constants and conductivities of mixtures of isotropic substances. *Ann. Phys.* (1935). doi:10.1002/andp.19374210205

51. Koelman, J. M. V. A. & De Kuijper, A. An effective medium model for the electric conductivity of an N-component anisotropic and percolating mixture. *Phys. A Stat. Mech. its Appl.* (1997). doi:10.1016/S0378-4371(97)00385-3

52. Dinsdale, A. T. SGTE data for pure elements. *Calphad* (1991). doi:10.1016/0364-5916(91)90030-N

53. Wang, S. *et al.* Conductivity-limiting bipolar thermal conductivity in semiconductors. *Sci. Rep.* (2015). doi:10.1038/srep10136

CHAPTER IV:

SYNTHESIS AND PROPERTIES OF THERMOELECTRIC TiNiSn COMPOUNDS

4.1 Introduction

Heusler compounds were first synthesized in 1903 by Friedrich Heusler who discovered $MnCu_2Al$ was ferromagnetic despite containing no magnetic elements. This led to the discovery of multiple large structural classes of materials, including half-Heusler *(hH)* and Heusler *(H)* compounds. Compounds with these structures exhibit properties with a broad range of applications including magnetic tunnel junctions,[1] topological insulators,[2] superconductivity,[3] magnetocalorics,[4] and thermoelectrics.[5] Half-Heusler compounds are a group of ternary intermetallic compounds with the general formula ABX, where A is a more electropositive transition metal, B is a less electropositive transition metal and X is the main group element,[6] so an huge number of hH materials can be formed by combination of the different elements maintaining the VEC equal to 18, as shown in Figure IV- 1.

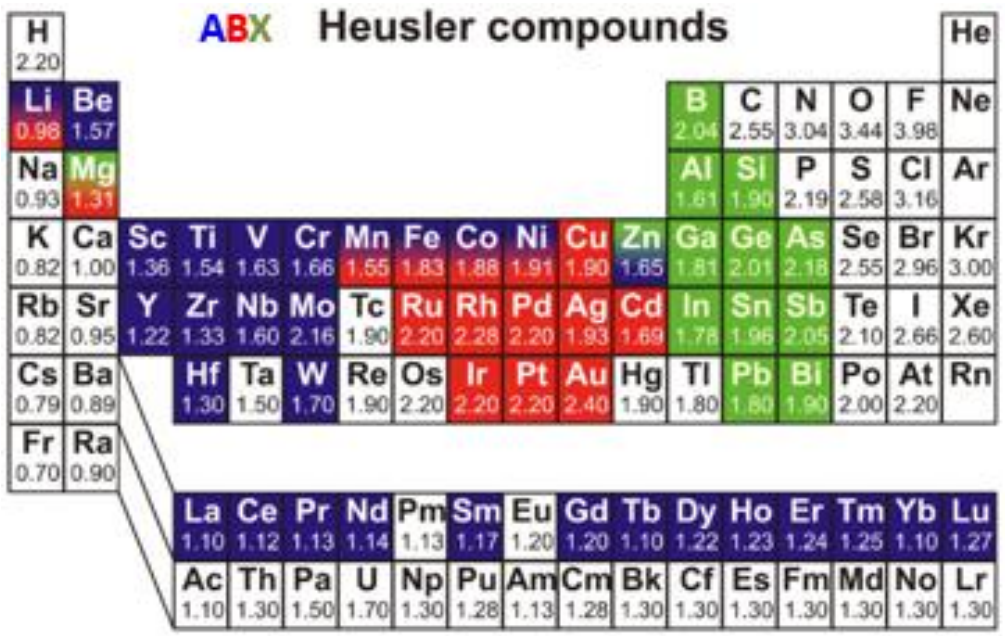

Figure IV- 1: Periodic table of the elements. The huge number of hH materials can be formed by combination of the different elements according to the color scheme and maintaining the VEC equal to 18.[7]

The crystal structure consists in three interpenetrating face-centered-cubic (fcc) sublattices and one vacant fcc sublattice, if the vacant sublattice is also filled by transition metal B, the corresponding Heusler structure is obtained, as shown in Figure IV- 2.

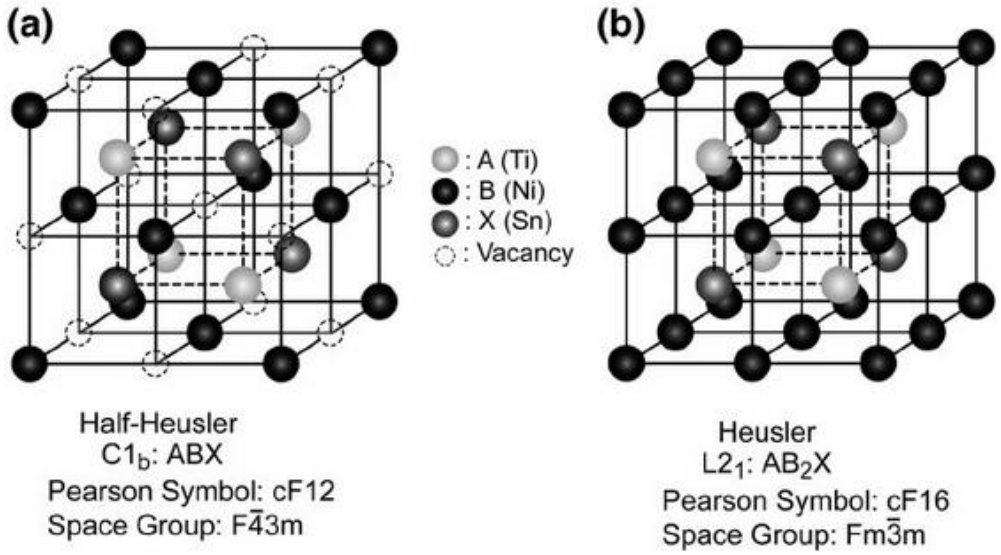

Figure IV- 2: Unit cells of the ordered crystal structure (a) half-Heusler type and (b) Heusler type.[8]

4.2 State of art and aim of work

Half-Heusler compounds with 18 valence electrons have been extensively studied as potential thermoelectric materials for medium/high temperature power generation.[9–15] Among the different family of half-Heusler is well known that the MNiSn (M = Ti, Zr, Hf) based half-Heusler show the best thermoelectric performance.[16–30] ZT of half-Heusler compounds can be improved by reducing the lattice thermal conductivity, thus several methods were investigated for increasing phonon scattering through mass fluctuation,[31] phase separation[24,25,32] and microstructure refinement.[19,22,29,30] Seebeck coefficient and electrical conductivity of TiNiSn alloys prepared with different processing routes are quite scattered due to residual secondary phases.[23,27] For example, processing from the melt (arc

melting, induction melting) leads to the formation of sample with multiple phases that need long annealing to be homogenized.[18] Our approach was to study the effect two different pre-processing routes (arc melting and rapid solidification) on the structure and microstructure of TiNiSn alloy. Subsequently, arc melted ingots and rapidly solidified flakes were post-processed by annealing and powder sintering, respectively, in order to obtain homogeneous and dense massive samples for thermoelectric characterization. The effect of residual secondary phases on the measured values of Seebeck coefficient and electrical conductivity is discussed through a literature survey. The role of grain boundary scattering on the lattice thermal conductivity was evaluated. Finally, in order to study the thermal stability of TiNiSn alloy, the effect of thermal cycles on the thermoelectric properties were evaluated. Part of the results of this chapter was published in Ref.[33].

4.3 Experimental

Polycrystalline samples, TiNiSn, were synthesized by arc-melting of elemental metals (Titanium 99.99%; Nickel 99.95%; Tin 99.995%) in Argon (5.5) atmosphere. Residual traces of oxygen were removed by melting Ti and Zr getters. The ingots were flipped over and remelted five times to ensure chemical homogeneity. On the one side, the arc-melted ingot, wrapped in a Ta foil and sealed under vacuum in a quartz tube, was annealed for three weeks at 1123 K and then one week at 923 K in order to obtain a single phase sample. On the other side, arc-

melted ingots were rapidly solidified by planar flow casting (Edmund Bühler GmbH), producing fragmented ribbons. The alloy was induction melted in a boron nitride (BN) crucible under Argon (5.5) atmosphere (1 bar) and injected onto a rotating copper wheel at different wheel speed (10, 20 and 30 ms^{-1}) by an Ar overpressure of 0.2 bar with a distance between the crucible nozzle and the wheel of 0.3 mm. The rapidly solidified ribbons were ground by hand in an agate mortar, and the powders were sintered by Open Die Pressing (ODP).[34] The powders were loaded into a Fe sheath and preheated at 973 K and sintered at 748 K for 15 min applying a compressive load of 20 tons. For sake of clarity the arc-melted, arc-melted and annealed, rapidly solidified and as sintered samples will be named AM, AM-AN, RS and ODP-AP, respectively. Structural characterization was performed by X-ray diffraction (XRD) using both Bragg Brentano (Panalytical X'Pert Pro) and parallel beam (Panalytical PW3020) geometries with Cu Kα radiation (Kα = 1.5406 Å). Rietveld refinement of the measured diffraction patterns was performed using Maud software. XRD measurements were carried out on ground powders in order to remove possible effects of preferential crystallographic orientations. Microstructural observations were performed by scanning electron microscopy (SEM) using a ZEISS EVO 50 XVP-LaB6 equipped with an Oxford Instruments INCA - Energy 250 for energy-dispersive X-ray analysis (EDX). Chemical etching was carried out maintaining the samples into Kroll's reagent

(92 % distilled water, 6 % Nitric acid and 2 % Hydrofluoric acid) for about 20 seconds. Thermodynamic calculations were performed by Pandat software using the database optimized by Gürth et al.[20] Thermal stability of the AM-AN sample was evaluated by thermogravimetry analysis, TGA (TA-Q600). Seebeck coefficient, α, and electrical conductivity σ, were measured under He flow in the temperature range from room temperature to 1008 K by using a custom test apparatus described in chapter 3.[35] The relative error of α and σ was estimated to around 4 and 5 % respectively. The thermal conductivity k was calculated from $k = D\rho C_p$ where ρ is the sample density, D is the thermal diffusivity and C_p is the heat capacity. The thermal diffusivity was measured by laser flash method (LFA 457 MicroFlash, Netzesch, Selb, Germany) with uncertainty around 3 %. The mass density (ρ) was estimated, with a relative error of 5 %, both by Archimedian principle with a pycnometer, and using the ratio between the mass and the volume of regularly shaped samples. The heat capacity C_p was determined using Differential Scanning Calorimetry (DSC). In the DSC measurements of the specific heat, heating ramps 10 K min^{-1} were performed in limited temperature ranges of 30 K. Each ramp was preceded and followed by a long isotherm in order to stabilize the signal. The measurement was repeated with the empty alumina pan, a standard (sapphire) and the sample. The specific heat of the sample at different temperature was

obtained by comparing the signals measured for the sample and the standard using both the “height” and the “area” methods.

4.4 Results

4.4.1 Effect of pre-processing on phase formation and microstructure

Figure IV- 3 shows the XRD pattern of the AM ingot and RS (20 ms^{-1}) ribbons. The AM ingot, Figure IV- 3a, shows the presence of TiNiSn half Heusler phase together with $TiNi_2Sn$ full Heusler, Ti_6Sn_5 and Sn phases. The relative amount of the phases and the corresponding lattice parameters obtained by Rietveld refinement are reported in Table IV- 1.

Table IV- 1
Results of the Rietveld refinement of the XRD patterns in Figure IV- 3 and in Figure IV- 7: fitted phases, relative quantity of the phases, lattice parameter, a, of the phases.

Sample	Density (gcm^{-3})	Phases	Relative amount (wt. %)	Lattice parameter (Å)
AM	–	TiNiSn	62	5.949(1)
		$TiNi_2Sn$	26	6.075(2)
		Ti_6Sn_5	9	…
		Sn	3	…
RS (20 m/s)	–	TiNiSn	85	5.950(6)
		$TiNi_2Sn$	11	6.061(3)
		Sn	4	…
AM_AN	6.78	TiNiSn	98	5.928(4)
		$TiNi_2Sn$	2	6.103(7)
ODP	6.82	TiNiSn_1	58	5.926(8)
		TiNiSn_2	36	5.943(4)
		Ni_3Sn_4	6	…

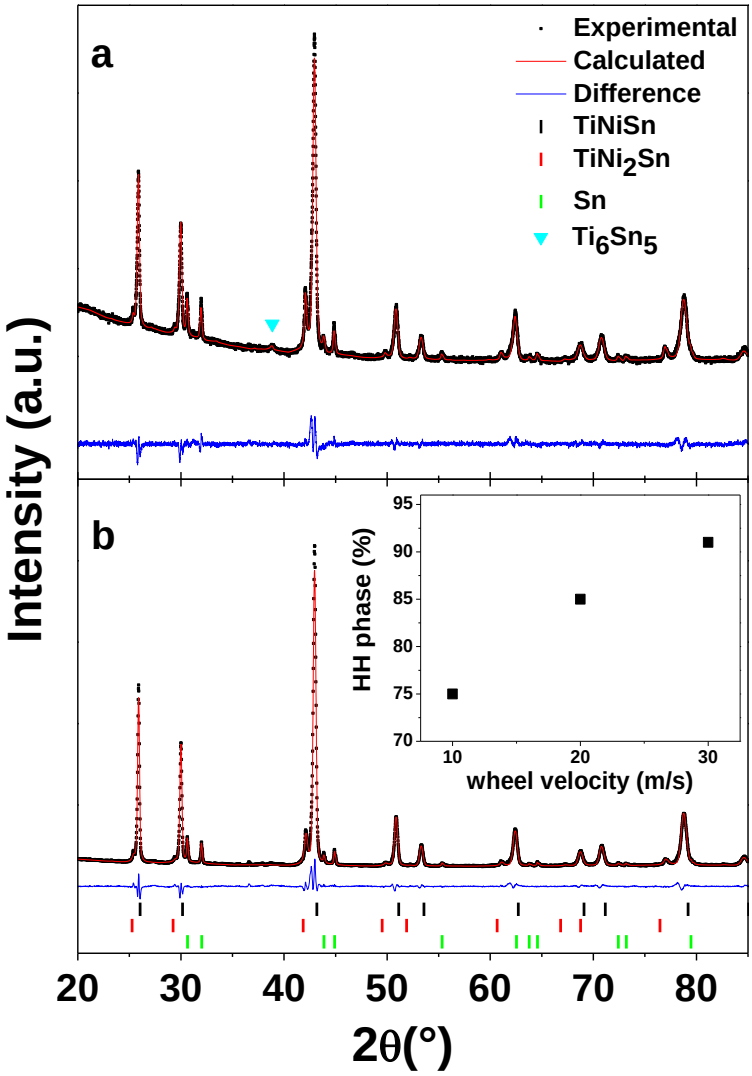

Figure IV- 3: X-ray diffraction patterns of the as prepared arc melted master alloy (a) and the rapidly solidified ribbon (20 ms^{-1}) (b). inset in (b) shows the relative amount of TiNiSn half-Heusler phase, performed by Rietveld refinement of the patterns of the ribbon rapidly solidified at different wheel velocity, as a function of the wheel speed.

Figure IV- 4a shows the backscattered electron image of the AM ingot. The phases identified are half Heusler TiNiSn (1), full Heusler $TiNi_2Sn$ (2), Ti_6Sn_5 (3), Ni_3Sn_4 (4), Ti_5Sn_3 (5), Ti (6) and Sn (7). Only

the amount of the phases identified by XRD were quantified because the other phases were below the detection limit. The presence of more than three phases in the AM sample indicates that the thermodynamic equilibrium was not reached, as a consequence of the complex solidification path involving a peritectic reaction[20] that is hindered by long distance diffusion.

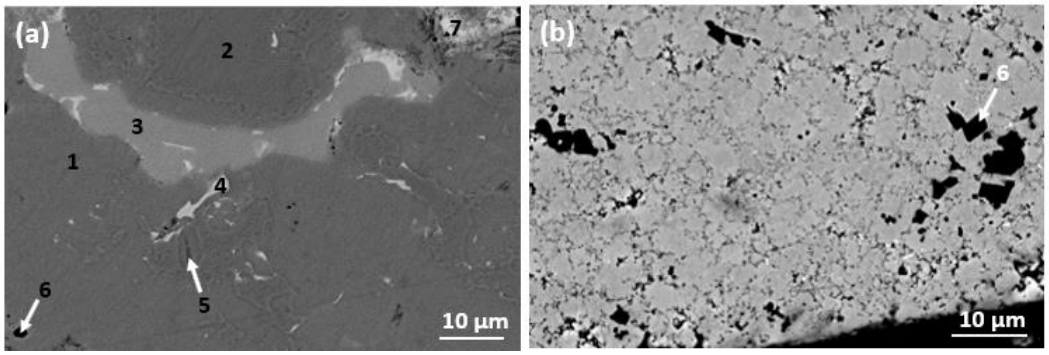

Figure IV- 4: Scanning electron microscope micrograph (backscattered electrons detector) of the as prepared arc melted master alloy (a) and the rapidly solidified ribbon ($20ms^{-1}$) (b). the phases are labelled in the following way: TiNiSn (1), full Heusler $TiNi_2Sn$ (2), Ti_6Sn_5 (3), Ni_3Sn_4 (4), Ti_5Sn_3 (5), Ti (6) and Sn (7).

The relative amount of the phases forming upon solidification was calculated using the Pandat software and the database optimized by Gürth et al.[20], on the basis of the Scheil model that assumes complete miscibility in the liquid state and absence of diffusion in solid state. On the one hand, all the phases predicted by the Scheil model were experimentally observed by SEM in the AM ingot, Figure IV- 4a, a part from Ti_2Sn_3 that is expected to be the less abundant (< 2 wt.%). On the other hand, the presence of elemental Ti, detected by SEM, Figure IV- 4a, is not foresee by the Scheil model and can be explained

by uncompleted melting during the process. In Figure IV- 5 the relative amounts of the phases calculated at the end of the solidification process are compared with the corresponding amounts obtained by the quantitative analysis of the XRD patterns.

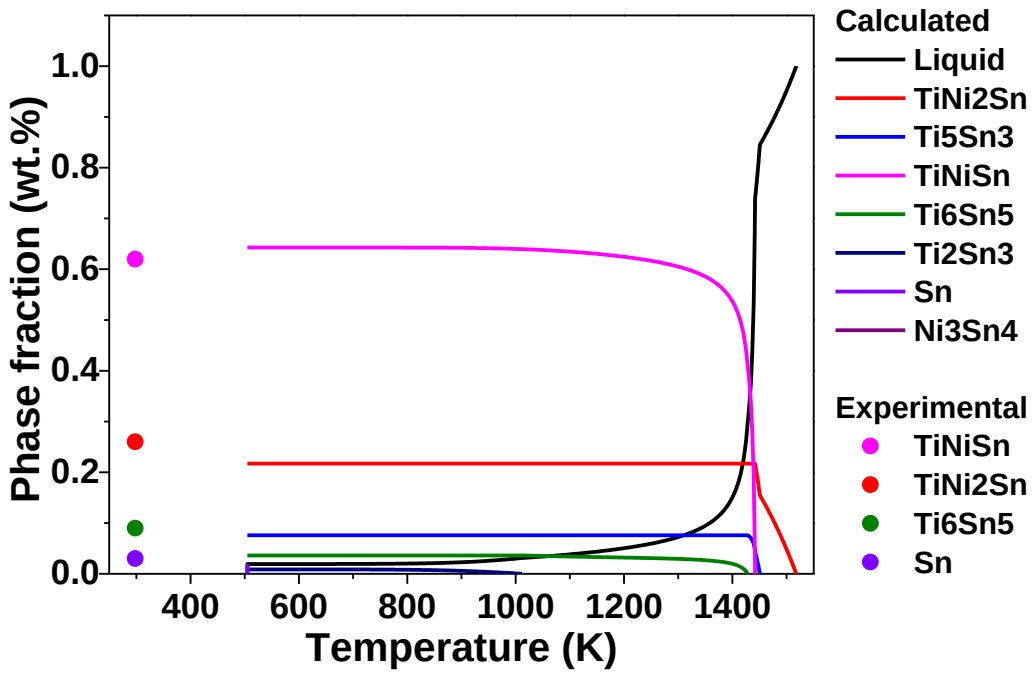

Figure IV- 5: Relative amount of the phases as a function of the temperature calculated with the Scheil model (lines) and experimentally determined by quantitative analysis of the XRD pattern (symbols).

Despite the minority could not be quantified by Rietveld analysis of the XRD patterns, because below the detection limit, the agreement between the calculated and experimental values for the remaining four phases (TiNiSn, $TiNi_2Sn$, Ti_6Sn_5, Sn) is rather good, validating the choice of the Scheil model for describing the solidification of the AM sample

The XRD pattern of the RS ($20ms^{-1}$) sample, Figure IV- 3b, shows the peaks of TiNiSn phase, together with the less intense peaks related to $TiNi_2Sn$ and Sn. The relative amount of the phases and the corresponding lattice parameters are reported in Table IV- 1. The amount of the half Heusler phase in the RS sample increases as the wheel speed increases, as shown by the inset of Figure IV- 3b, and is always larger than in the AM sample. The SEM micrograph of Figure IV- 4b shows the presence of elemental Ti that counterbalance the apparent excess in Ni and Sn estimated by the quantitative analysis of the XRD patterns. The presence of elemental Ti is not expected from the thermodynamic equilibrium[20] and can be explained by the short processing time in the molten state that does not allow to dissolve unreacted Ti already present in the starting ingot, Figure IV- 4a. Figure IV- 6 shows a magnification of the calculated stable and metastable isopleths Ni-SnTi obtained by maintaining and suspending the $TiNi_2Sn$ phase, respectively. The comparison between the two isopleths shows that an undercooling of the liquid of about 70 K is necessary to avoid the primary solidification of $TiNi_2Sn$ phase. Such a degree of undercooling can be typically reached by rapid solidification hindering the formation of the primary phase $TiNi_2Sn$ and allowing the solidification of the metastable liquid directly in the desired TiNiSn phase. Another effect of the liquid undercooling associated to the rapid solidification process is the microstructure refinement (grain size between 0.5 µm and 5 µm), as shown by the

SEM micrograph of the etched cross section of the ribbon, Figure IV- 4b.

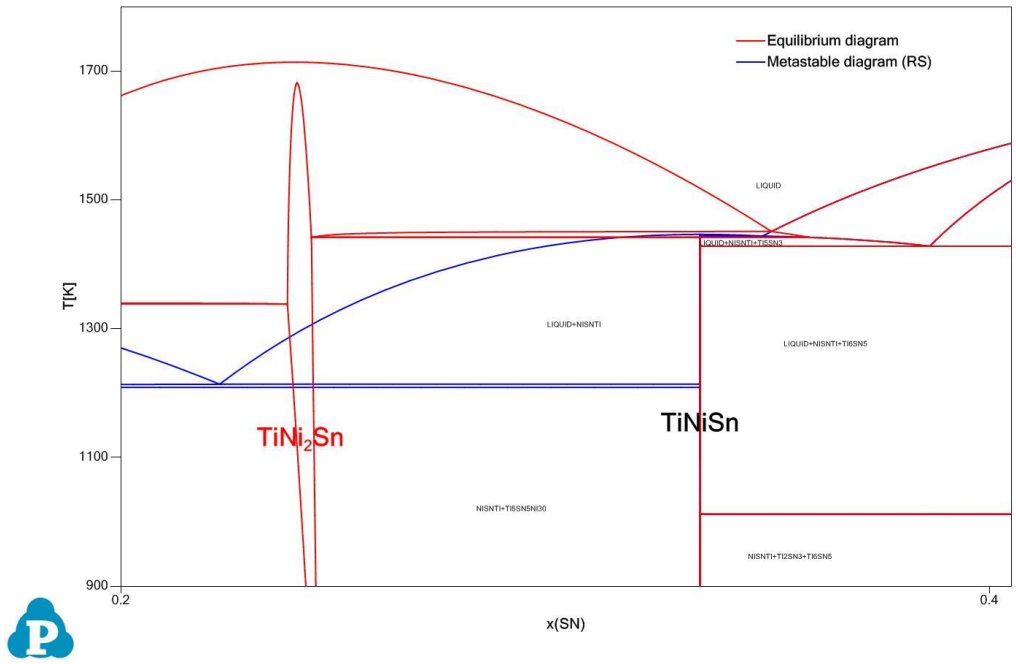

Figure IV- 6: Calculated isopleths Ni-SnTi obtained by maintaining (red line) and suspending (blue line) the $TiNi_2Sn$ phase

In both AM and RS samples the value of refined lattice parameters of TiNiSn and $TiNi_2Sn$ significantly deviate from the reference values 5.921 Å for TiNiSn and 6.098 Å for $TiNi_2Sn$. Thus, uncontrolled solidification leads to the formation of non-stoichiometric compounds, with a larger amount of Ni in the TiNiSn cell and a lower amount of Ni in the $TiNi_2Sn$ cell, in agreement with the solvus lines in the isopleth Ni-TiSn.[36] The amount of Ni present in the half and full Heusler phases in AM and RS samples is very close to the solubility

limit around 1223 K[20], indicating that the high temperature solute content was frozen during cooling.

4.4.2 Post-processing

The XRD pattern of the AM-AN sample, Figure IV- 7a, shows only the reflections of the TiNiSn and $TiNi_2Sn$ phases, while the backscattered electron SEM image, Figure IV- 8a, shows traces of Ni_3Sn_4 that could not be detected by XRD because below the detection limit.

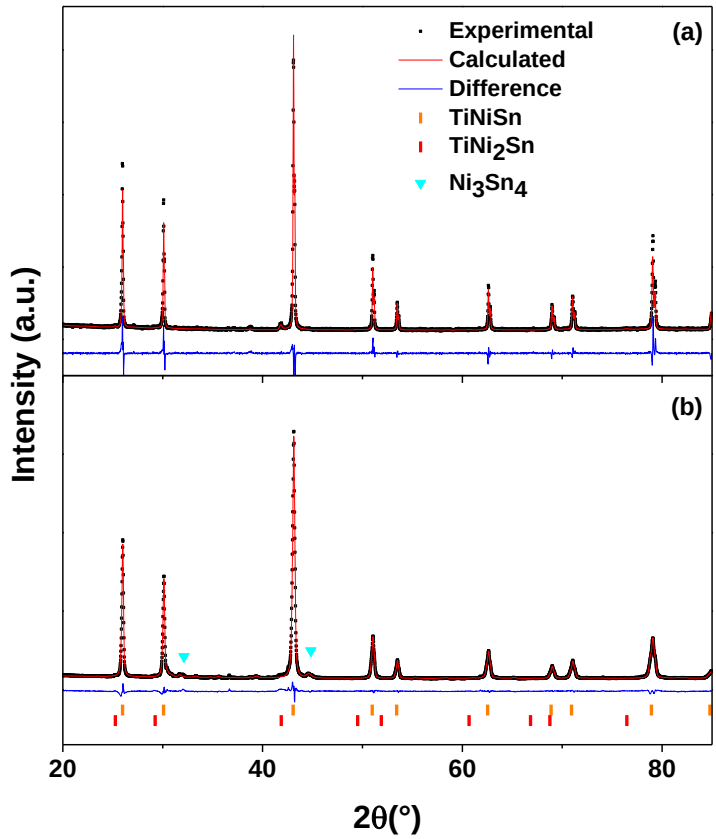

Figure IV- 7: X-ray diffraction patterns of the arc melted and annealed master alloy (AM-AN), (a), and the ODP sample obtained by sintering the rapidly solidified flakes, (b).

As a consequence of the long annealing, AM-AN sample attains equilibrium in a three phases region (TiNiSn, $TiNi_2Sn$, Ni_3Sn_4) and the lattice parameters of both TiNiSn and $TiNi_2Sn$ tend to the equilibrium values, as reported in Table IV- 1. The deviation from the single phase region can be explained by a slight deviation of the sample composition from the nominal stoichiometry that could not be detected by EDX analysis. The XRD pattern of ODP-AP sample, Figure IV- 7b, shows the peaks of the TiNiSn phase and Ni_3Sn_4

secondary phase. Furthermore, the sample after sintering (ODP-AP) shows asymmetry and strain broadening of the peaks related to half Heusler phase. This behaviour was also observed for example in hot pressed TiNiSn samples and was explained by inhomogeneous distribution of interstitial metals in the Wyckoff position 4d in the cell [28]. We modelled the peak broadening using two half-Heusler phases (TiNiSn_1 and TiNiSn_2): the corresponding refined lattice parameters and relative amounts are reported in Table IV- 1.

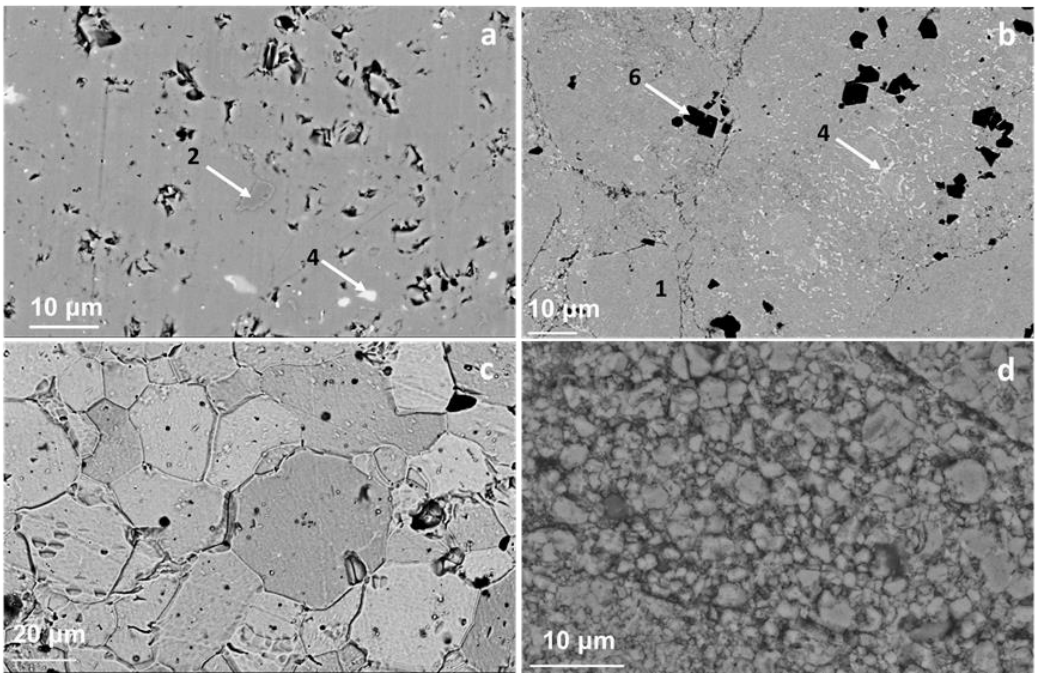

Figure IV- 8: Backscattered electron SEM images of the arc melted and annealed master alloy (AM-AN), (a), and the ODP sample obtained by sintering the rapidly solidified flakes, (b). The legend of the phases indicated by the arrows is the same as in Figure IV- 4. Secondary electron SEM images of the etched AM-AN, (c), and ODP, (d), samples.

The phase TiNiSn_1 has a lattice parameter close to the equilibrium value, indicating that excess Ni was rejected during ODP, whereas the

phase TiNiSn_2 shows a lattice parameter comparable to the one of the RS sample, indicating that the interstitial Ni originally present is maintained during ODP. The backscattered electron image of the ODP-AP sample, Figure IV- 8c, still shows the presence of unreacted Ti that was already detected in the RS ribbon. The secondary electron images reported in Figure IV- 8b and d show the AM-AN and ODP-AP samples after chemical etching, respectively. The ODP-AP sample, Figure IV- 8d, shows a finer microstructure (0.5-5 μm) than AM-AN sample (20-60 μm), Figure IV- 8b, and is comparable to the one of the RS sample, Figure IV- 4b. The grain growth in the ODP-AP sample was limited using sintering conditions in proximity or below the recrystallization temperature (~ 825 K), since the sample was pre-annealed at 993 K for only 5 min and pressed at 748 K for 15 min.

4.4.3 Thermoelectric properties

- **Seebeck coefficient and electrical conductivity**

Figure IV- 9a shows the temperature dependence of Seebeck coefficient (α) of the AM-AN and ODP-AP samples. The Seebeck coefficient of both samples is negative in whole temperature range, indicating that electrons are the majority carriers (n-type). The temperature dependence of electrical conductivity is reported in Figure IV- 9b.

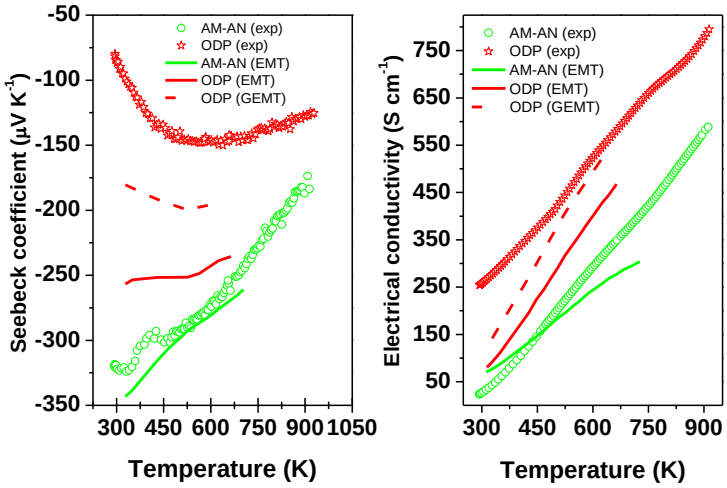

Figure IV- 9: Thermoelectric properties of AM-AN (red-circles) and ODP (green-stars) samples as a function of temperature: Seebeck coefficient (a), electrical conductivity (b). Dashed and solid lines represent the calculated thermoelectric properties of the "composite" according to EMT and GEMT,respectively.

Both samples show an increasing trend with the temperature, indicating a typical semiconducting behaviour. The AM-AN sample shows a lower electrical conductivity than that of the ODP-AP sample in the entire range the temperature, suggesting a difference in carrier concentration between the two samples. The literature values of thermopower and electrical conductivity of stoichiometric TiNiSn are quite dispersed, as already reported by Berche et al.[23] and Tang et al.[27]. As suggested by the complex solidification path (Figure IV- 5), formation of pure single phase TiNiSn is extremely difficult so that secondary phases are quite often present in different proportion depending on the processing method. Furthermore, the tendency of Ti to oxidize tends to deviate the alloy composition from the nominal one favoring the formation of secondary phases[23].

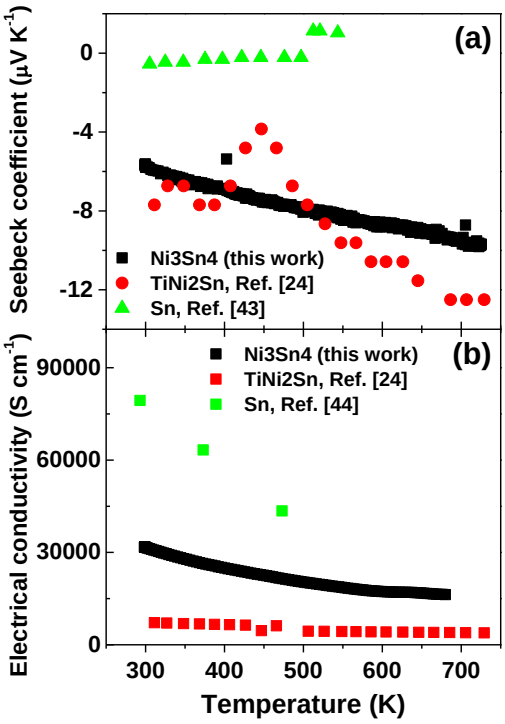

Figure IV- 10: Seebeck coefficient ,(a), and electrical conductivity, (b), as a function of the temperature for Ni3Sn4 (squares), TiNi2Sn (circles), and Sn (triangles).

Typical secondary phases forming are $TiNi_2Sn$, Sn, stannides, depending on the actual composition of the alloy. Figure IV- 10a and b show the temperature dependence of the Seebeck coefficient and electrical conductivity, respectively, for Ni_3Sn_4 (this work), $TiNi_2Sn$[37] and Sn[38]. The low values of $|\alpha|$ and the decreasing trend of σ with temperature indicate that all these phases have, as expected, a metallic behavior.

On the basis of the thermoelectric properties of pure TiNiSn[26] and each secondary phase, Figure IV-10, the electrical conductivity and

the Seebeck coefficient of the "composite" AM-AN and ODP samples were calculated according to the Effective Medium Theory (EMT)[39,40] where secondary phases are considered as spherical inclusions in the hosting matrix

$$\varphi_1 \frac{\sigma_1-\sigma_e}{\sigma_1+2\sigma_e} + \varphi_2 \frac{\sigma_2-\sigma_e}{\sigma_2+2\sigma_e} = 0 \qquad \text{(IV- 1)}$$

$$\varphi_1 \frac{\sigma_1(\alpha_e-\alpha_1)}{(2\sigma_e+\sigma_1)(2\lambda_e+\lambda_1)} + \varphi_2 \frac{\sigma_2(\alpha_e-\alpha_2)}{(2\sigma_e+\sigma_2)(2\lambda_e+\lambda_2)} = 0 \qquad \text{(IV- 2)}$$

where φ_1 and φ_2 are the volume fractions of phase 1 and phase 2, the subscripts 1, 2 and e refer to phase 1, phase 2 and the effective medium. An extension of the EMT is represented by the general effective medium theory (GEMT)[40] where elements of the percolation theory are considered, leading to the following equations for the electrical conductivity (σ) and thermal conductivity (κ), respectively

$$\varphi_1 \frac{\sigma_1^{1/t}-\sigma_e^{1/t}}{\sigma_1^{1/t}+A\sigma_e^{1/t}} + \varphi_2 \frac{\sigma_2^{1/t}-\sigma_e^{1/t}}{\sigma_2^{1/t}+A\sigma_e^{1/t}} = 0 \qquad \text{(IV- 3)}$$

$$\varphi_1 \frac{\kappa_1^{1/t}-\kappa_e^{1/t}}{\kappa_1^{1/t}+A\kappa_e^{1/t}} + \varphi_2 \frac{\kappa_2^{1/t}-\kappa_e^{1/t}}{\kappa_2^{1/t}+A\kappa_e^{1/t}} = 0 \qquad \text{(IV- 4)}$$

where $A = \frac{1-\varphi_c}{\varphi_c}$ (φ_c is the percolation threshold) and *t* is a constant related to microstructure asymmetry (t = 1 for a spherical shape).

On the basis of the EMT, Webman, Jortner and Cohen (WJC) developed the following equation for the thermopower of a two phases mixture[40]

$$\varphi_1 \frac{\sigma_1(\alpha_e-\alpha_1)}{(2\sigma_e+\sigma_1)(2\kappa_e+\kappa_1)} + \varphi_2 \frac{\sigma_2(\alpha_e-\alpha_2)}{(2\sigma_e+\sigma_2)(2\kappa_e+\kappa_2)} = 0 \qquad \text{(IV- 5)}$$

where α_1, α_2 and α_e are the Seebeck coefficients of phase 1, phase 2 and the effective medium. All the other terms of equation (IV- 5) are same of equations (IV- 1) and (IV- 2).

The combination of the WJC model and the general effective medium theory (GEMT), where percolation is considered, leads to the following equation for the thermopower of a two phases mixture

$$\varphi_1 \frac{\sigma_1^{1/t}(\alpha_e^{1/t}-\alpha_1^{1/t})}{(A\sigma_e^{1/t}+\sigma_1^{1/t})(A\kappa_e^{1/t}+\kappa_1^{1/t})} + \varphi_2 \frac{\sigma_2^{1/t}(\alpha_e^{1/t}-\alpha_2^{1/t})}{(A\sigma_e^{1/t}+\sigma_2^{1/t})(A\kappa_e^{1/t}+\kappa_2^{1/t})} = 0 \qquad \text{(IV- 6)}$$

In the equations (IV- 3) and (IV- 4) for the percolation model the constants *A* and *t* can be determined by a fitting procedure if the thermoelectric properties of the effective medium (σ_e or κ_e) are experimentally available over a wide range of the phase fraction φ. The same constants are then used in Eq. (IV- 6) to determined α_e.

We applied the EMT model to AM-AN and ODP samples using the thermoelectric properties of the pure constituents and the volume ratio of the phases determined by Rietveld refinement of the XRD patterns. On the one hand, for AM-AN sample, the thermoelectric properties of pure TiNiSn[26] and $TiNi_2Sn$[37] were considered. On the other hand, for ODP sample, the thermoelectric properties of pure TiNiSn and Ni_3Sn_4 were considered. The calculated Seebeck coefficient and the electrical conductivity are represented by the continuous lines in Figure IV- 9a

and Figure IV- 9b, respectively. The thick green lines and the thin red lines refer to the AM-AN and ODP samples, respectively. In the case of AM-AN sample, there is agreement between the calculated continuous green thick lines (EMT) and the experimental points (green open circles). Conversely, the EMT model fails to reproduce the experimental values of Seebeck coefficient and electrical conductivity (red open stars) for the ODP sample.

The backscattered electron micrograph of ODP sample (Fig. IV-8b) shows that the secondary phase (Ni_3Sn_4) is segregated at the grain boundaries of the half Heusler phase in the matrix and tends to form a connected network. On the basis of this observation, the Seebeck coefficient and the electrical conductivity of ODP sample were calculated assuming the percolation model, using Eq. (IV-3) and Eq. (IV-6), respectively. In our case, the A and t parametes cannot be obtained by fitting because the experimental value of σ_e is available only for a single value of φ. Thus, the arbitrary values A=5.25 (corresponding to φ_c=16%) and t=2 (non spherical particles)[40] were used to find the solutions of Equations (IV-3), (IV-4) and (IV-6). The calculated values of the Seebeck coefficient and the electrical conductivity are represented by the dashed red lines in Figure IV-9(a) and Figure IV-9(b), respectively. The percolation model shows a better agreement with the experimental data than the EMT model. Some discrepancies between calculated and experimental values are

still present likely due to the use of not optimized values of the parameters *A* and *t*.

Figure IV-11a and Figure IV-11b show the values of the Seebeck coefficient and electrical conductivity at 328 K, respectively, for stoichiometric TiNiSn as a function of the secondary phases fraction estimated by quantitative analysis of the XRD patterns both from this work and the literature[21,25,26,28]. The selection of the literature data was limited to samples showing values of the lattice constant (table IV-2) close to the one of stoichiometric TiNiSn[26], so that the simultaneous significant variation of the interstitial Ni content could be neglected. The different secondary phases (Sn, Ni_3Sn_4 and $TiNi_2Sn$) in the samples considered are represented by different symbols (diamonds, circles and squares, respectively) and colors (blue, red and green, respectively). The absolute value of the Seebeck coefficient clearly decreases as the total amount of secondary phases increases due to their metallic behavior, Figure IV-11b. Accordingly, the electrical conductivity raises as the total amount of secondary phases increases, Figure IV-a, even if the relationship between these two quantities is apparently less evident than the corresponding trend of the Seebeck coefficient, Figure IV-11b. The larger spread of the data in Figure IV-11b can be explained by the significant difference in density of the samples (from 80 % to almost 100 %), that strongly affects the measurement of the electrical conductivity. Quite interestingly, the thermoelectric properties of the two phases systems considered in

Figure IV-11a and Figure IV-11b scale with the fraction of the secondary phase irrespectively of the type of phase. Also in this case, we applied EMT (continuous lines) and percolation (dashed lines) models to describe the thermoelectric behavior of two phases systems as a function of the amount of secondary phases. In the case of the percolation model, the values of parameters A and t are same as in Figure IV-9a and Figure IV-9b. A better agreement between experimental and calculated values is obtained when percolation is assumed even for rather small amount of secondary phase. In the case of ODP sample (containing Ni_3Sn_4 as a second phase), an interconnecting network of the secondary phase is visible in the backscattered SEM image. In the case of the samples containing Sn[23,30], no information about the microstructure is given by the authors. However, since Sn has a low melting point (505 K) we can hypothesize that it is segregated at the grain boundaries "decorating" the grains of the matrix and creating a percolating path.

Table IV- 2
Lattice parameters and corresponding literature references for selected TiNiSn samples whose thermoelectric properties are reported in Figure IV-11.

Composition	Lattice parameter, Å	Ref.
TiNiSn	5.9285	21
	5.9290	25
	5.9304	28
	5.9297	36

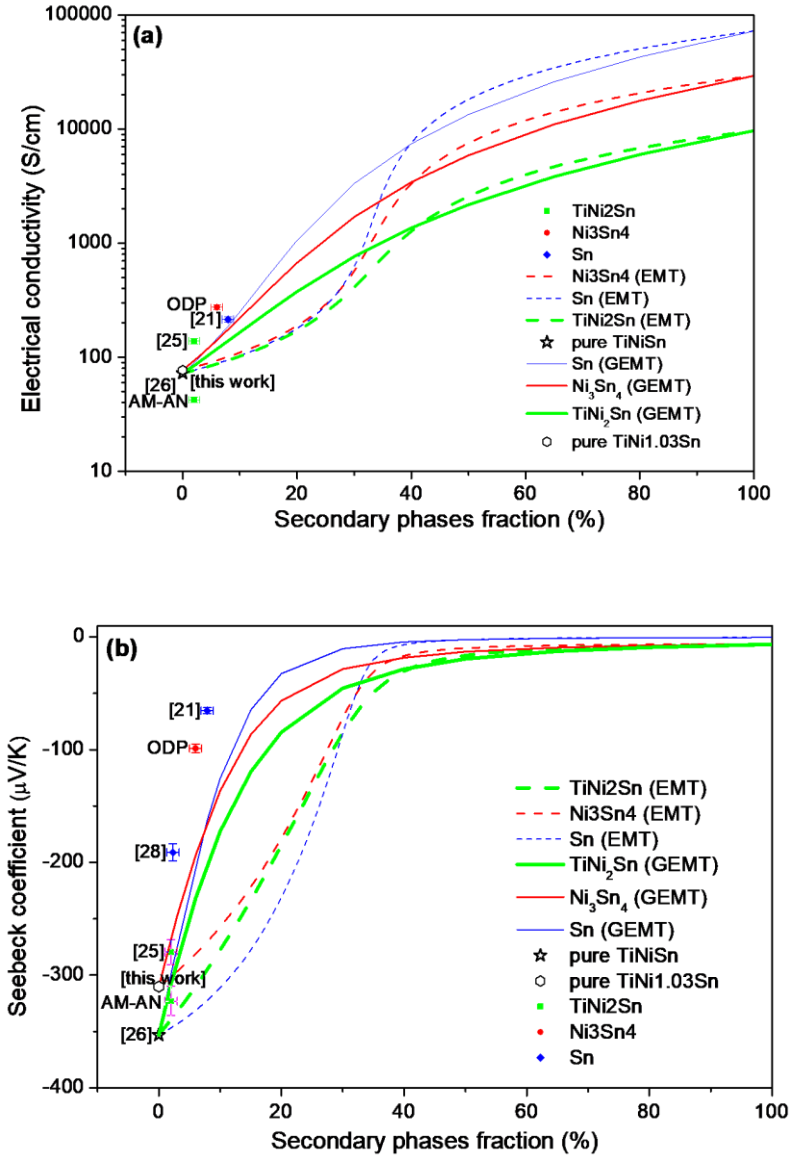

Figure IV- 11: Electrical conductivity (a), and Seebeck coefficient (b), at 328 K as a function of the total amount of secondary phases. Symbols refer to measured data from the literature and this work. Dashed and solid lines represent the calculated thermoelectric properties of the "composite" according to EMT and GEMT,respectively, for different types of secondary phase ($TiNi_2Sn$, Ni_3Sn_4, Sn). Symbols and lines with the same color refer to the same secondary phase.

- **Thermal conductivity**

Figure IV- 12 shows the temperature dependence of thermal conductivity of AM-AN and ODP-AP samples.

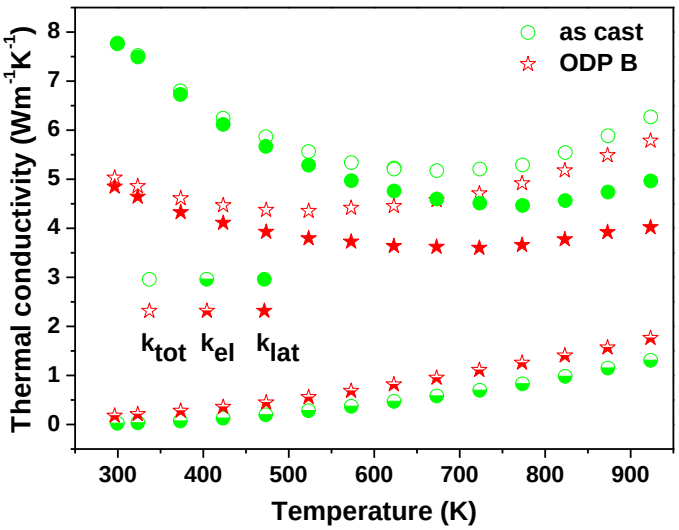

Figure IV- 12: Thermal conductivities of AM-AN (green-circles) and ODP (red-stars) samples as a function of temperature

The total thermal conductivity, κ_{tot}, was obtained from the measurement of thermal diffusivity, specific heat and density. The electronic contribution was obtained by applying the Wiedemann-Franz law below reported:

$$\kappa_{el} = L\sigma T \qquad \text{(IV- 3)}$$

where L is the Lorenz's constant, σ is the electrical conductivity, T is the absolute temperature, while the lattice contribution, κ_{lat}, was

estimated as the difference between κ_{tot} and κ_{el}. The Lorenz's constant was calculated using the following equation[41]:

$$L = 1.5 + \exp\left[-\frac{|S|}{116}\right] \qquad \text{(IV- 4)}$$

On the one hand, the ODP sample shows a slight larger electronic contribution to the thermal conductivity, κ_{el}, with respect to AM-AN sample, as a consequence of its larger electrical conductivity. On the other hand, AM-AN sample shows a significantly larger lattice contribution to the thermal conductivity, $\kappa_{lat} = \kappa_{tot}\text{-}\kappa_{el}$, that leads to a larger total thermal conductivity with respect to ODP sample. The values of κ_{tot} measured for AM-AN are among the largest reported in literature together with those of samples prepared with analogous processing routes (i.e. arc/induction melting plus annealing)[25,42] and can be taken as a reference for a "defect-free" sample with a coarse relaxed microstructure. The lattice thermal conductivity at room temperature of the ODP sample (with an average grain size around 1 μm) normalized by the one of the AM-AN sample is about 0.62 for the as sintered sample and raises to 0.65 after thermal cycling (the measurement of the second cycle is not shown). Bhattacharya et al.[30] estimated the effect of grain boundary scattering on the lattice thermal conductivity of TiNiSn-based half Heusler compounds applying the model proposed by Sharp et al.[22] It was shown that phonon scattering by grain boundaries becomes relevant only when the average grain size is below 50 μm. Considering a grain size around 1 μm, that is

comparable with the one estimated for the ODP sample, the predicted lattice thermal conductivity is about 0.68 times the value of a coarse grain sample (average grain size above 50 µm), in good agreement with the experimental values obtained for the ODP sample, as shown in Figure IV- 13. The slightly lower value of the normalized lattice thermal conductivity in the as sintered ODP sample can be explained by the presence of interstitial Ni in the half Heusler cell (TiNiSn_2) that induces further scattering of the phonon.

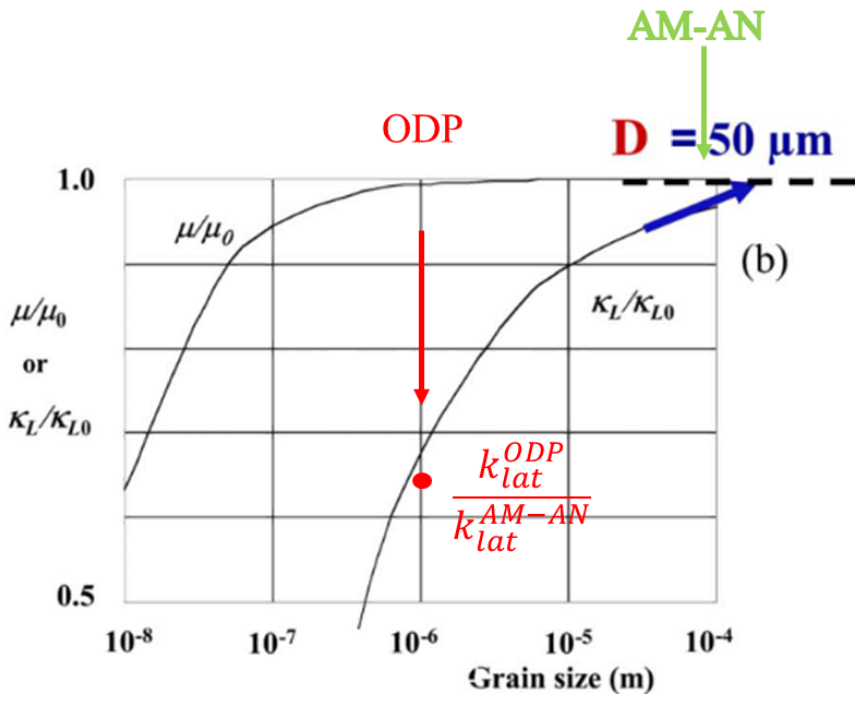

Figure IV- 13: The dependence of the lattice thermal conductivity and electrical thermal conductivity as function of the grain size.

- **Power factor and figure of merit ZT**

The power factor of the two samples is reported in Figure IV- 14a. In the AM-AN sample, the larger values of the Seebeck coefficient compensate the lower values of electrical conductivity, leading to a larger power factor with respect to ODP sample. The overall thermoelectric performance is represented by the figure of merit, ZT, as reported in Figure IV- 14b. Around 850 K the figure of merit of the AM-AN sample shows a maximum value of 0.3 that is larger than the maximum value (0.2) observed for the ODP-AP sample. The larger value of ZT for the AM-AN sample is due to the larger power factor that compensate the larger thermal conductivity. The maximum values of ZT obtained for the AM-AN sample is in line with the typical value (about 0.30-0.35) found for nearly single phase TiNiSn reported in literature[25,42].

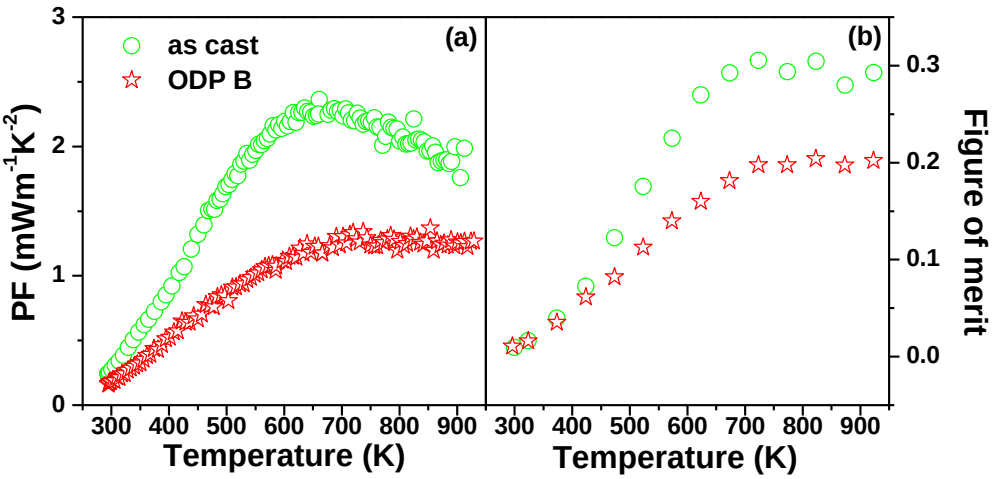

Figure IV- 14: Power factor (a) and Figure of merit (b) of AM-AN (green-circles) and ODP (red-stars) samples as a function of temperature

4.4.4 Thermal cycling and oxidation

To evaluate the reproducibility of the thermoelectric properties of TiNiSn, the AM-AN sample was thermally cycled. Figure IV- 15 shows the temperature dependence of Seebeck coefficient, electrical conductivity and power factor after cycling. The absolute value of the Seebeck coefficient during the 2^{nd} cycle of measurement, from room temperature to 750 K, decreases with respect to the first cycle, while electrical conductivity increases with respect to the 1^{st} cycle. This leads to a non-significant variation in the power factor, as shown in Figure IV- 15.

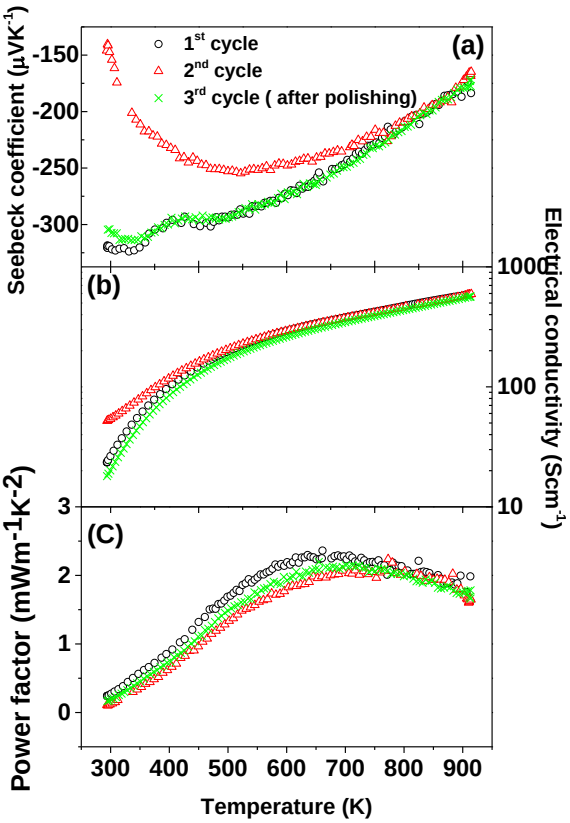

Figure IV- 15: The temperature dependence of Seebeck coefficient (a), electrical conductivity (b) and power factor (c) measured upon different thermal cycles.

The parallel beam XRD pattern (graze angle geometry), shown in *Figure IV- 16*, shows only the reflections of TiO_2 and Ni_3Sn_4 phases, that cannot be detected when the measurement is performed with Bragg-Brentano geometry, indicating the formation of a surface layer of titanium oxide and Ni_3Sn_4.

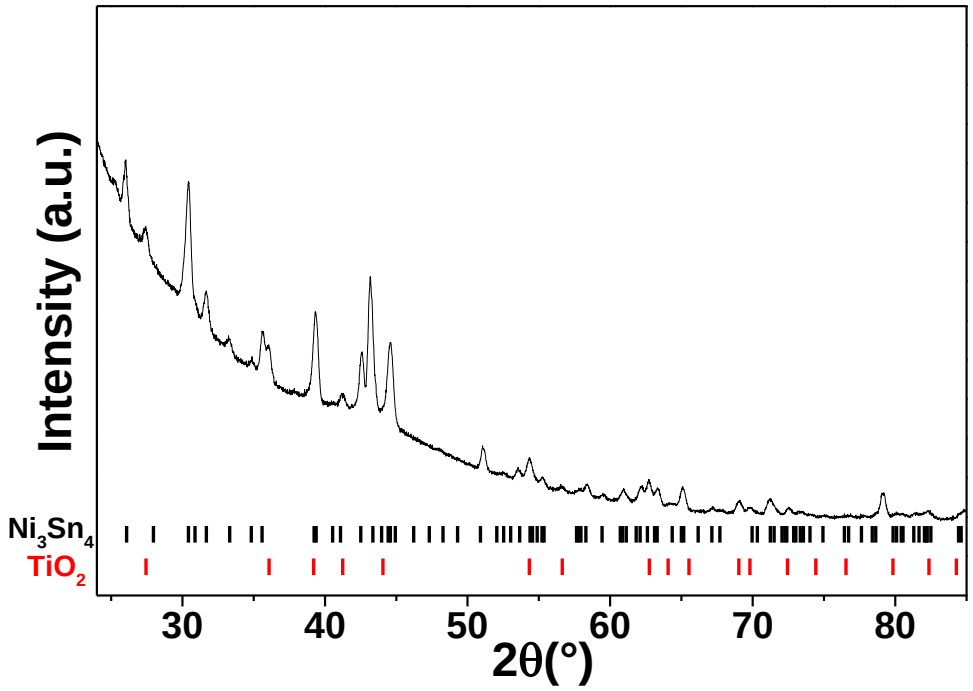

Figure IV- 16: Parallel beam XRD pattern of the AM-AN sample after thermoelectric cycling.

According to the XRD results, the backscattered SEM image, shown in Figure IV- 17, shows the presence of a thin layer of titanium oxide and the presence of the secondary metallic phase Ni_3Sn_4 that can be explained by the depletion of Ti from the matrix due to its oxidation on the surface.

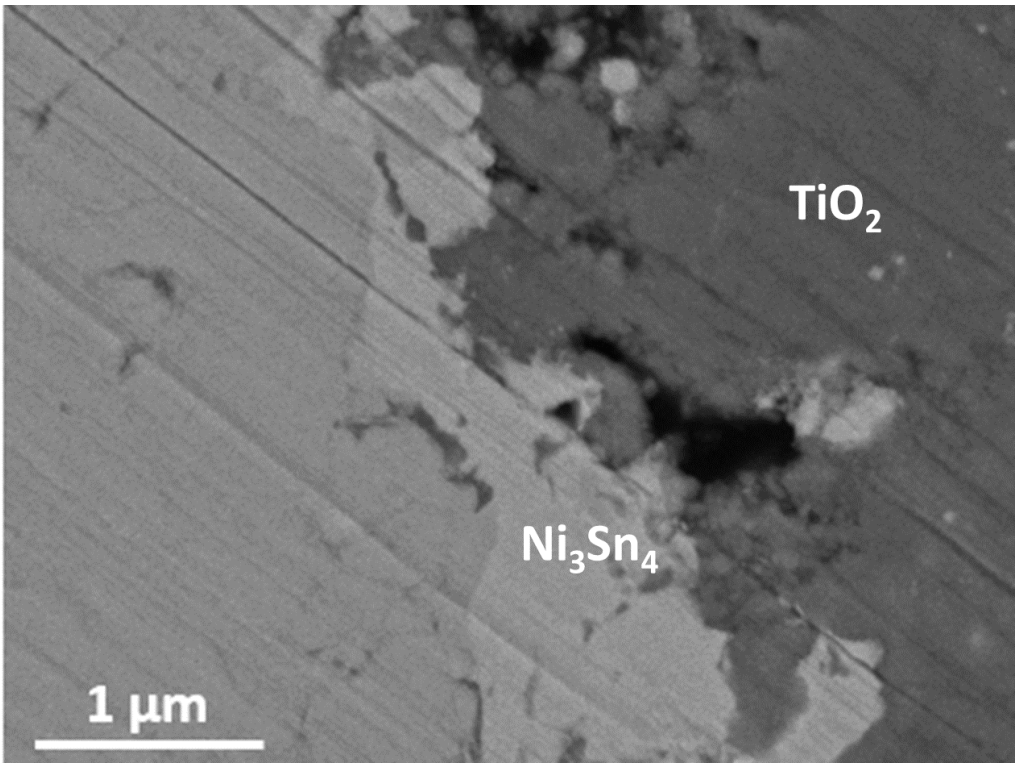

Figure IV- 17: Backscattered SEM image of the AM-AN sample after the second cycle.

After polishing the surface, both the Seebeck coefficient and the electrical conductivity, measured during the third cycle, return to the values of the first cycle, indicating that the original thermoelectric properties were restored by removing the altered layer on the surface (TiO_2 and Ni_3Sn_4). The curves of the the Seebeck coefficient for the first and second cycles overlap around 700-750 K, suggesting that oxidation starts in this temperature range. This was confirmed by TGA measurement where a mass increase due to oxidation occurs around 700 K, as shown in Figure IV- 18.

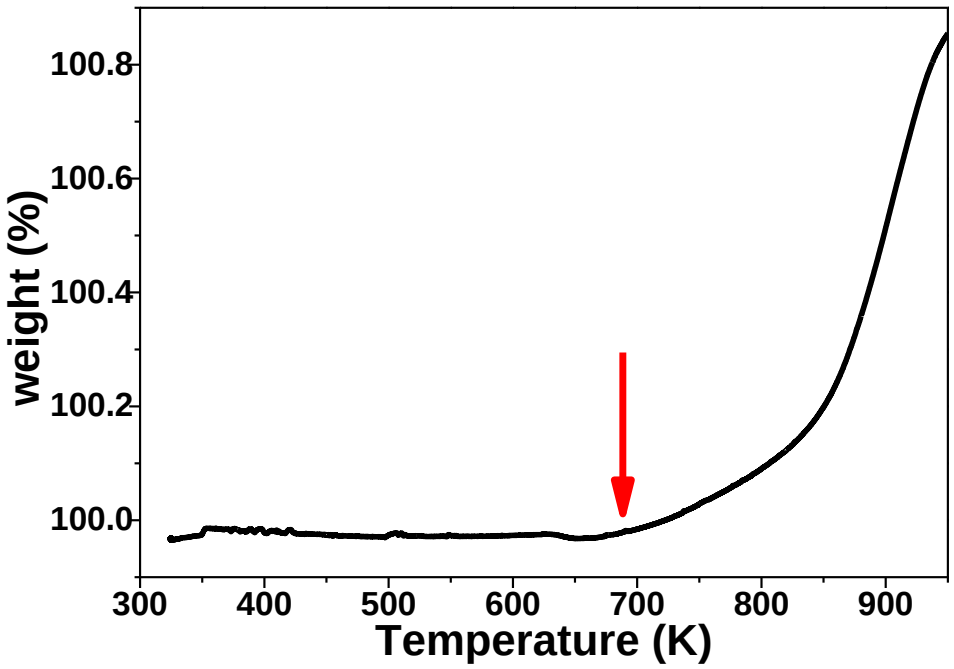

Figure IV- 18: TGA of the AM-AN sample.

To avoid the oxidation and degradation of thermoelectric materials, many efforts were made to look for possible solutions. Among the possible solutions studied, the use of a hybrid protective coating showed a great interest, as the procedure does not require the need of expensive equipment. Thus, as reported in Refs.[43–45] the hybrid protective coating is an effective method to provide a barrier coating to avoid the oxidation.

4.5 Conclusions

In this work, dense TiNiSn bulk samples were obtained using two different processing routes (i.e. arc melting plus annealing and rapid solidification followed by sintering). The solidification of the arc

melted (AM) sample can be described by the Scheil model, that assumes complete miscibility in the liquid and absence of diffusion in the solid. Calculated stable and metastable isopleth Ni-TiSn, obtained maintaining and suspending the $TiNi_2Sn$ phase, showed that a liquid undercooling of about 70 K is necessary to avoid the primary solidification of $TiNi_2Sn$ and obtaining almost TiNiSn single phase, in accordance with the experimental results of the rapidly solidified (RS) samples. Annealing of the AM sample and open die pressing of the RS sample allow to obtain homogenous and dense massive specimens (AM-AN and ODP-AP, respectively) for thermoelectric characterization. The different thermoelectric properties of the two samples were correlated to the corresponding structural and microstructural features within a literature survey. The behavior of the lower absolute value of thermopower and the larger electrical conductivity of ODP sample with respect to the AM-AN sample was explained by the larger amount of residual metallic secondary phases. The lower thermal conductivity of the ODP-AP sample with respect to the AM-AN sample was explained by the increased phonon scattering induced by the finer microstructure obtained by rapid solidification and maintained during sintering by ODP. Finally, AM-AN sample shows a larger ZT than ODP-AP sample with a maximum of 0.3 at 850 K due to the larger power factor that compensates the larger thermal conductivity. The different values obtained for the Seebeck coefficient and electrical conductivity of the AM-AN sample

during the 2nd measurement cycle is due to the formation of a thin layer of titanium oxide that involves the formation of the secondary metallic phase Ni_3Sn_4 due to the decrease of Ti in alloy. However, this does not lead to a significant variation in the power factor. The original thermoelectric properties can be restored (3rd cycle) by polishing the surface and removing the altered layes. The use of hybrid protective coating could be is an effective solution to avoid the oxidation.

References

1. Tsunegi, S., Sakuraba, Y., Oogane, M., Takanashi, K. & Ando, Y. Large tunnel magnetoresistance in magnetic tunnel junctions using a Co 2MnSi Heusler alloy electrode and a MgO barrier. *Appl. Phys. Lett.* (2008). doi:10.1063/1.2987516

2. Chadov, S. *et al.* Tunable multifunctional topological insulators in ternary Heusler compounds. *Nat. Mater.* (2010). doi:10.1038/nmat2770

3. Tafti, F. F. *et al.* Superconductivity in the noncentrosymmetric half-Heusler compound LuPtBi: A candidate for topological superconductivity. *Phys. Rev. B - Condens. Matter Mater. Phys.* (2013). doi:10.1103/PhysRevB.87.184504

4. Planes, A., Mãosa, L. & Acet, M. Magnetocaloric effect and its relation to shape-memory properties in ferromagnetic Heusler alloys. *J. Phys. Condens. Matter* (2009). doi:10.1088/0953-8984/21/23/233201

5. Chen, S. & Ren, Z. Recent progress of half-Heusler for moderate temperature thermoelectric applications. *Mater. Today* **16**, 387–395 (2013).

6. Hohl, H. *et al.* New compounds with MgAgAs-type structure: NbIrSn and NbIrSb. *J. Phys. Condens. Matter* (1998). doi:10.1088/0953-8984/10/35/016

7. Schierning, G. *et al.* Concepts for medium-high to high temperature thermoelectric heat-to-electricity conversion: a review of selected materials and basic considerations of module design. *Transl. Mater. Res.* (2015). doi:10.1088/2053-1613/2/2/025001

8. Kimura, Y. & Chai, Y. W. Ordered Structures and Thermoelectric Properties of MNiSn (M = Ti, Zr, Hf)-Based Half-Heusler Compounds Affected by Close Relationship with Heusler Compounds. *Jom* **67**, 233–245 (2015)

9. Hohl, H. *et al.* Efficient dopants for ZrNiSn-based thermoelectric materials. *J. Phys. Condens. Matter* (1999). doi:10.1088/0953-8984/11/7/004

10. Gofryk, K., Kaczorowski, D., Plackowski, T., Leithe-Jasper, A. & Grin, Y. Magnetic and transport properties of rare-earth-based half-Heusler phases RPdBi: Prospective systems for topological quantum phenomena. *Phys. Rev. B - Condens. Matter Mater. Phys.* (2011). doi:10.1103/PhysRevB.84.035208

11. Pavlosiuk, O. *et al.* Magnetic structures of REPdBi half-Heusler bismuthides (RE = Gd, Tb, Dy, Ho, Er). *Phys. B Condens. Matter* (2018). doi:10.1016/j.physb.2017.10.062

12. Bos, J. W. G. & Downie, R. A. Half-Heusler thermoelectrics: A complex class of materials. *Journal of Physics Condensed Matter* (2014). doi:10.1088/0953-8984/26/43/433201

13. Gautier, R. *et al.* Prediction and accelerated laboratory discovery of previously unknown 18-electron ABX compounds. *Nat. Chem.* **7**, 308–316 (2015).

14. Zhu, T., Fu, C., Xie, H., Liu, Y. & Zhao, X. High Efficiency Half-Heusler Thermoelectric Materials for Energy Harvesting. *Adv. Energy Mater.* **5**, 1–13 (2015).

15. Huang, L. *et al.* Recent progress in half-Heusler thermoelectric materials. *Mater. Res. Bull.* **76**, 107–112 (2016).

16. Aliev, F. G. Optical properties of the vacancy MNiSn lattices (M = Ti , Zr , Hf). (2017).

17. Morelli, D. T. & Meisner, G. P. Transport properties of pure and doped mnisn (m=zr, hf). *Phys. Rev. B - Condens. Matter Mater. Phys.* (1999). doi:10.1103/PhysRevB.59.8615

18. Cook, B. A., Harringa, J. L., Tan, Z. S. & Jesser, W. A. TiNiSn: A gateway to the (1,1,1) intermetallic compounds. in *International Conference on Thermoelectrics, ICT, Proceedings* (1996). doi:10.1109/ict.1996.553270

19. Zou, M., Li, J. F., Du, B., Liu, D. & Kita, T. Fabrication and thermoelectric properties of fine-grained TiNiSn compounds. *J. Solid State Chem.* **182**, 3138–3142 (2009).

20. Gürth, M. *et al.* On the constitution and thermodynamic modelling of the system Ti-Ni-Sn. *RSC Adv.* **5**, 92270–92291 (2015).

21. Berry, T. *et al.* Improving thermoelectric performance of TiNiSn by mixing MnNiSb in the half-Heusler structure. *Phys. Chem. Chem. Phys.* (2017). doi:10.1039/c6cp06859f

22. Sharp, J. W., Poon, S. J. & Goldsmid, H. J. Boundary Scattering and the Thermoelectric Figure of Merit. *Phys. Status Solidi Appl. Res.* (2001). doi:10.1002/1521-396X(200110)187:2<507::AID-PSSA507>3.0.CO;2-M

23. Berche, A. & Jund, P. Oxidation of half-Heusler NiTiSn materials: Implications for thermoelectric applications. *Intermetallics* **92**, 62–71 (2018).

24. Kirievsky, K., Shlimovich, M., Fuks, D. & Gelbstein, Y. An ab initio study of the thermoelectric enhancement potential in nano-grained TiNiSn. *Phys. Chem. Chem. Phys.* (2014). doi:10.1039/c4cp02868f

25. Douglas, J. E. *et al.* Phase stability and property evolution of biphasic Ti-Ni-Sn alloys for use in thermoelectric applications. *J. Appl. Phys.* (2014). doi:10.1063/1.4862955

26. Downie, R. A., Smith, R. I., Maclaren, D. A. & Bos, J. W. G. Metal distributions, efficient n-type doping, and evidence for in-gap states in TiNiM<inf>y</inf>Sn (M = Co, Ni, Cu) half-Heusler nanocomposites. *Chem. Mater.* **27**, 2449–2459 (2015).

27. Tang, Y. *et al.* Impact of Ni content on the thermoelectric properties of half-Heusler TiNiSn. *Energy Environ. Sci.* **11**, 311–320 (2018).

28. Barczak, S. A. *et al.* Impact of interstitial Ni on the thermoelectric properties of the half-Heusler TiNiSn. *Materials (Basel).* (2018). doi:10.3390/ma11040536

29. Schrade, M. *et al.* The role of grain boundary scattering in reducing the thermal conductivity of polycrystalline XNiSn (X = Hf, Zr, Ti) half-Heusler alloys. *Sci. Rep.* (2017). doi:10.1038/s41598-017-14013-8

30. Bhattacharya, S. *et al.* Effect of boundary scattering on the thermal conductivity of TiNiSn-based half-Heusler alloys. *Phys. Rev. B - Condens. Matter Mater. Phys.* **77**, 1–8 (2008).

31. Fu, C. *et al.* High band degeneracy contributes to high thermoelectric performance in p-type Half-Heusler compounds. *Adv. Energy Mater.* (2014). doi:10.1002/aenm.201400600

32. Appel, O., Zilber, T., Kalabukhov, S., Beeri, O. & Gelbstein, Y. Morphological effects on the thermoelectric properties of Ti0.3Zr0.35Hf0.35Ni1+δSn alloys following phase separation. *J. Mater. Chem. C* (2015). doi:10.1039/c5tc03214h

33. Aversano, F. *et al.* Thermoelectric Properties of TiNiSn Half Heusler Alloy Obtained by Rapid Solidification and Sintering. *J. Mater. Eng. Perform.* **27**, 6306–6313 (2018).

34. Ceresara, S., Fanciulli, C., Passaretti, F. & Vasilevskiy, D. Texturing of (Bi0.2Sb0.8)2Te3 nanopowders by open die pressing. *J. Electron. Mater.* **42**, 1529–1534 (2013).

35. Boldrini, S. *et al.* Test rig for high-temperature thermopower and electrical conductivity measurements. *J. Electron. Mater.* (2013). doi:10.1007/s11664-012-2437-3

36. Verma, N. *et al.* Microstructure Evolution of Biphasic TiNi1+xSn Thermoelectric Materials. *Metall. Mater. Trans. A Phys. Metall. Mater. Sci.* **47**, 4116–4127 (2016).

37. Downie, R. A., Smith, R. I., Maclaren, D. A. & Bos, J. W. G. Metal distributions, efficient n-type doping, and evidence for in-gap states in TiNiM<inf>y</inf>Sn (M = Co, Ni, Cu) half-Heusler nanocomposites. *Chem. Mater.* (2015). doi:10.1021/cm5045682

38. Fiflis, P., Kirsch, L., Andruczyk, D., Curreli, D. & Ruzic, D. N. Seebeck coefficient measurements on Li, Sn, Ta, Mo, and W. *J. Nucl. Mater.* (2013). doi:10.1016/j.jnucmat.2013.03.043

39. Landauer, R. The electrical resistance of binary metallic mixtures. *J. Appl. Phys.* (1952). doi:10.1063/1.1702301

40. Webman, I., Jortner, J. & Cohen, M. H. Critical exponents for percolation conductivity in resistor networks. *Phys. Rev. B* (1977). doi:10.1103/PhysRevB.16.2593

41. Kim, H. S., Gibbs, Z. M., Tang, Y., Wang, H. & Snyder, G. J. Characterization of Lorenz number with Seebeck coefficient measurement. *APL Mater.* (2015). doi:10.1063/1.4908244

42. Katayama, T., Kim, S. W., Kimura, Y. & Mishima, Y. The effects of quaternary additions on thermoelectric properties of TiNiSn-based half-Heusler alloys. *J. Electron. Mater.* **32**, 1160–1165 (2003).

43. Ning, H., Reece, M. J., Smeacetto, F. & Salvo, M. Oxidation protective glass–ceramic coating for higher manganese silicide thermoelectrics. *J. Mater. Sci.* (2016). doi:10.1007/s10853-016-0192-1

44. Gucci, F. *et al.* Oxidation protective hybrid coating for thermoelectric materials. *Materials (Basel).* (2019). doi:10.3390/ma12040573

45. Salvo, M. *et al.* Glass-ceramic oxidation protection of higher manganese silicide thermoelectrics. *J. Eur. Ceram. Soc.* (2019). doi:10.1016/j.jeurceramsoc.2018.01.007

CHAPTER V:

SYNTHESIS AND CHARACTERIZATION OF TaCoSn: A NEW THERMOELECTRIC HALF-HEUSLER COMPOUND

5.1 State of art and aim of work

As said in the previous chapter half-Heusler compounds are promising candidates for high temperature power generation because of their high power factor[1,2], good thermal stability[3] and excellent mechanical properties[4]. However, the intrinsically large lattice thermal conductivity of most half-Heusler limits their thermoelectric applications. ZrCoSb and NbFeSb are among the best p-type half-Heusler compounds investigated[5–11]. On the one hand, new p-type half-Heusler compounds with promising thermoelectric performance were recently discovered. Zhu et al.[3,12] reported for p-type $ZrCoBi_{0.65}Sb_{0.15}Sn_{0.20}$ and $Ta_{0.74}V_{0.1}Ti_{0.16}FeSb$ half-Heusler compounds a peak of ZT of about 1.42 and 1.52 at 973 K respectively. On the other hand, progress on the n-type half-Hesuler remains sluggish. The maximum value reported for n-type half-Heusler is around unity for the ZrNiSn-based compounds. Joshi et al.[13] reported for nanostructured n-type $Hf_{0.75}Zr_{0.25}NiSn_{0.99}Sb_{0.01}$ half-Heusler a ZT peak around 1.0 at 873-973 K, while Xie et al.[14] reported for n-type $ZrNiSn_{0.99}Sb_{0.01}$ half-Heusler a ZT peak of about 0.8 at 875 K. Thus, it is extremely important to find and study new n-type half-Heusler compounds that have comparable properties to p-type half-Heusler compounds for the development of high-efficiency thermoelectric modules.

First principle calculation is a very efficient tool to accelerate the discovery of new possible thermoelectric materials before

experimental realization. Gautier et al. [15] studied, by first principle approach, the thermodynamic stability of about 400 possible ternary compound maintaining an Valence Electron Count (VEC) equal to 18.

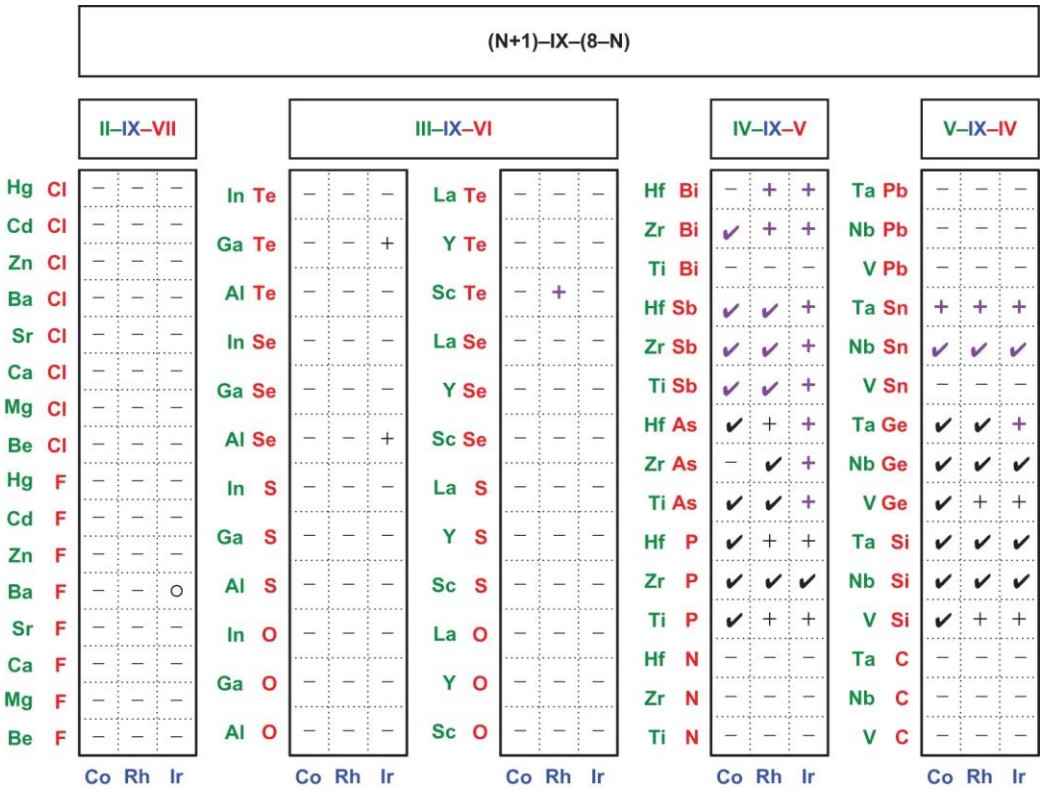

Figure V- 1: The group IX elements are shown in blue, (N+1) in green and (8−N) in red. Tick, previously reported; plus sign, unreported and predicted here to be stable; minus sign, unreported and predicted here to be unstable; circle, too close to call. The compounds that have half-Heusler type structure are denoted by the bold violet symbols.

Figure V- 1 shows part of the results obtained by Gautier[15], where the tick indicate the ternary compounds experimentally verified[16–21], the minus sign the ternary compounds predicted to be unstable e never experimentally synthesized, the plus sign the ternary compounds predicted to be stable but which have not been experimentally verified

yet while the compounds that have half-Heusler type structure are denoted by the bold violet symbols. Therefore, TaCoSn was predicted to be stable and have a half-Heusler type structure but never experimentally synthesized. Currently, Zakutayev et al.[22] synthesized TaCoSn twice. The first time as bulk by solid-liquid reaction, but the sample contained many Co rich impurities, such as CoSn, $TaCo_2$ and $CoSn_2$, while the second time as thin film by co-sputtering obtaining TaCoSn single phase. Currently, there have been no experimental data reported on thermoelectric properties of TaCoSn despite the calculated thermoelectric performance is predicted to be high[23,24]. Therefore, aim of this chapter is the synthesis of the TaCoSn half-Heusler phase in bulk form to perform structural, microstructural and thermoelectric characterization.

5.2 Experimental

The synthesis of TaCoSn was attempted according to two procedures. At first, arc melting of the elemental metals in form of small slags was performed. Secondly, elemental powders of Ta, Co and Sn with 99.95 %, 99.8 % and 99.85 % purity, respectively, were mechanically alloyed using Fritsch Pulverisette-6 high-energy planetary ball mill with zirconium oxide (ZrO_2) jar and balls. The ball to powder weight ratio was maintained as 8:1 and the milling was carried out dry under Ar controlled atmosphere. The speed of milling was maintained at 400 rpm during the entire milling process. Mechanical alloying of the elemental blends was carried out for 70 h. Because of the cold-

welding effect, a fraction (30 %) of the milled material was attached to the walls of the jar. The attached materials was mechanically removed from the jar wall after 50 h of milling and the process was continued for other 20 hours to favor complete homogenization of the product. The powders were then compacted by cold pressing (30 MPa) and sealed in a quartz tube under a vacuum of about 10^{-5} mbar. The annealing was performed in the muffle furnace at two different temperature, 873 K and 973 K, for 1 h.

Structural characterization was performed by X-ray diffraction (XRD) using Bragg-Brentano geometry (Panalytical X'Pert Pro) with Cu Kα radiation (Kα = 1.5406 Å). Rietveld refinement of the measured diffraction patterns was performed using Maud software[25]. XRD measurements were carried out on ground powders in order to remove possible effects of preferential crystallographic orientations. Microstructural observations were performed by scanning electron microscopy (SEM) using a ZEISS EVO 50 XVP-LaB6 equipped with an Oxford Instruments INCA -Energy 250 for energy-dispersive X-ray analysis (EDX). Thermal stability and phase transformations of the milled powders were studied by differential thermal analysis in two temperature ranges. Between room temperature and 973 K using a TA Q-200 DSC, working under nitrogen flow, was employed. In this case, the sample masses used for DSC measurements were about 50 milligrams. Heating rates of 2, 5, 10, 20, and 40 $Kmin^{-1}$ were employed in order to study the kinetics of thermally activated

transformations. Phase transformations at higher temperature (673-1273 K) were studied using a SETARAM High Temperature-Differential Scanning Calorimeter (HT-DSC) using a scan rate of 10 $Kmin^{-1}$ and working under helium flow.

Seebeck coefficient, α, and electrical conductivity σ, were measured under He flow in the temperature range from room temperature to 875 K by using a custom test apparatus described in chapter 3 [26]. The relative error of α and σ was estimated to around 4 and 5 % respectively. The mass density (ρ) was estimated, with a relative error of 5 %, using the ratio between the mass and the volume of regularly shaped samples.

5.3 Results and Discussions

5.3.1 Formation of HH TaCoSn

The pure elements could not be successfully alloyed by arc melting because of the large difference between their melting points and because the high temperature necessary to melt Ta involves the reaction between Sn and copper plate. Therefore, we opted for a method of synthesis in the solid state by mechanical alloying.

Figure V- 2 shows the effect of mechanical alloying of elemental powders as a function of milling time, studied by XRD.

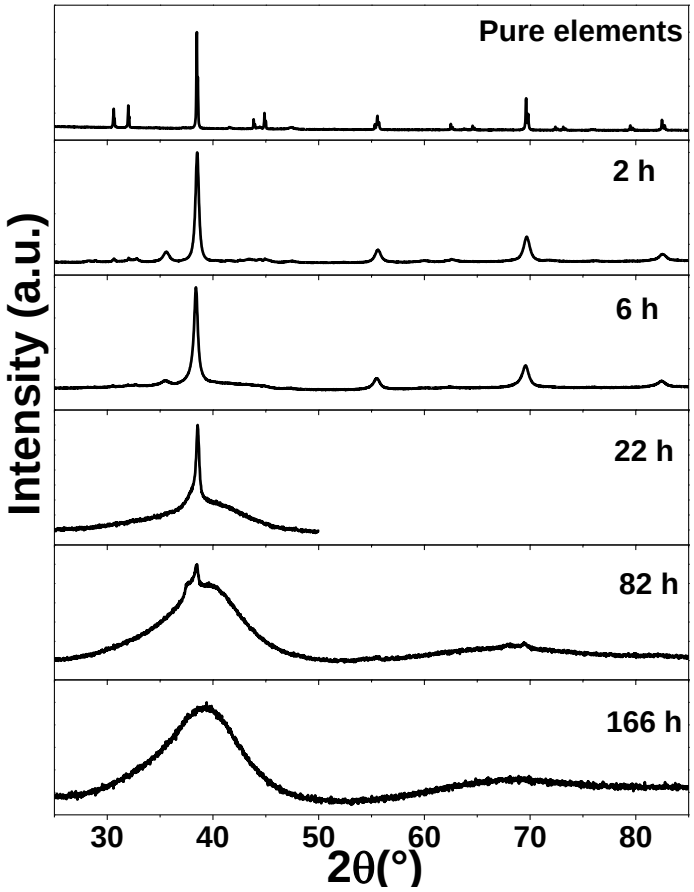

Figure V- 2: The XRD pattern of the elemental powder as function of the milling time.

As milling proceeds, from 0 to 166 h, crystallographic reflections disappear leaving place to a broad halo, suggesting the progressive amorphization of the powders. Scanning electron microscopy (SEM) was performed together with the energy dispersive spectroscopy (EDS) mapping to verify the quality of the prepared sample. The EDS mapping displayed in Figure V- 3, shows that all elements are distributed homogeneously in the sample within the detection limit of the technique.

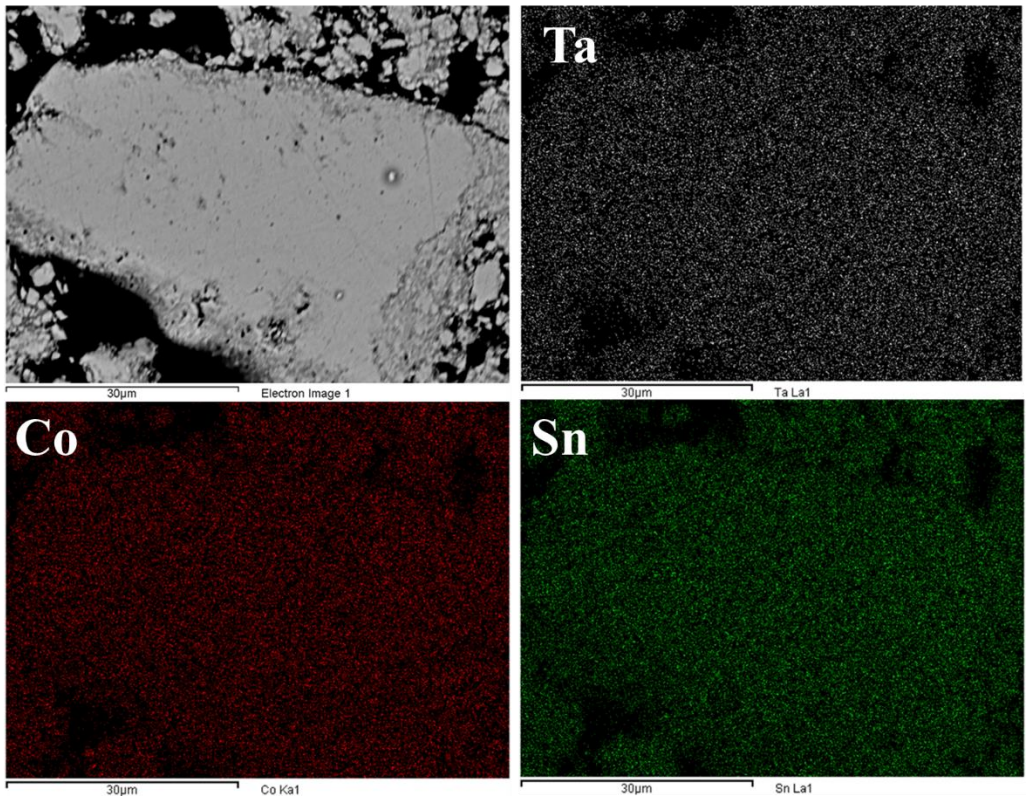

Figure V- 3: EDS mapping of TaCoSn after ball milling

The HTDSC trace of the ball milled powder, reported in Figure V- 4, shows the presence of three peaks during the heat ramp, an exothermic peak at 753 K and two endothermic peaks at 1011K and 1153 K respectively, while no peak was observed during the cooling ramp.

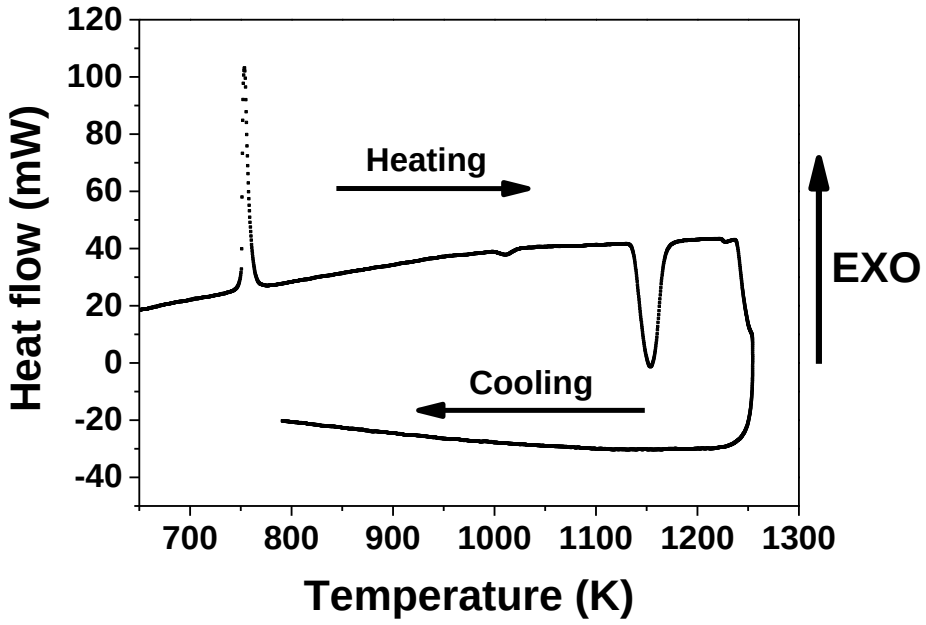

Figure V- 4: HTDSC trace of ball milled TaCoSn

The first exothermic peak observed in Figure V- 4 is irreversible and is related to the crystallization of the metastable amorphous phase into an half Heusler structure, as shown by the crystallographic reflections in Figure V-5.

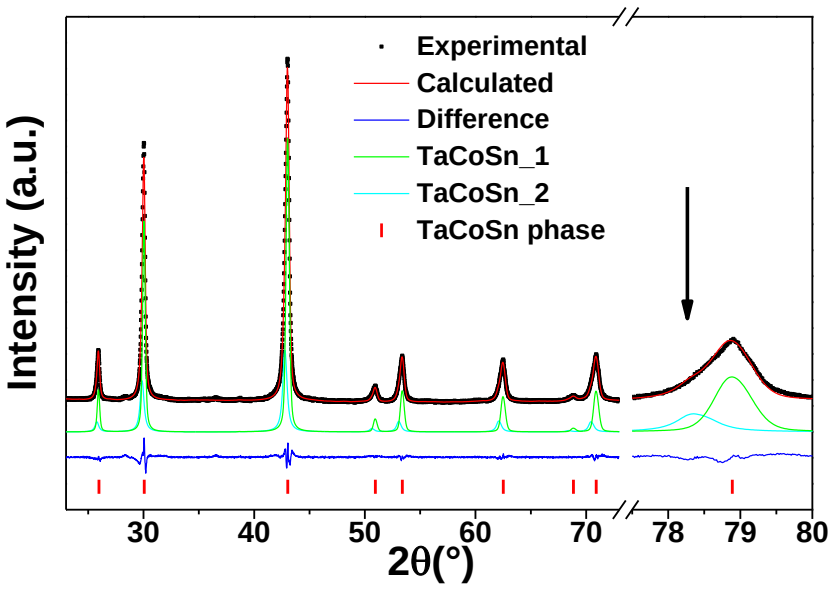

Figure V- 5: XRD pattern of the TaCoSn sample after heat treatment at 973 K.

The magnification of the crystallographic reflection around 79°, corresponding to the half-Heusler TaCoSn, shows a shoulder on the left (indicated by the arrow) that can be fitted by a second TaCoSn phase (TaCoSn_2) with a slightly larger lattice parameter as reported in Table V-1

Table V- 1
Lattice parameter, calculated by Rietveld refinement, of TaCoSn HH phase after heat treatment at different temperatures

Heat treatment (K)	Phase	Lattice parameter (Å)
973	TaCoSn_1	5.945(7)
	TaCoSn_2	5.975(3)
1073	TaCoSn_1	5.937(9)
	TaCoSn_2	5.945(2)
1223 + 973	TaCoSn_1	5.937(4)

In according to the XRD, the back scattered electrons micrograph of the TaCoSn, reported in Figure V- 6, shows uniform grey contrast confirming the presence of TaCoSn single phase. The composition of the phase, calculated from the average of several points obtained through EDS analysis, reported in Table V- 2, shows that the equimolar stoichiometry of the phase is respected.

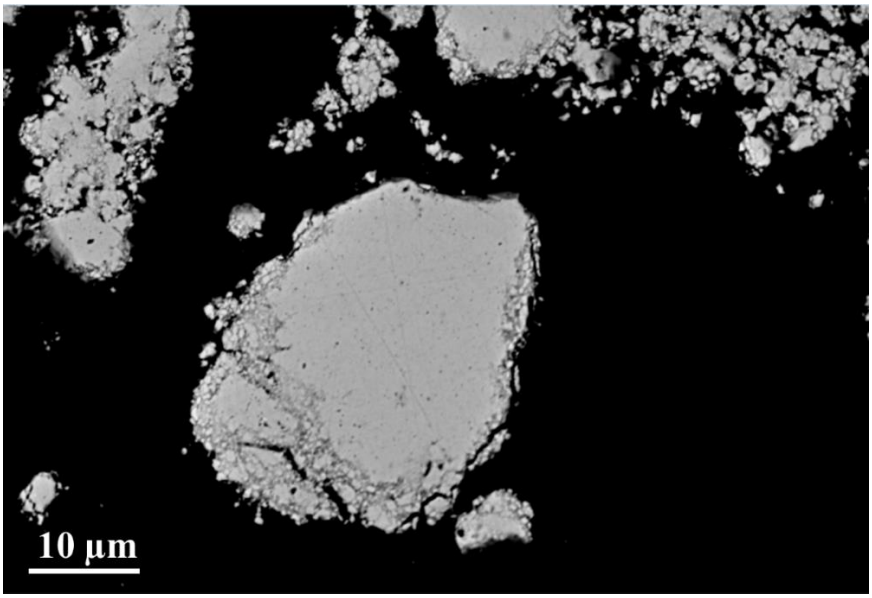

Figure V- 6: Back-scattered electrons micrograph of TaCoSn after annealing at 973 K.

Table V- 2
Composition (at.%) of different phases observed, in TaCoSn after different heat treatments by SEM, obtained using EDS analysis

Heat treatment (K)	**TaCoSn**			**TaCo**		**Sn-rich**	
	Ta	**Co**	**Sn**	**Ta**	**Co**	**Sn**	**Co**
973	32.8	33.0	34.2				
1073	32.7	32.8	34.4				
1223				51.5	48.5	69.3	30.7
1223 & 973	32.5	34.7	32.8	51.2	48.8	72.4	27.6

The kinetics of non-isothermal crystallization of TaCoSn amorphous alloy was investigated by DSC method. Figure V- 7 shows DSC curves for TaCoSn amorphous metallic alloys, obtained at a heating rate of 2, 5, 10, 20 and 40 K min^{-1}.

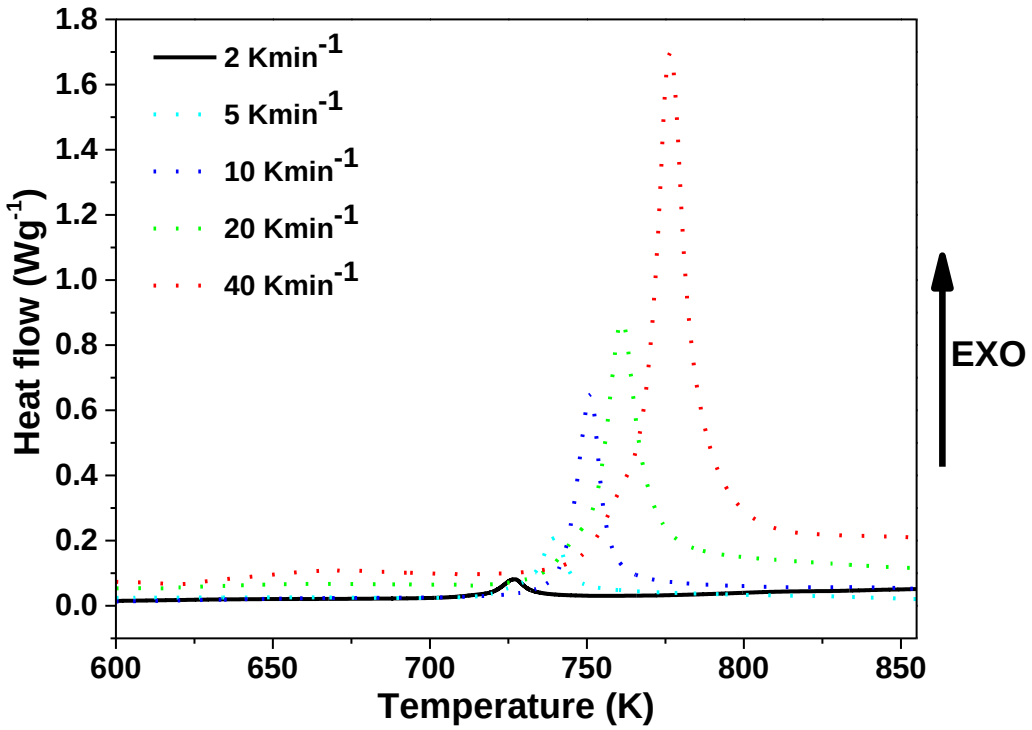

Figure V- 7: DSC traces of TaCoSn for different heating rates (2, 5, 10, 20 and 40 $Kmin^{-1}$) showing crystallization process.

The maximum peak temperatures can be used to calculate the activation energy of crystallization through the Kissinger method[27,28]. This is a non-isothermal method based on the Arrhenius equation, evaluating kinetic parameters from a linear temperature scan measurement. The method uses the Kissinger equation[28], which is expressed as:

$$\ln\frac{\beta}{T_p^2} = \frac{E_a}{RT_p} + \ln\frac{RK_0}{E_a} - \ln g(\alpha) \qquad \text{(V- 1)}$$

where β is the heating rate, T_p is a temperature at which a determined transformed fraction is reached (isokinetic condition), E_a is the activation energy, K_0 is the pre-exponential factor of the Arrhenius equation, R is the gas constant and $g(\alpha)$ is a function. The equation can be reduced to a linear relation with formula: y = -mx + q. In DSC it is typical to use the maximum temperature of the peak as T_p, since the transformation rate at that temperature has reached its maximum. Accordingly, the activation energy can be determined by plotting $\ln \beta/T_p^2$ as a function of $1/T_p$ (Kissinger plot), as shown in Figure V- 8, and performing a linear fit of the points. The value of the activation energy (275 kJmol^{-1}, see Table V- 3), calculated from the resulting slope $m = -E_a/R$, is in the range of those obtained for the crystallization of typical amorphous alloys[26,30].The crystallization heat, ΔH_x, was obtained by the integration of the exothermic peak, as reported in Table V- 3.

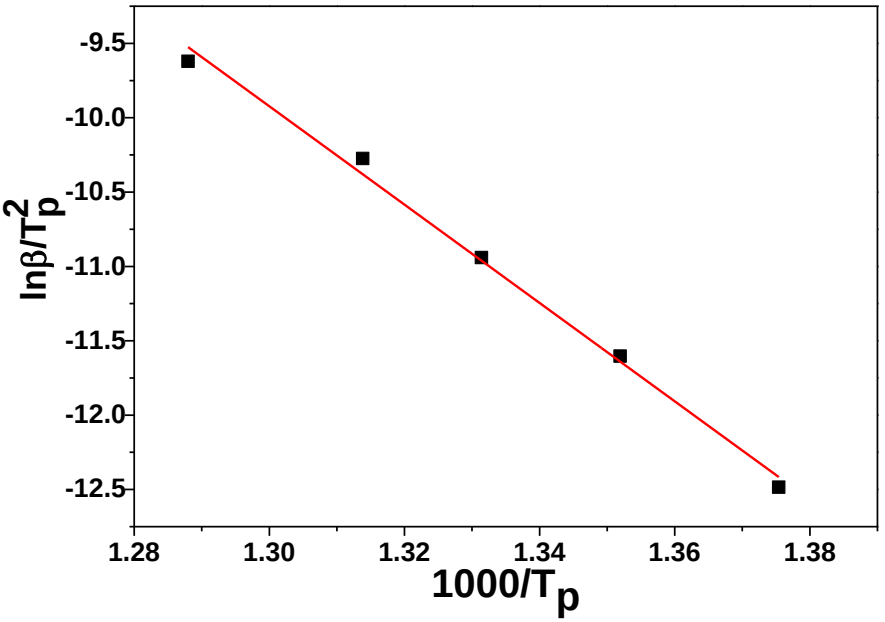

Figure V- 8: Kissinger plot for determination of the activation energy E_a of TaCoSn from a set of DSC scans with different heating rates (2, 5, 10, 20 and 40 $Kmin^{-1}$).

On the basis of the data obtained , is possible to describe the formation of the TaCoSn phase through two steps, mechanical alloying and heat treatment with the scheme reported in *Figure V- 9*. The enthalpy of formation of the TaCoSn HH phase from the pure elements (ΔH_f) can be expressed by the two following contributions: the enthalpy of formation of the amorphous intermediate from the pure elements (ΔH_1) and the enthalpy of crystallization of the amorphous intermediate in the HH phase (ΔH_2). From the thermodynamic point of view, the formation of TaCoSn HH phase directly from the pure elements is equivalent to the formation of TaCoSn HH phase through the amorphous intermediate since $\Delta H_f = \Delta H_1 + \Delta H_2$. However, the formation of the metastable amorphous intermediate by mechanical

alloying of the pure elements is kinetically favoured with respect to the equilibrium HH phase. Subsequently, the thermal energy provided by heat treatment allows to overcome the activation barrier for the crystallization of the metastable amorphous intermediate into the stable HH phase.

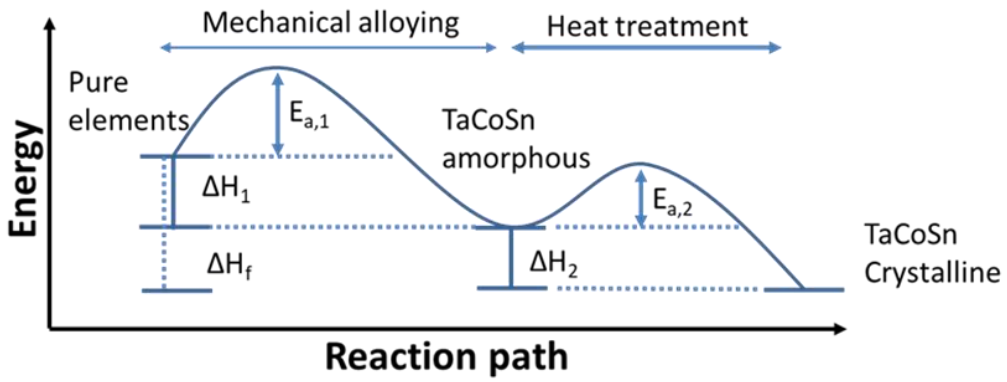

Figure V- 9: Illustration of the reaction path, in two steps, of TaCoSn.

Table V- 3
Activation energy and crystallization enthalpy of TaCoSn

Sample	**Activation energy, $E_{a,2}$ (kJmol^{-1})**	**Crystallization heat, ΔH_2 (kJmol^{-1})**
TaCoSn	275	4.7

5.3.2 Thermal stability of HH TaCoSn

To understand and associate the phase changes that occurs after the peaks observed by HTDSC (Figure V- 4) were performed three heat treatments, at 973 K, 1073 K and 1223 K respectively.

As previously mentioned, the exothermic peak at 753 K is related to the crystallization of the amorphous phase to the crystalline TaCoSn half-Heusler phase. Figure V- 10a shows the XRD pattern of the TaCoSn after heat treatment at 973 K. The crystallographic reflection around 79°, corresponding to the half-Heusler TaCoSn, shows a shoulder on the left (indicated by the arrow) that can be fitted by a second TaCoSn phase (TaCoSn_2). TaCoSn_2 shows a larger lattice parameter (a = 5.9753 Å) than the one of TaCoSn_1 (a = 5.9427 Å), corresponding to the main peak. Figure V- 10b shows the XRD patter of TaCoSn annealed at 1073 K (just after the weak endothermic peak observed in Figure V-4) also in this case, the crystallographic reflection around 79° shows a shoulder (less evident with respect to the previous one) on the left that was fitted using a second TaCoSn phase (TaCoSn_2). Furthermore, from the magnification from 36° to 46° of the patterns shown in Figure V- 10, it is possible to observe that the pattern of the sample annealed at 1073 K the reflections related to the CoTa phase (space group, R-3m), Figure V- 11.

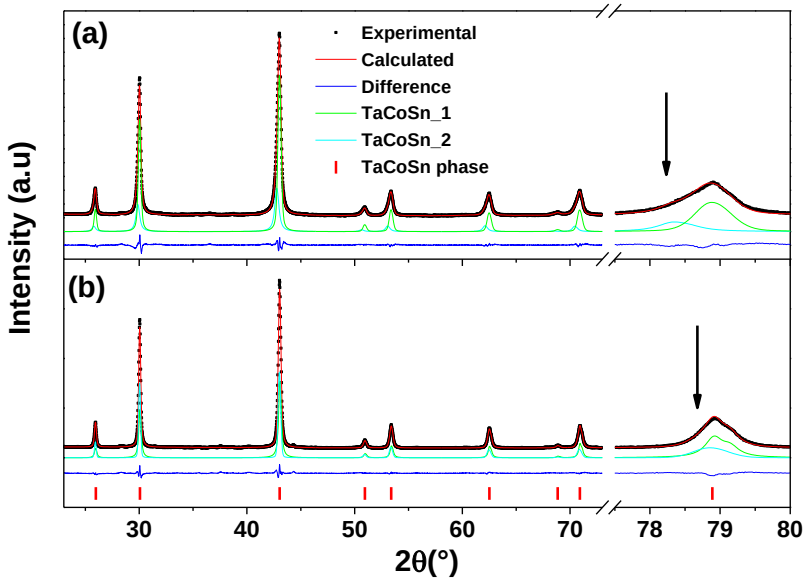

Figure V- 10: XRD pattern of TaCoSn after annealing at 973 K (a) and 1073 K (b)

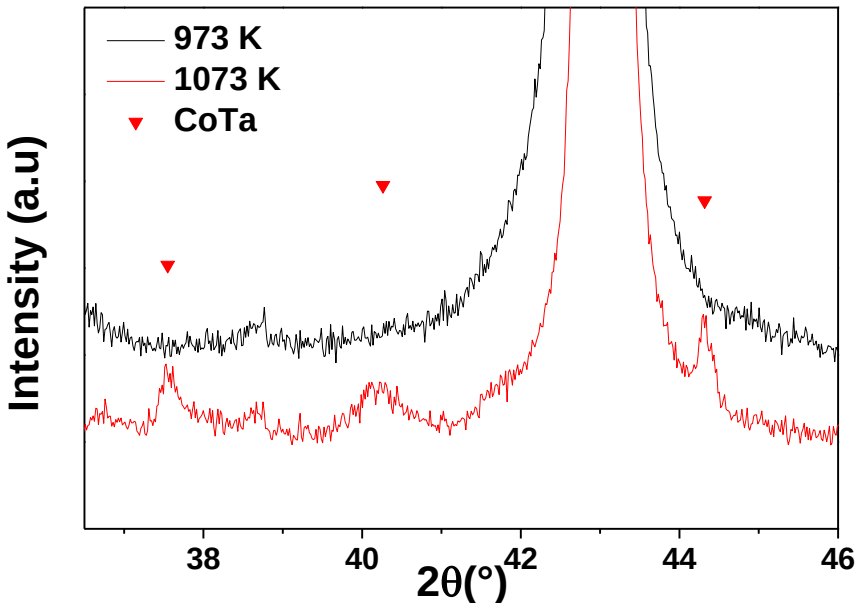

Figure V- 11: Magnification from 36° to 46° of the XRD pattern of TaCoSn annealed at 973 K and 1073 K

The SEM analysis (not reported) did not allow to identify the CoTa phase as it is present in small quantities and¸ likely is finely dispersed. Thus, the first endothermic peak observed in Figure V- 4 can be associated to the phase transition that lead to formation of a small amount of CoTa phase that coexists, in a two phase region, with the remaining HH phase. The change of the lattice parameters of TaCoSn_1 and TaCoSn_2 (table V-1) suggests a compositional variation of the HH phase in accordance with the formation of TaCo. In the XRD pattern of TaCoSn after annealing at 1223 K, displayed in Figure V- 12, the reflections of TaCoSn half-Heusler phase disappear leaving place to the reflections of two phases, TaCo and Sn-rich solid solution, also confirmed from the back-scattered electrons micrograph, shown in Figure V- 13, indicating a decomposition of half-Heusler phase. Thus, the second endothermic peak observed in Figure V- 4 can be associated to a decomposition of the half-Heusler phase.

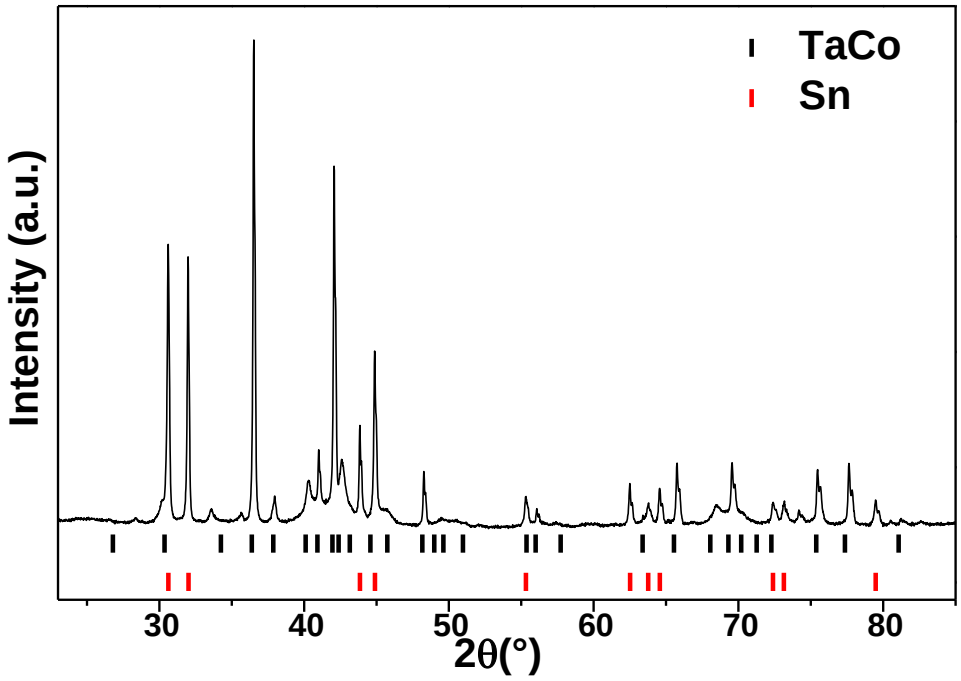

Figure V- 12: XRD pattern of TaCoSn after annealing at 1223 K.

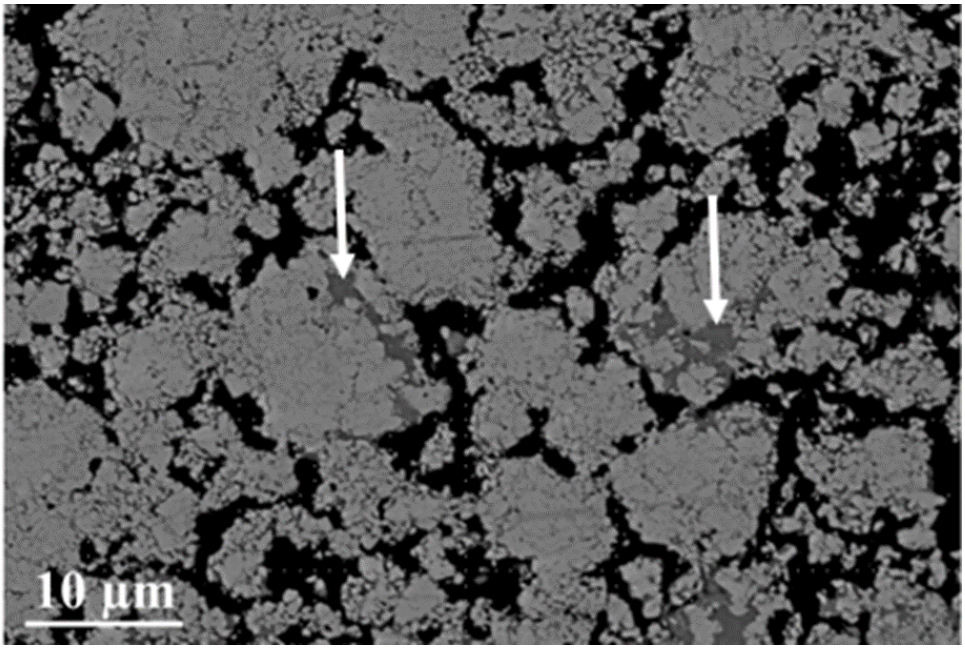

Figure V- 13: Back-scattered electrons micrograph of TaCoSn after annealing at 1223 K: Sn-rich (matrix), TaCo (grey phase indicated with the white arrows)

The TaCoSn powder after annealing at 1223 K was annealed a second time at 973 K for 24 h to study the reversibility of the process. The XRD pattern, reported in Figure V- 14, shows the presence of three phase, TaCoSn half-Heusler phase, TaCo and Sn-rich solid solution, according to the back-scattered electrons micrograph reported in Figure V- 15. The presence of the secondary phase, TaCo and Sn-rich solid solution, is likely due to the slow kinetic of the process that explain the absence of the exothermic peak during the cooling trace obtained by HTDSC (Figure V- 4).

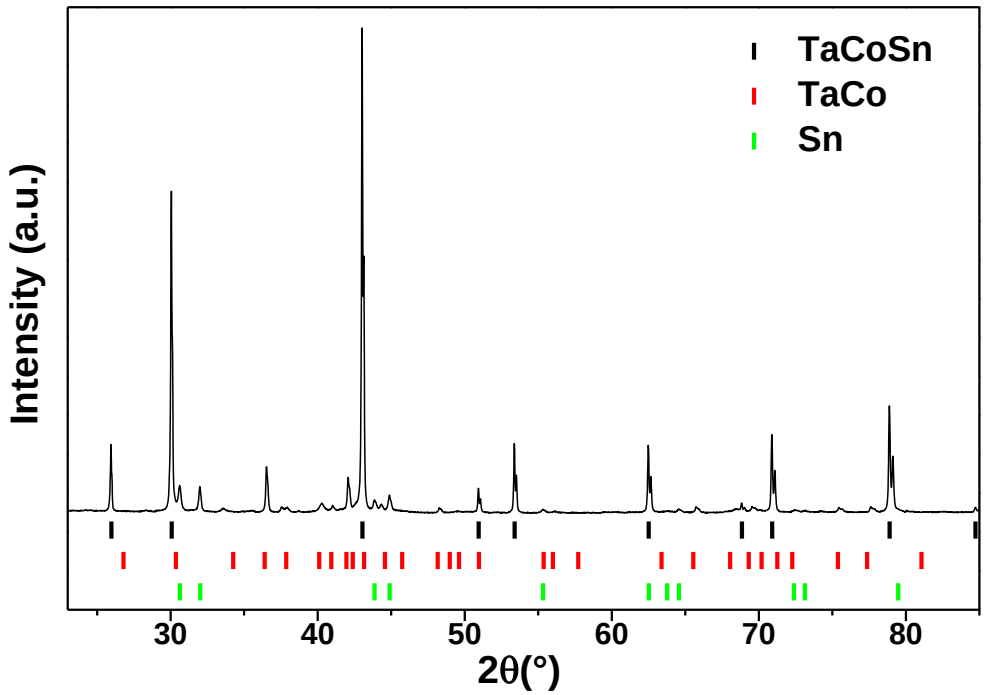

Figure V- 14: XRD pattern of TaCoSn annealed first at 1223 K and then at 973 K for 24 h.

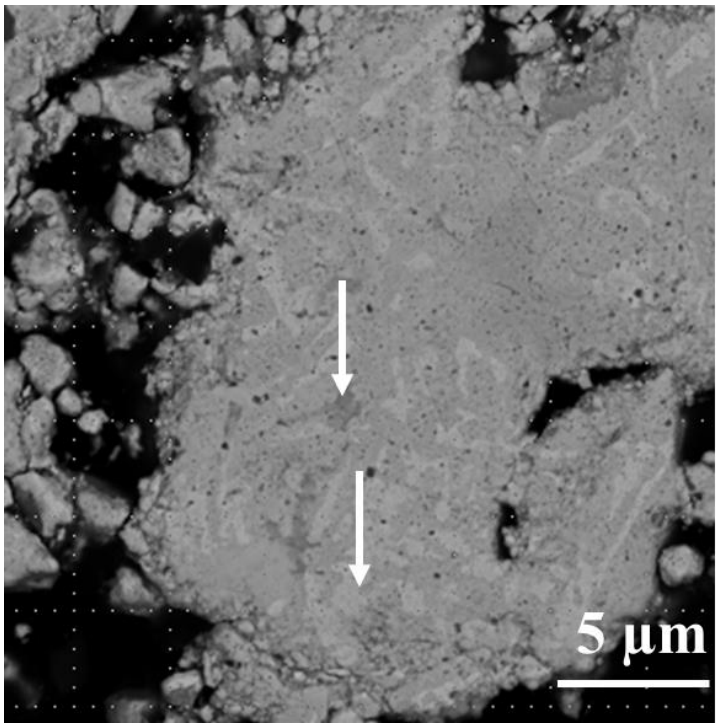

Figure V- 15: Backscattered electron micrograph of TaCoSn annealed first at 1223 K and then at 973 K for 24 h. TaCoSn (matrix) while Sn-rich and TaCo (dark grey and light grey, respectively indicated with the white arrows)

Thus, on the basis of the results obtained it was possible to hypothesize the isopleth TaCo-Sn of the Ta-Co-Sn ternary phase diagram shown in Figure V- 16. For the TaCoSn HH phase a certain compositional range was supposed on the basis of the different lattice parameters estimated by Rietveld analysis of the XRD patterns (Table V-1). When annealing, the weak endothermic peak at 1011 K corresponds to the transition through the solvus line with formation of TaCo that coexists with the remaining TaCoSn which slightly modified its composition, as suggested by the change of the lattice parameter. The second endothermic peak upon annealing (1153 K) can be interpreted as a peritectic reaction where HH-TaCoSn

transforms into TaCo and a Sn-rich liquid. The presence of a peritectic reaction is supported by the fact that the corresponding exothermic peak does not appear upon cooling, as a consequence of the sluggish kinetics of this reaction. However, reversibility of the transformation was verified after annealing at 973 K for 24 h with formation of the HH phase.

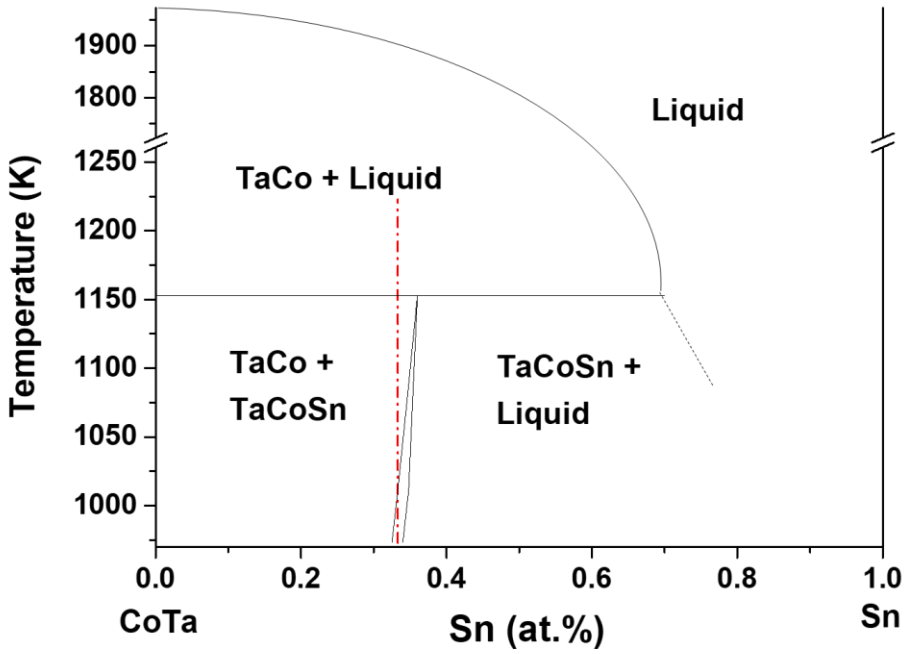

Figure V- 16: hypothetical isopleth of the Ta-Co-Sn phase diagram constructed on the basis of the obtained data.

5.3.2 Sintering

The TaCoSn powder was cold pressed and annealed at 873 K and 973 K for 1 h, obtaining values of relative density of about 60 % and 67 %, respectively. The XRD patterns of the sample sintered at higher

temperature, reported in Figure V- 17, shows only the reflections of TaCoSn half-Heusler phase. The back-scattered electrons micrograph, shown in Figure V- 18, according to the values of density obtained, shows a highly porous sample

The high porosity of the sintered samples can be explained by the use of the cold pressing technique that does not allow to apply pressure levels comparable with those of the hot pressing or other sintering techniques were mechanical and thermal energy are applied simoultaneously

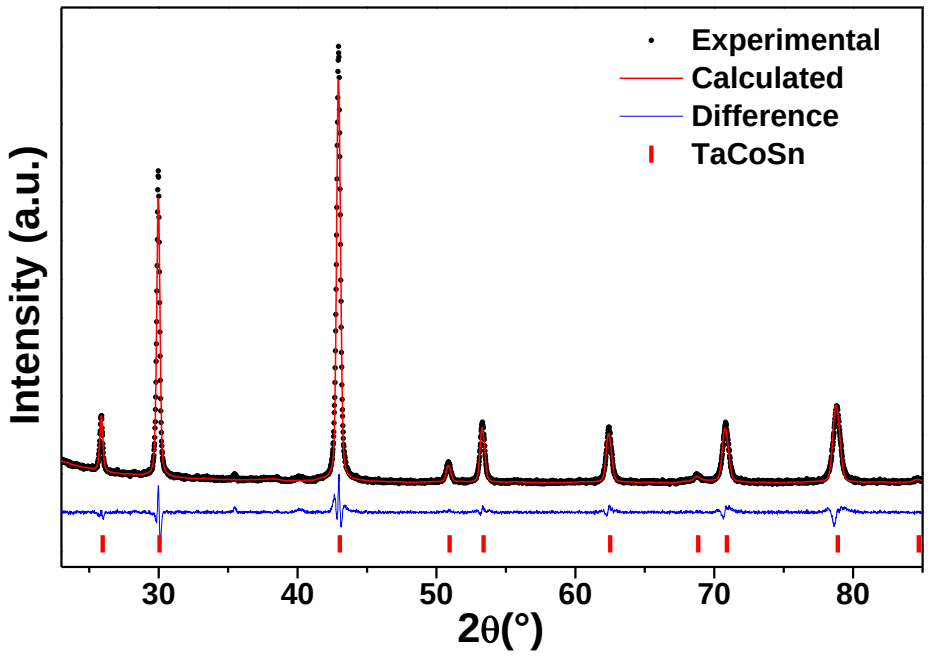

Figure V- 17: XRD pattern of TaCoSn after sintering

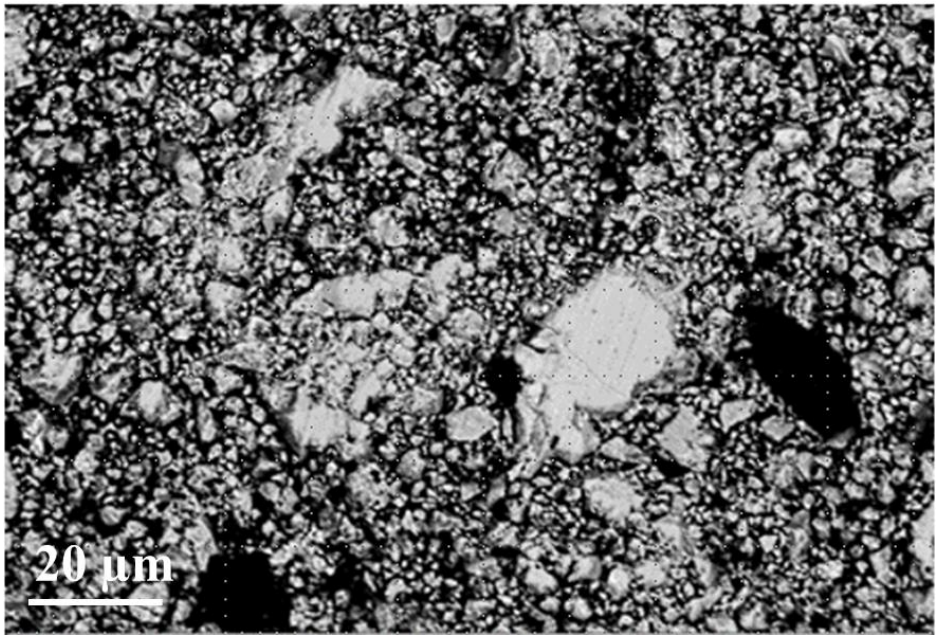

Figure V- 18: Back-scattered electrons micrograph of TaCoSn after sintering

5.3.3 Thermoelectric properties

Figure V- 19 shows the temperature dependence of Seebeck coefficient (α) of the TaCoSn sintered at higher temperature. The Seebeck coefficient of the sample is negative in whole temperature range, indicating that electrons are the majority carriers (n-type). The maximum value obtained is -65 μVK^{-1} at 850 K.

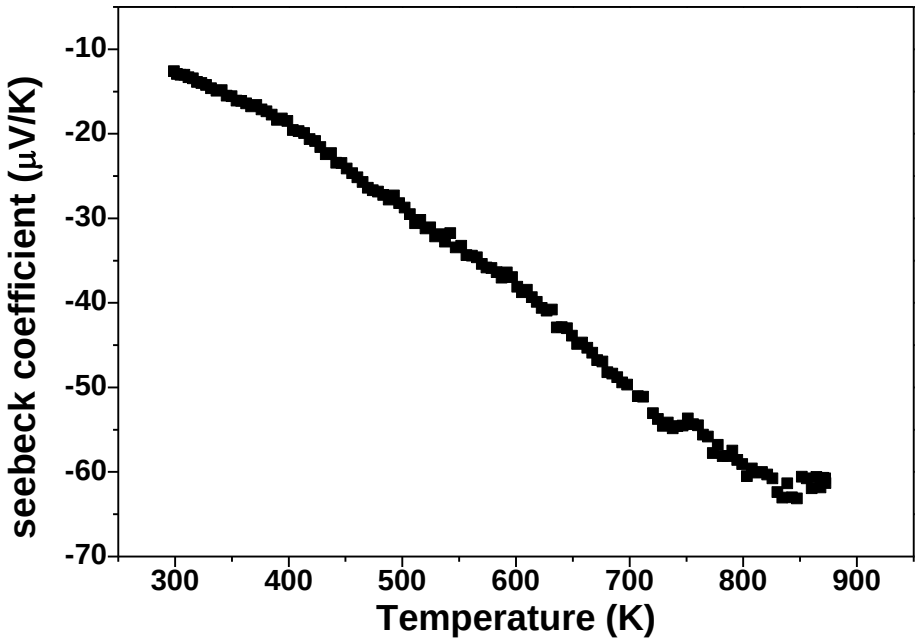

Figure V- 19: Temperature dependence of Seebeck coefficient of TaCoSn

The temperature dependence of electrical conductivity of TaCoSn is reported in Figure V- 20. The low electrical conductivity values obtained are not representative of the electrical conductivity of the TaCoSn compound, since the measurement was performed on a highly porous material.

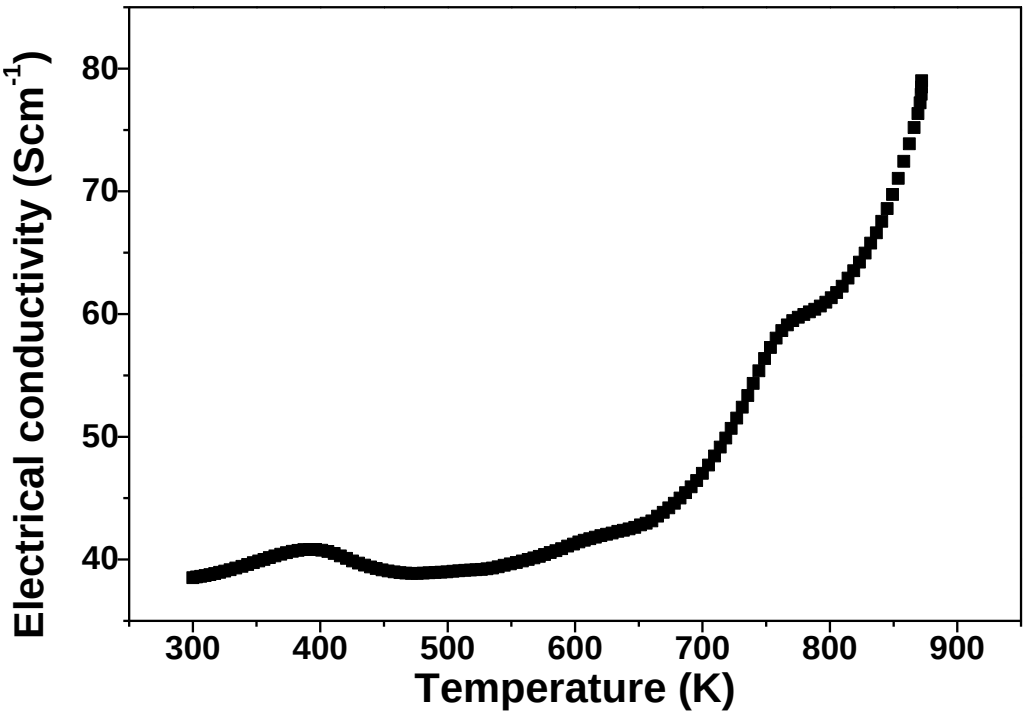

Figure V- 20: Temperature dependence of electrical conductivity of TaCoSn

5.4 Conclusions

In this work, TaCoSn half-Heusler single phase was successfully synthesized by ball-milling and annealing, passing through the formation of an amorphous intermediate. The kinetics of crystallization was studied by DSC, while the thermal stability was studied by HTDSC. The TaCoSn half-Heusler phase is stable up to 1123 K. At the temperature of 1223 K, TaCoSn presents a reversible decomposition process that leads to the formation of two phases, TaCo and Sn-rich. The hypothetical isopleth of Ta-Co-Sn phase diagram was constructed on the basis of the data obtained. Sintering by cold pressing and annealing did not allow to obtain a dense sample,

indicating that other sintering techniques should be used, such as Open die pressing (ODP), Sintering Spark Plasma (SPS) or Hot Pressing. However, for first time the Seebeck coefficient, from room temperature to 870 K, of TaCoSn half-Heusler phase was measured. The low values obtained are probably due to its high concentration of charge carriers. Thus, one of the possibilities to enhance the thermoelectric performance of TaCoSn a doping with Fe that is expected to reduce the carrier concentration, leading to a VEC value slightly lower than 18.

References

1. He, R. *et al.* Achieving high power factor and output power density in p-type half-Heuslers Nb1-xTixFeSb. *Proc. Natl. Acad. Sci. U. S. A.* (2016). doi:10.1073/pnas.1617663113

2. Ren, W. *et al.* Ultrahigh Power Factor in Thermoelectric System Nb 0.95 M 0.05 FeSb (M = Hf, Zr, and Ti). *Adv. Sci.* (2018). doi:10.1002/advs.201800278

3. Zhu, H. *et al.* Discovery of ZrCoBi based half Heuslers with high thermoelectric conversion efficiency. *Nat. Commun.* (2018). doi:10.1038/s41467-018-04958-3

4. Rogl, G. *et al.* Mechanical properties of half-Heusler alloys. *Acta Mater.* (2016). doi:10.1016/j.actamat.2016.01.031

5. Yan, X. *et al.* Thermoelectric property study of nanostructured p-type half-heuslers (Hf, Zr, Ti)CoSb0.8 Sn0.2. *Adv. Energy Mater.* (2013). doi:10.1002/aenm.201200973

6. He, R. *et al.* Investigating the thermoelectric properties of p-type half-Heusler Hfx(ZrTi)1-xCoSb0.8Sn0.2 by reducing Hf concentration for power generation. *RSC Adv.* (2015). doi:10.1039/c4ra14343d

7. Joshi, G. *et al.* NbFeSb-based p-type half-Heuslers for power generation applications. *Energy Environ. Sci.* (2014). doi:10.1039/c4ee02180k

8. Fu, C. *et al.* Realizing high figure of merit in heavy-band p-type half-Heusler thermoelectric materials. *Nat. Commun.* (2015). doi:10.1038/ncomms9144

9. Yu, J. *et al.* Unique Role of Refractory Ta Alloying in Enhancing the Figure of Merit of NbFeSb Thermoelectric Materials. *Adv. Energy Mater.* (2018). doi:10.1002/aenm.201701313

10. Shen, J., Fu, C., Liu, Y., Zhao, X. & Zhu, T. Enhancing thermoelectric performance of FeNbSb half-Heusler compound by Hf-Ti dual-doping. *Energy Storage Mater.* (2018). doi:10.1016/j.ensm.2017.07.014

11. Hu, C., Xia, K., Chen, X., Zhao, X. & Zhu, T. Transport mechanisms and property optimization of p-type (Zr, Hf)CoSb half-Heusler thermoelectric materials. *Mater. Today Phys.* (2018). doi:10.1016/j.mtphys.2018.11.002

12. Zhu, H. *et al.* Discovery of TaFeSb-based half-Heuslers with high thermoelectric performance. *Nat. Commun.* (2019). doi:10.1038/s41467-018-08223-5

13. Joshi, G. *et al.* Enhancement in thermoelectric figure-of-merit of an N-type half-Heusler compound by the nanocomposite approach. *Adv. Energy Mater.* (2011). doi:10.1002/aenm.201100126

14. Xie, H. *et al.* The intrinsic disorder related alloy scattering in ZrNiSn half-Heusler thermoelectric materials. *Sci. Rep.* (2014). doi:10.1038/srep06888

15. Gautier, R. *et al.* Prediction and accelerated laboratory discovery of previously unknown 18-electron ABX compounds. *Nat. Chem.* (2015). doi:10.1038/nchem.2207

16. Joint Committee on Powder Diffraction Standards. *Index to powder Diffr. file* (1972).

17. FIZ Karlsruhe. FIZ Karlsruhe. *Inorganic Crystal Structure Database* (2006).

18. Villars, P. & Calvert, L. D. Pearson's Handbook of Crystallographic Data for Intermetallic Phases. *ASM Int.* (1991).

19. Hohl, H. *et al.* New compounds with MgAgAs-type structure: NbIrSn and NbIrSb. *J. Phys. Condens. Matter* (1998). doi:10.1088/0953-8984/10/35/016

20. Haase, M. G., Schmidt, T., Richter, C. G., Block, H. & Jeitschko, W. Equiatomic rare earth (Ln) transition metal antimonides LnTSb (T=Rh, Ir) and bismuthides LnTBi (T=Rh, Ni, Pd, Pt). *J. Solid State Chem.* (2002). doi:10.1006/jssc.2002.9670

21. Casper, F., Seshadri, R. & Felser, C. Semiconducting half-Heusler and LiGaGe structure type compounds. *Phys. Status Solidi Appl. Mater. Sci.* (2009). doi:10.1002/pssa.200881223

22. Zakutayev, A. *et al.* Theoretical prediction and experimental realization of new stable inorganic materials using the inverse design approach. *J. Am. Chem. Soc.* (2013). doi:10.1021/ja311599g

23. Wei, J. & Wang, G. Thermoelectric and optical properties of half-Heusler compound TaCoSn: A first-principle study. *J. Alloys Compd.* (2018). doi:10.1016/j.jallcom.2018.05.037

24. Haque, E. & Hossain, M. A. First-principles study of elastic, electronic, thermodynamic, and thermoelectric transport properties of TaCoSn. *Results Phys.* (2018). doi:10.1016/j.rinp.2018.06.053

25. Lutterotti, L., S. Matthies, and H. R. W. MAUD: a friendly Java program for material analysis using diffraction. *IUCr Newsl. CPD* **21**, 14–15 (1999).

26. Boldrini, S. *et al.* Test rig for high-temperature thermopower and electrical conductivity measurements. *J. Electron. Mater.* (2013). doi:10.1007/s11664-012-2437-3

27. Castellero, A., Lussana, D., Ripamonti, D., Angella, G. & Baricco, M. Cold rolling of amorphous/crystalline Ag73.2Cu17.1Zr9.7 composite. *J. Alloys Compd.* (2014). doi:10.1016/j.jallcom.2013.11.103

28. Kissinger, H. E. Reaction Kinetics in Differential Thermal Analysis. *Anal. Chem.* (1957). doi:10.1021/ac60131a045

29. Song, K. K. *et al.* Thermal stability and mechanical properties of Cu 46Zr 46Ag 8 bulk metallic glass and its composites. *Mater. Sci. Eng. A* (2013). doi:10.1016/j.msea.2012.09.013

CHAPTER VI:

SYNTHESIS AND THERMOELECTRIC PROPERTIES OF METALLIC ULLMANNITES

6.1 Introduction and aim of work

The investigation of new classes of materials is one of the promising approaches for future research and development of the field of thermoelectrics. There are vast opportunities for discovery of new compounds with good thermoelectric properties in chemistry. For example, many possible inorganic materials that consist of three or more elements are still missing from published resources. The synthesis of missed inorganic materials for example can be guided by predictive theoretical first-principles calculations that sort stable versus unstable compounds [1]. Another approach to discover new materials with good thermoelectric performance is to study their band structure. As reported in literature [2] using the Boltzman's equation approach the Seebeck coefficient is given as

$$\alpha = \frac{1}{eT} k_0^{-1} k_1 \qquad \text{(VI- 1)}$$

where e is the electron charge, T is the temperature, tensors k_0 and k_1 are given by

$$k_n = \sum_k \tau(k)\upsilon(k)\upsilon(k)\left[\frac{-\partial f(\varepsilon)}{\partial \varepsilon}(k)\right](\varepsilon(k)-\mu)^n \qquad \text{(VI- 2)}$$

where $\varepsilon(k)$is the band dispersion, $\upsilon(k)$ is the group velocity, $\tau(k)$ is quasiparticle lifetime, $f(\varepsilon)$ is the Fermi distribution function and μ is the chemical potential. Using k_0, electrical conductivity is given as

$$\sigma = e^2 k_0 \qquad \text{(VI- 3)}$$

Thus, the Seebeck coefficient and electrical conductivity are directly proportional to k_1 and k_0, respectively. k_0 and k_1 depend on ν_A and ν_B, that are the velocities for the states above and below μ respectively.

$$\alpha \propto \frac{\upsilon_A^2 - \upsilon_B^2}{\upsilon_A^2 + \upsilon_B^2} \qquad \text{(VI- 4)}$$

$$\sigma \propto \upsilon_A^2 + \upsilon_B^2 \qquad \text{(VI- 5)}$$

Figure VI- 1 shows the band structure of usual metals where $\upsilon_A \sim \upsilon_B$. Thus, the numerator in equation VI- 4 is around 0, resulting in a small Seebeck coefficient.

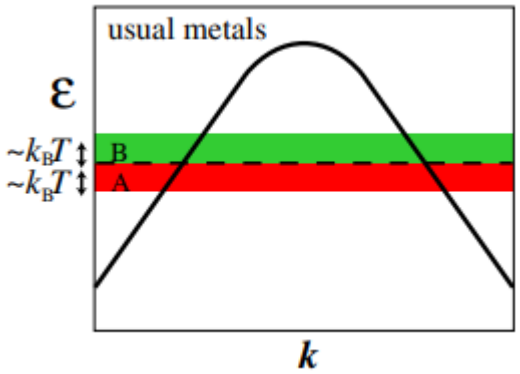

Figure VI- 1: band structure of usual metals[2]

Instead, considering an ideal band structure that has a somewhat flat portion called "Pudding mold", as shown in Figure VI- 2, where $\upsilon_A \gg \upsilon_B$ resulting in a high Seebeck coefficient and high electrical conductivity.

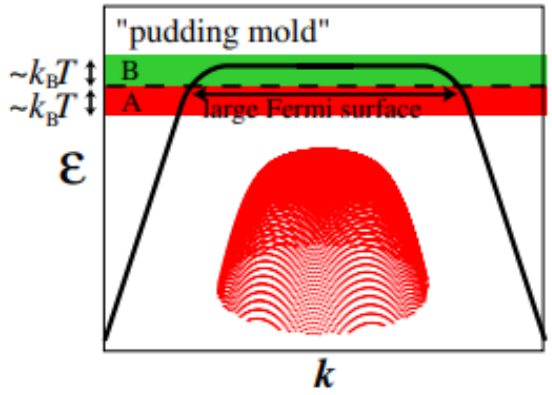

Figure VI- 2: s*chematic figure for the pudding mold band*[2]

Recently a new family of compounds, still little studied, called ullmannites are attracting large interest as promising new candidates for thermoelectric applications[3]. Ullmannite are equiatomic ternary compounds with general formula TPnCh, where T is a 9 or 10 group element, Pn is a pnictogen and Ch is a chalcogen. If T is an element of 9 group, with d^6 configuration, the compound shows semiconductor behaviour, if T is an element of 10 group, with d^7 configuration, the compound shows metallic behaviour[3,4]. The structure belongs to the FeS_2 pyrite family, resulting from the substitution of S_2 groups in pyrite structure by PnCh in the ullmannite structure. This replacement leads to a sizeable shifting of T atom along the body diagonal direction of the cube structure: in this arrangement T results surrounded by three Pn atoms and three Ch atoms that form an octahedron, as shown in Figure VI- 3[5–9].

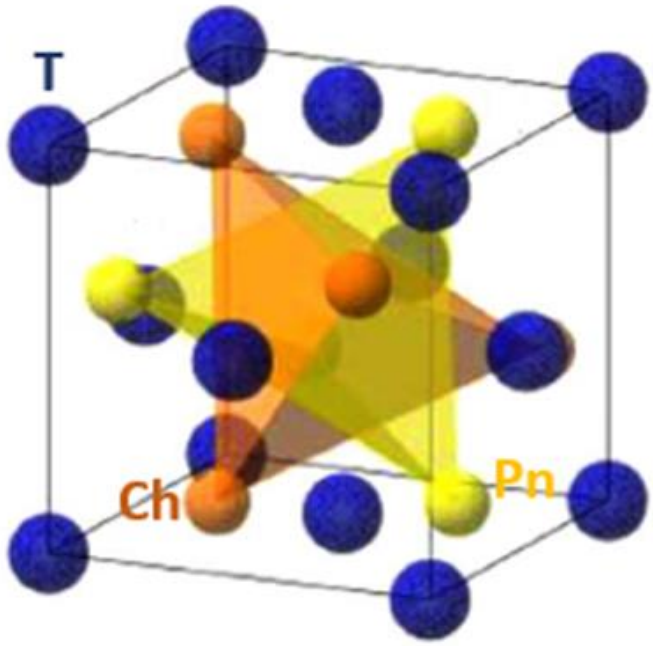

Figure VI- 3: Crystal structure of Ullmannite compounds[10]

NiSbS and other ullmannite conductors have been synthesized, but the thermoelectric properties at high temperature have never been measured [4,9]. The aim of this work was to calculate the thermodynamic stability of four different ullmannites (NiSbS, NiSbSe, PdSbS and PdSbSe) by ab-initio calculation and synthesize them in order to measure, for the first time, the thermoelectric properties at high temperature in order to correlate the thermoelectric properties, in particular the Seebeck coefficient, with the differences in their band structure.

6.2 Experimental

Polycrystalline samples of NiSbS, NiSbSe and PdSbSe, were synthesized by melting pure elements. In the case of PdSbS, the synthesis was conducted by solid state reaction because of impossibility of obtaining the phase by melting the pure elements. Powder elements Ni (3N), Pd (3N), Sb (3N) and Se (3N) were mixed in stoichiometric quantities. The mixture was sealed in an evacuated quartz ampoule. The synthesis conditions used for each sample are reported in Figure VI- 4. Thermodynamic stability of the ullmannites phases was calculated by ab-initio calculation using Crystal-program[12]. Crystal characterization was performed by Powder X-Ray diffraction (PXRD) measurements using a Rigaku, miniflex diffractometer with Cu-K_α radiation. Rietveld analysis was performed using MAUD software[13]. The thermoelectric properties were measured in the temperature range from room temperature to 773 K. The electrical resistivity, σ, and Seebeck coefficient, α, were measured simultaneously using Ulvac ZEM-3 in Helium atmosphere. The Seebeck coefficient was measured in the temperature gradient 20, 30 and 40 K. The relative error of α and σ was estimated to around 5%.

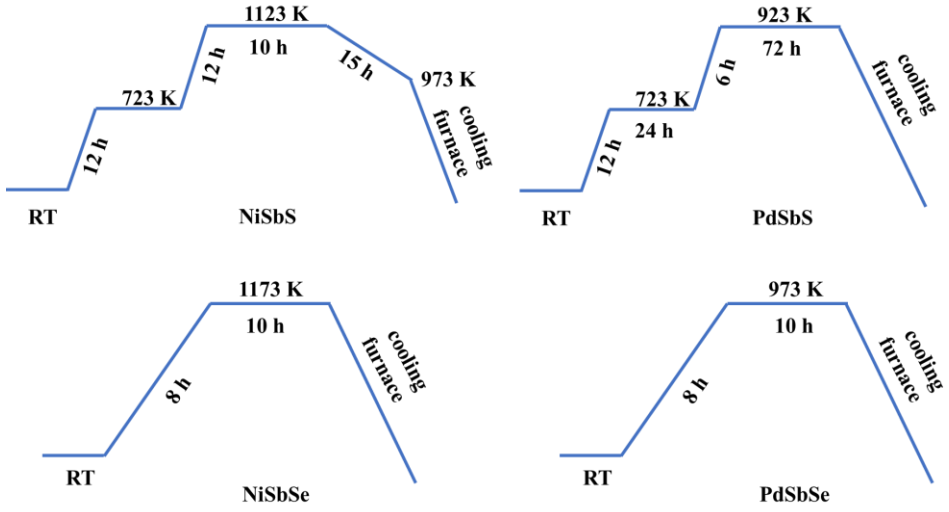

Figure VI- 4: synthesis conditions used to synthesize NiSbS, PdSbS, NiSbSe and PdSbSe

6.3 Results

6.3.1 Stability of ullmannites phase relative to binary phases

The thermodynamic phase stability of the various ullmannites was calculated ab-initio by Prof. Lorenzo Maschio and coworkers (University of Turin, Department of Chemistry) by means of CRYSTAL code[12]. According to this purpose, the following reactions in standard conditions (pressure and temperature) were considered where the ternary phases (ullmannites) form from binary phases:

$$NiSb_2 + NiS_2 \rightarrow 2NiSbS$$

$$NiSe_2 + NiSb_2 \rightarrow 2NiSbSe$$

$$PdSb_2 + PdS_2 \rightarrow 2PdSbS$$

$$PdSb_2 + PdSe_2 \rightarrow 2PdSbSe$$

As shown in Table VI- 1, all ullmannites phases showed negative values of the enthalpy of formation (ΔH_f) and Gibbs free energy of formation (ΔG_f), indicating the thermodynamic stability of the ullmannites phases under examination.

Despite the thermodynamic stability of all the four ullmannites considered, only NiSbS, NiSbSe and PdSbSe could be obtained by melt processing. In the case of NiSbS, DTA traces [3] show a congruent melting of the ternary compound, indicating that the ullmannite phase directly forms by solidification of the melt. A similar behaviour can be supposed for NiSbSe and PdSbSe. In the case of PdSbS, the ullmanite ternary compound could not be obtained by melt processing, suggesting a more complex solidification path that is currently under investigation.

Table VI- 1
Enthalpy and Gibbs free energy of formation of NiSbS, PdSbS, NiSbSe and PdSbSe calculated ab-initio using Crystal code.

Sample	**ΔH°_f(kJmol^{-1})**	**ΔG°_f(kJmol^{-1})**
NiSbS	-246.4	-256.2
PdSbS	-279.9	-274.8
NiSbSe	-224.6	-232.8
PdSbSe	-292.8	-287.0

6.3.2 Structural characterization

Figure VI- 5 shows the XRD pattern of NiSbS, PdSbS, NiSbSe and PdSbSe. For the all samples, the diffraction pattern can be fitted assuming ullmannite structure with $P2_13$ symmetry. Every sample

shows only the reflections of ullmannite phase, except for the sample NiSbSe that it shows additional peaks attributable to a small amount of NiSb secondary phase. The relative amount of the phases and the corresponding lattice parameters, obtained by Rietveld refinement of the XRD pattern of Figure VI- 5 are reported in Table VI- 2 and are in good agreement with those reported in literature [5].

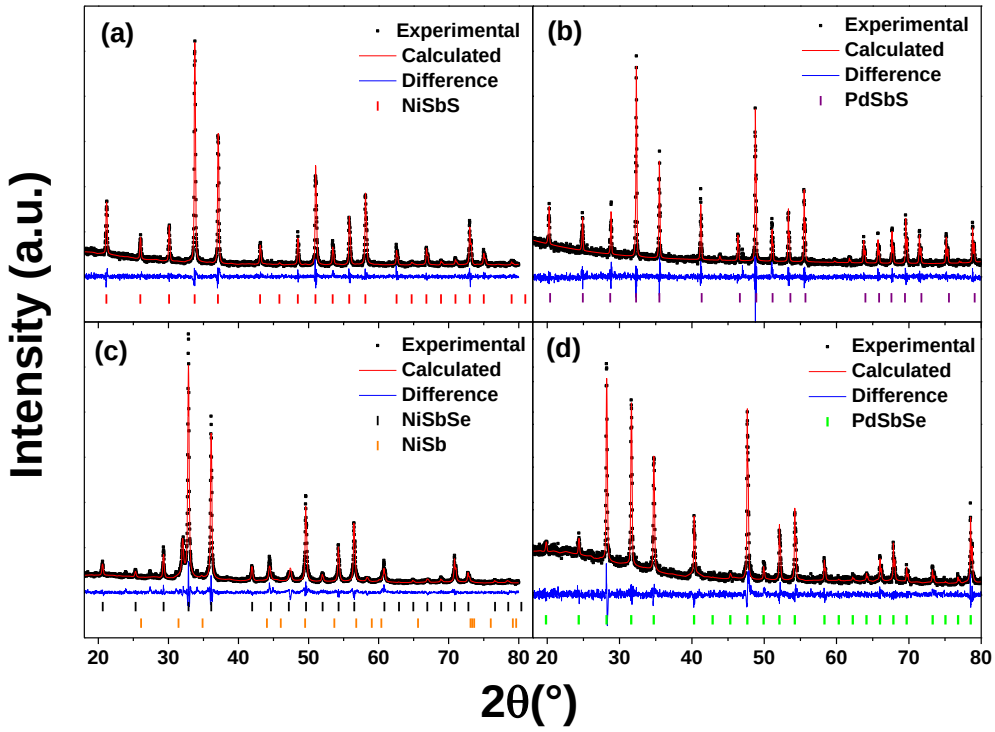

Figure VI- 5: X-ray diffraction pattern of the samples (a) NiSbS, (b) PdSbS, (c) NiSbSe and (d) PdSbSe

Table VI- 2
Lattice parameter and relative amount of the phases, performed by Rietveld refinement using Maud

Sample	Lattice parameter (Å)	Phases (wt. %)
NiSbS	5.933(9)	NiSbS
PdSbS	6.186(4)	PdSbS
NiSbSe	6.092(1)	NiSbSe (90), NiSb (10)
PdSbSe	6.323(7)	PdSbSe

6.3.3 Thermoelectric characterization

The temperature dependence of the NiSbS, NiSbSe and PdSbSe are reported in *Figure VI- 6*. The thermoelectric properties of the PdSbS sample could not be measured since it was not possible to obtain a dense material by the solid state reaction. The temperature dependence of Seebeck coefficient for the sample above cited is presented in Figure VI- 6a. For NiSbS, the values of Seebeck coeffient are negative in entire temperature range explored, which indicates that the NiSbS is an n-type TE material. The values are larger (from -23 μVK^{-1}at 334 K to -21 μVK^{-1} at 761 K) with respect to the others two samples studied (NiSbSe and PdSbSe). The temperature dependence of electrical resistivity are reported in Figure VI- 6b. For the all samples the electrical resistivity increases linearly with the temperature, indicating a typical metallic behaviour. The NiSbS sample shows an electrical resistivity lower than that of the others two samples in the entire range of temperature considered. The temperature dependence of the power factor is shown in Figure VI-

6c. The power factor for NiSbS is about 1.3 $mWm^{-1}K^{-2}$ at 334 K. This value is larger than that of the sulfide materials with high thermoelectric performance, such as tetrahedrites (PF= 1.2 $mWK^{-2}m^{-1}$ at 665 K, or PF~0.9 $mWK^{-2}\cdot m^{-1}$ at 700 K) [12,13] or colusites (PF= 0.61 $mWK^{-2}\cdot m^{-1}$at 663 K) [16]. The observed behaviour results from the low electrical resistivity, typical of metallic materials, and the Seebeck coefficient, that shows unusually large values for a metallic system such as NiSbS.

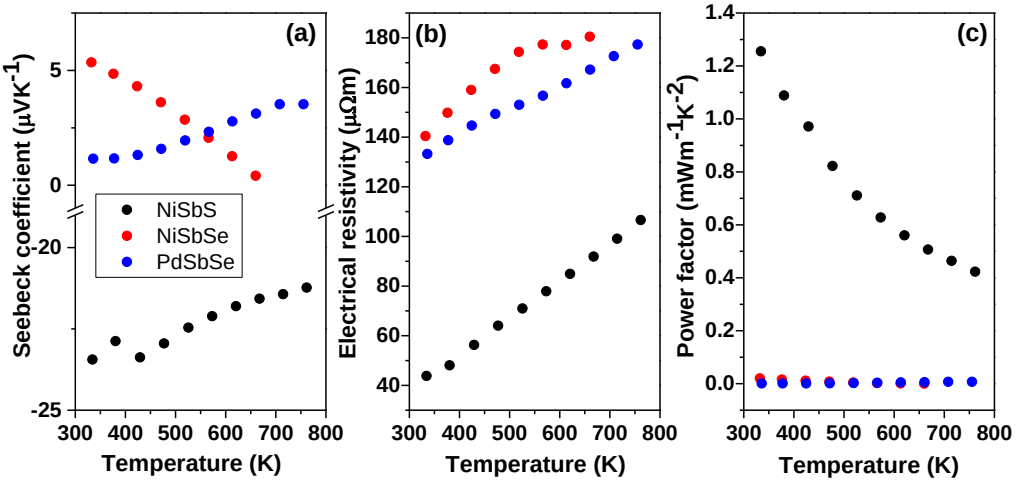

Figure VI- 6: The temperature dependence of Seebeck coefficient (a), electrical resistivity (b) and power factor (c) for the NiSbS, NiSbSe and PdSbSe samples

To explain the unusual thermoelectric properties of the metallic NiSbS ternary compound, the band structure and the density of states (DOS) of the NiSbS, NiSbSe and PdSbSe ullmannites, Figure VI-7, were calculated ab-initio by Lorenzo Maschio and coworkers using CRYSTAL code. For all the three compounds, there is not evidence

of a band gap, in agreement with the metallic behaviour observed experimentally.

The three compounds show similar band structures with small differences. The attention should be focused on the band along the Γ-R direction, that is highlighted by the circle in Figure VI-7, and its intersection with the Fermi level. In the case of NiSbS, the band dispersion near E_F along the Γ-R direction leads to $\upsilon_A \gg \upsilon_B$, and consequently to a larger value of the Seebeck coefficient with respect to NiSbSe and PdSbSe, despite the metallic nature of this compound. The combination of the large values of the Seebeck coefficient and electrical conductivity in NiSbS ensures a reasonable large value of the power factor for this metallic thermoelectric compound.

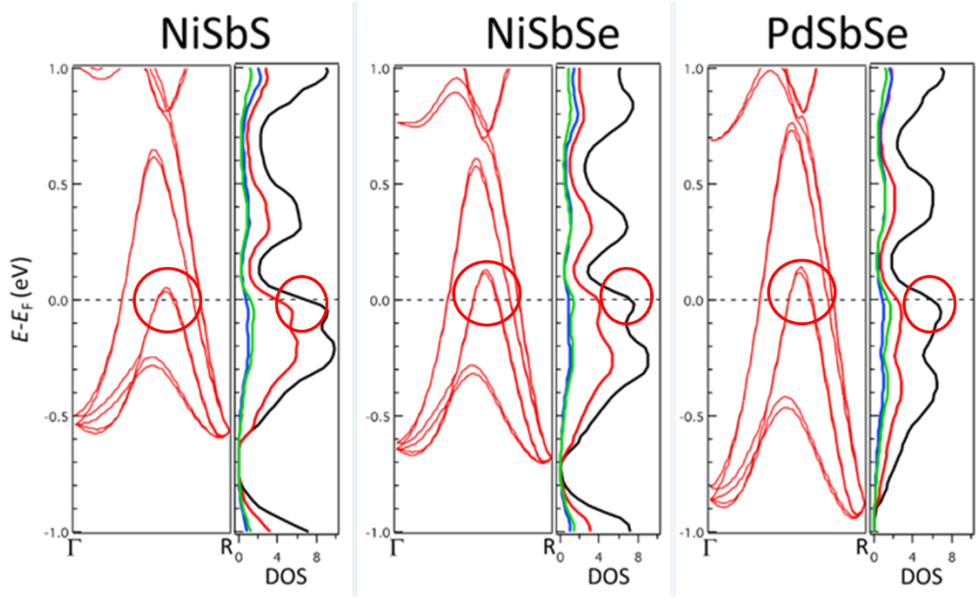

Figure VI- 7: Comparison of band dispersion of NiSbS, NiSbSe and PdSbSe near E_F along Γ-R direction(highlighted by the red circle)

6.4 Conclusions

The thermodynamic stability of four ullmannite compounds (NiSbS, NiSbSe, PdSbSe, PdSbS) was confirmed by ab-initio calculations using Crystal code. NiSbS, NiSbSe and PdSbSe were successfully synthesized by melting pure elements, except PdSbS that had to be synthesized by solid state reaction, probably due to a complex solidification path. For the first time the thermoelectric properties at high temperature for ullmannites compounds was measured. The NiSbS, shows a large Seebeck coefficient and a small electrical resistivity, resulting in a large power factor about 1.3 $mWm^{-1}K^{-2}$, comparable with others thermoelectric materials. The key of higher Seebeck coefficient and lower electrical resistivity of the NiSbS sample is due to different band dispersion near E_F along Γ-R direction.

References

1. Zakutayev, A. *et al.* Theoretical prediction and experimental realization of new stable inorganic materials using the inverse design approach. *J. Am. Chem. Soc.* (2013). doi:10.1021/ja311599g

2. Kuroki, K. & Arita, R. ‘Pudding mold’ band drives large thermopower in Na xCoO2. *J. Phys. Soc. Japan* (2007). doi:10.1143/JPSJ.76.083707

3. Carlini, R., Zanicchi, G., Borzone, G., Parodi, N. & Costa, G. A. Synthesis and characterization of the intermetallic compound NiSbS. in *Journal of Thermal Analysis and Calorimetry* (2012). doi:10.1007/s10973-012-2192-y

4. Foecker, A. J. & Jeitschko, W. The atomic order of the pnictogen and chalcogen atoms in equiatomic ternary compounds TPnCh (T = Ni, Pd; Pn = P, As, Sb; Ch = S, Se, Te). *J. Solid State Chem.* (2001). doi:10.1006/jssc.2001.9342

5. Hulliger, F. New compounds with cobaltite structure. *Nature* (1963). doi:10.1038/198382b0

6. Bayliss, P. SUBDIVISION OF THE PYRITE GROUP, AND ACHEMICAL AND X.RAY-DIFFRACTION INVESTIGATION OF ULLMANNITE. **33**, 27–33 (1986).

7. BAYLISS P. ISOMORPHOUS SUBSTITUTION IN SYNTHETIC COBALTITE AND ULLMANNITE. *Am. Mineral.* (1969).

8. Palache, C., Berman, H., Frondel, C. & Evans, B. S. The system of mineralogy of james dwight dana and edward salisbury dana. *The Analyst* (1946). doi:10.1039/an9467100343

9. Tacheuchi Yoshio. THE ABSOLUTE STRUCTURE OF ULLMANITE, NiSbS. *Mineral. J.* **2**, 90–102 (1957).

10. Kakihana, M. *et al.* Split Fermi surface properties in ullmannite NiSbS and PdBiSe with the cubic chiral crystal structure. *J. Phys. Soc. Japan* (2015). doi:10.7566/JPSJ.84.094711

11. Miyata, M., Ozaki, T., Nishino, S. & Koyano, M. Thermoelectric properties of high power factor sulfide NiSbS and Co substitution system Ni1-xCoxSbS. *Jpn. J. Appl. Phys.* (2017). doi:10.7567/JJAP.56.021801

12. Dovesi, R. *et al.* Quantum-mechanical condensed matter simulations with CRYSTAL. *Wiley Interdiscip. Rev. Comput. Mol. Sci.* (2018). doi:10.1002/wcms.1360

13. Lutterotti, L., S. Matthies, and H. R. W. MAUD: a friendly Java program for material analysis using diffraction. *IUCr Newsl. CPD* **21**, 14–15 (1999).

14. Suekuni, K. *et al.* High-performance thermoelectric mineral Cu12-xNi xSb4S13 tetrahedrite. *J. Appl. Phys.* (2013). doi:10.1063/1.4789389

15. Lu, X. *et al.* High performance thermoelectricity in earth-abundant compounds based on natural mineral tetrahedrites. *Adv. Energy Mater.* (2013). doi:10.1002/aenm.201200650

16. Suekuni, K. *et al.* High-performance thermoelectric minerals: Colusites Cu26V2M6S32 (M = Ge, Sn). *Appl. Phys. Lett.* (2014). doi:10.1063/1.4896998

CHAPTER VII: CONCLUSIONS

In this thesis, I focused my work on the experimental optimization and development of selected thermoelectric intermetallic compounds for waste heat harvesting. On the one hand, I studied the effect of rapid solidification on the structural, microstructural and thermoelectric properties of Yb-filled $CoSb_3$ skutterudite and TiNiSn half Heusler alloy. On the other hand, I studied the synthesis and the properties of "novel" intermetallic compounds, such as TaCoSn half Heusler alloy and (Ni,Pd)Sb(S,Se) ullmannites, that so far were never considered for thermoelectric applications.

Yb-filled $CoSb_3$ skutterudite and TiNiSn half Heusler alloy present, upon solidification, peritectic reactions that require long distance diffusion path and, consequently, long heat treatments for homogenizing the alloys. It was shown that rapid solidification is a suitable intermediate step for shortening the total processing time to obtain dense and single phase samples.

In rapidly solidified Yb-filled $CoSb_3$ skutterudite, the fine microstructure obtained by rapid solidification favours grain boundary diffusion allowing, upon annealing, a faster homogenization of the alloy with respect to the cast ingot.

Rapid solidification of TiNiSn by planar flow casting favours undercooling of the melt. As the copper wheel speed is increased, the amount of secondary phases decreases, indicating a progressive increase of the degree of undercooling in the liquid. The primary

solidification of $TiNi_2Sn$ full Heusler phase is progressively by-passed as suggested by the calculated metastable Ni-TiSn isopleth.

In the case of rapidly solidified Yb-filled $CoSb_3$ and TiNiSn, consolidation of the rapidly solidified flakes was needed to obtain dense and massive samples for thermoelectric characterization. In both cases, sintering was performed by open die pressing at CNR-ICMATE in Lecco. This technique allows to sinter the powders near the recrystallization temperature, limiting grain growth and preserving the fine microstructure obtained by rapid solidification.

Thermoelectric properties of Yb-filled $CoSb_3$ samples prepared in this thesis were discussed in the framework of a wide literature survey. Seebeck coefficient and electrical conductivity scale with the amount of Yb solubilized in the skutterudite cell**,** in accordance with the increased density of charge carrier. Conversely, lattice thermal conductivity reaches a minimum in correspondence of the maximum solubility of Yb in the skutterudite cell, indicating that exceeding this limit is counterproductive due to the formation of metallic secondary phases.

In the case of TiNiSn, thermoelectric properties strongly depend on the presence of metallic secondary phases, indicating that the manufacturing process must be carefully controlled to avoid undesired impurities that can deteriorate the thermoelectric performance. Futhermore, it was shown that thermal cycling above 673 K induces

surface oxidation of titanium with consequent formation of Ni_3Sn_4 as a secondary phase. In thermally cycled samples, the Seebeck coefficient and the electrical conductivity scale in accordance with the metallic nature of Ni_3Sn_4. Quite interestingly, the power factor remains almost unchanged upon thermal cycling due to the opposite effect of the secondary phase on the Seebeck coefficient and the electrical conductivity. However, the occurrence of oxidation above 673 K suggests that a protective coating is needed to use this material in this temperature range for practical applications.

In the case of TaCoSn, the half-Heusler phase was successfully synthesized for the first time by mechanical alloying and annealing, passing through the formation of an amorphous intermediate, which is kinetically favored with respect to the equilibrium crystalline phase. The combination of thermal analysis by high temperature calorimetry and structural characterization by X-ray diffraction allowed to hypothesize the TaCo-Sn isopleth with the presence of a peritectic reaction. Sintering by cold pressing and annealing did not allow to obtain a fully dense sample. However, for first time the Seebeck coefficient of TaCoSn half-Heusler phase was measured from room temperature to 870 K, showing n-type behaviour

Finally, during my stay in Okayama University (Japan), I focused on the synthesis of ullmannites a new promising candidates for thermoelectric applications. The thermodynamic stability of four ullmannite compounds was confirmed by ab-initio calculations by

Prof. Lorenzo Maschio (University of Turin, Department of Chemistry) using Crystal code. NiSbS, NiSbSe and PdSbSe were successfully synthesized by melting pure elements, while PdSbS was synthesized by solid state reaction, probably due to a more complex solidification path. For the first time the thermoelectric properties at high temperature for NiSbS, NiSbSe and PdSbSe ullmannites compounds were measured. The NiSbS, shows a large Seebeck coefficient and a small electrical resistivity, resulting in a large power factor about 1.3 $mWm^{-1}K^{-2}$, comparable with others thermoelectric materials. The different Seebeck coefficient obtained for the four samples was explained through the differences in their band structure and density of state.